Development and Characterization of a Novel Mouse Model Carrying Mitochondrial DNA Mutations

Inaugural-Dissertation
zur
Erlangung des Doktorgrades
der Mathematisch-Naturwissenschaftlichen Fakultät
der Universität zu Köln

vorgelegt von

PAMELLA MARIE DE VELEZ SENDON

aus Manila, Philippinen

Köln, Deutschland
2024

TABLE OF CONTENTS

ABSTRACT

Mitochondria perform vital functions in the cell by regulating bioenergetics, metabolism, and signaling pathways. These organelles contain their own DNA, known as the mitochondrial DNA (mtDNA) which encodes mitochondrial ribosomal RNAs, transfer RNAs, and messenger RNAs constituting some of the subunits of oxidative phosphorylation (OXPHOS). Pathogenic mtDNA mutations can therefore affect the OXPHOS structural subunits or the mitochondrial protein synthesis machinery resulting in the development of mitochondrial diseases. In this regard, animal models are a valuable tool in understanding the mechanisms underlying mtDNA mutations and mitochondrial diseases *in vivo*.

The research presented in this thesis aims to identify specific mtDNA mutations and their molecular and biochemical consequences, investigate the effect of these mutations on the mouse phenotype, and compare the novel mouse model to the previously characterized C5024T. In this work, we generated a novel mouse model through a breeding strategy utilizing female heterozygous mutator mice with PolgA proofreading deficiency. We identified three mtDNA point mutations in a single mtDNA molecule cosegregating with mitochondrial deficiency: m.5019A>G, m.15200A>G, and m.16232A>T. The m.15200A>G mutation is a synonymous mutation located in the Cytochrome b gene while the m.16232A>T mutation caused a very little reduction in transcription initiation according to *in vitro* transcription assay; however, this has no effect on mt-mRNA steady-state levels and mtDNA copy number *in vivo*. The m.5019A>G mutation does not affect mt-tRNA^{ALA} stability but impacts mt-tRNA^{ALA} aminoacylation as shown by the presence of deacylated mt-tRNA^{ALA} molecules in the aminoacylation assay. We then refer to this novel mouse model as A5019G mice.

Phenotypically, A5019G male mice exhibited a lean phenotype with age; however, we observed no sign of heart enlargement associated with cardiomyopathy in A5019G mice, unlike in C5024T mice. Tissue-specific COX deficiency occurs in A5019G mice with the intestinal epithelial tissue being impacted the most while rare occurrence of COX deficiency is found in skeletal muscle and lung tissues. Proteomics revealed extensive changes occurring in the intestinal epithelium proteome of A5019G mice as they age. Furthermore, analysis of the mitochondrial proteins in these mice showed a significant reduction in the expression of the majority of Complex I and Complex IV protein subunits with upregulation of proteins for OXPHOS assembly, mtRNA metabolism, and mitochondrial translation as a compensatory mechanism.

In conclusion, the major pathogenic mutation causing mitochondrial dysfunction in this novel mouse model is the m.5019A>G mutation which affects the aminoacylation of mt-tRNA^{ALA} resulting in difficulties in translation of protein subunits of Complexes I and IV. Accordingly, the work covered in this thesis offers valuable insights into the control and regulation of mtDNA heteroplasmy and mitochondrial dysfunction. This work can be used in future studies involving mitochondrial genome engineering techniques to reduce mtDNA heteroplasmy and rescue the animals from OXPHOS defects, which is pertinent for potential therapeutic approaches for mitochondrial diseases.

1. INTRODUCTION

1.1. Mitochondria

1.1.1. Mitochondrial evolutionary origin

According to the endosymbiosis theory, mitochondria originated from the integration of an endosymbiotic α-proteobacterium into an Archaeal-derived host cell more than 1.45 billion years ago (Martin & Mentel, 2006; Roger et al., 2017). The host lineage is most closely related to the recently discovered group of Archaea, the Asgards (Asgard superphylum), which is comprised of novel phylum-level groups Lokiarchaeota, Thorarchaeota, Odinarcaeota, and Heimdallarchaeota, that represent the closest archaeal relatives of eukaryotes (Spang et al., 2015; Zaremba-Niedzwiedzka et al., 2017). Representative samples from this group were from deep marine sediments and hot spring metagenomes. In a recent study using expanded Asgard archaea genomic samples, phylogenetic analyses revealed that the host/eukaryotes are placed as a well-nested clade within Asgard archaea and as a sister lineage to Hodarchaeales, a newly proposed order within Heimdallarchaeia (Eme et al., 2023). The endosymbiont ancestor of the mitochondria originated within the α-proteobacteria based on the long-standing phylogenetic consensus (L. Fan et al., 2020; M. W. Gray et al., 1999). However, the precise placement of mitochondria in the α-proteobacteria tree is still a matter of debate, with contradictory results depending on the phylogenetic analyses used. Studies suggest that the closest relative of mitochondria may be Rickettsiales order, wherein Rickettsiales and mitochondria share a common ancestor with an extant marine planktonic α-proteobacteria (L. Fan et al., 2020; Wang & Wu, 2015). Rickettsiales is a group containing exclusively intracellular parasitic and endosymbiotic bacteria. Contradicting from this Rickettsiales-sister hypothesis is a study suggesting that mitochondria did not evolve from Rickettsiales, instead, they evolved from a proteobacterial lineage that branched off before the divergence of all sampled α-proteobacteria (Martijn et al., 2018). A recent study further supports this by showing that the mitochondrial lineage is sister to all known α-proteobacteria (Muñoz-Gómez et al., 2022).

Various scenarios have been proposed regarding the process of the integration of the endosymbiont to the host cell. Among these are the "archezoan scenario" and the "symbiogenesis scenario" (Koonin, 2010). The archezoan scenario, which can also be referred to as the phagotrophic origin of mitochondria or the "mitochondrion-late" theory, posits that an amitochondriate eukaryotic host cell engulfed the α-proteobacterium by phagocytosis, which

was then subsequently transformed into mitochondrion (Martin et al., 2015). On the other hand, the symbiogenesis scenario, which can also be referred to as syntrophic origin or "mitochondrion-early", hypothesizes that a physical and metabolic fusion between an α-proteobacterium and an archaeal cell generated the ancestor of the eukaryotic cell, with the α-proteobacterium subsequently becoming the mitochondrion. This was then followed by the evolution of the nucleus and compartmentalization of the eukaryotic cell (Martin et al., 2015, 2017). Several models, which include the Hydrogen hypothesis (Martin & Müller, 1998), Searcy's hypothesis (Searcy, 2003), the Reverse Flow model (Spang et al., 2019), the Entangle-Engulf-Endogenize model (Imachi et al., 2020), Hydrogen and Methane-transfer-based symbiosis (HM Syntrophy) hypothesis (López-García & Moreira, 2006), and Hydrogen and Sulfur-transfer-based model (HS Syntropy) hypothesis (López-García & Moreira, 2020), support the symbiogenesis scenario.

After the integration of the endosymbiont into the host cell, how did it transition into an organelle? Its transition required various evolutionary changes, which include, among other things, the development of the protein-transport system, characterized by the delivery of the solute carriers in the inner membrane of the proto-mitochondria, allowing the import of nuclear-encoded proteins of α-proteobacterial origin to the mitochondrion and the movement of small molecules (Gabaldón, 2021; Roger et al., 2017). Since the mitochondrial genome is highly reduced compared to the genome of its α-proteobacterial ancestor, another evolutionary change is the endosymbiotic gene transfer of the initial genetic information from the proto-mitochondrial genome to the nuclear genome of the host (M. W. Gray, 2012). However, with the α-proteobacteria being the ancestor of the mitochondria, it is surprising to see that only ~10-20% of the total mitochondrial proteome is part of the α-proteobacterial complement (M. W. Gray, 2015). A possible scenario was the presence of a basic α-proteobacterial protein core, wherein lineage-specific gains and losses occurred during evolution leading to the present-day mitochondrial proteome. It is also possible that the last mitochondrial common ancestor (LMCA) already has a complete protein important apparatus, and that the last eukaryotic common ancestor (LECA) is already a structurally complex cell. Based on phylogenetic tree reconstructions, mitochondrial proteins can be binned into four categories – those having a strong relationship with α-proteobacteria, non-α-proteobacterial homologs in prokaryotes, homologs exclusively in eukaryotes, and those lacking evident homologs in other eukaryotes. Interestingly, essential components of the mitochondrial transcription and replication machinery, which include the RNA polymerase (POLRMT), the helicase Twinkle, and the DNA polymerase (Polg) are not derived from the α-proteobacteria but from the T-odd

lineage of bacteriophage (Shutt & Gray, 2006). T-odd bacteriophage are T3 and T7 bacteriophages and their close relatives, members of a group of lytic bacteriophages known to infect γ-protobacteria. Although there isn't proof that the genes from T-odd phage have directly incorporated into the mitochondrial genomes, certain phage-like genes have been discovered in the α-proteobacterial genomes (Shutt & Gray, 2006).

1.1.2. Mammalian mitochondrial morphology

Mitochondria are cellular organelles consisting of two membranes, the outer mitochondrial membrane (OMM) and the inner mitochondrial membrane (IMM). In between the OMM and IMM is the intermembrane space (IMS) and the innermost region is the mitochondrial matrix (MM) (Figure 1.1). The IMM forms invaginations referred to as cristae, which contain the respiratory chain complexes – NADH:ubiquinone oxidoreductase (Complex I), succinate dehydrogenase (Complex II), cytochrome c reductase (Complex III), cytochrome c oxidase (Complex IV), and ATP synthase (Complex V) (Figures 1.1 and 1.2). The subunits of Complexes I, III, IV, and V are encoded both by the mitochondrial DNA (mtDNA) and the nuclear DNA (nDNA) while the subunits of Complex II are encoded solely by the nDNA. The mitochondrial-encoded subunits are hydrophobic membrane proteins while the nuclear-encoded subunits are expressed in the cytoplasm and imported inside the mitochondria (Wasilewski et al., 2017). The assembly of oxidative phosphorylation (OXPHOS) complexes has been discussed (Signes & Fernandez-Vizarra, 2018) whereby the largest OXPHOS complex is Complex I consisting of 45 subunits, with a hydrophilic arm that extends into the matrix where electron is transferred from NADH to coenzyme Q (CoQ), also referred to as ubiquinone, and a hydrophobic arm that transports protons; Complex II is compose of four nDNA-encoded subunits and has no proton pumping activity; Complex III consists of 11 subunits and accepts electrons from ubiquinone and transfers them to another electron carrier, cytochrome c; Complex IV has 13 or 14 subunits and functions in catalyzing cytochrome c oxidation and reducing oxygen to water; and Complex V or F_0F_1-ATPase is the enzyme that synthesizes ATP using the proton motive force generated by Complexes I, III, and IV. These complexes can interact with each other forming supercomplexes or respirasomes, in which Complex I-III-IV association was observed in mammalian mitochondria (Schägger & Pfeiffer, 2000). Mitochondrial DNA (mtDNA) is located in the mitochondrial matrix (further discussion of mtDNA in Section 1.2).
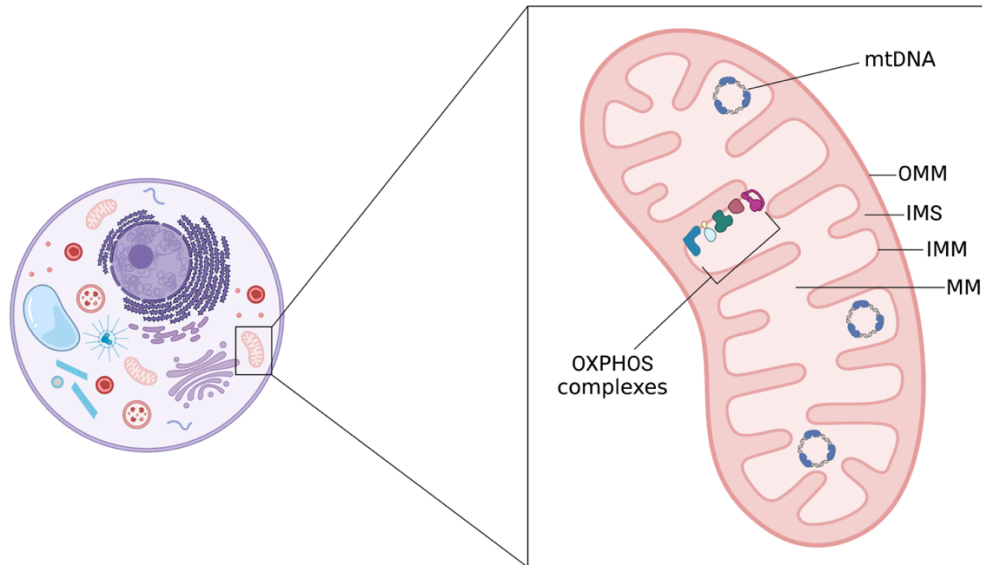
Figure 1.1 Mitochondria in animal cell. The mitochondrion is a double membrane organelle, consisting of the outer mitochondrial membrane (OMM) and the inner mitochondrial membrane (IMM). In between the two membranes is the intermembrane space (IMS). It contains its own genetic material, the mitochondrial DNA (mtDNA) located in the mitochondrial matrix (MM). Complexes for OXPHOS are located in the cristae, which are invaginations of the IMM. Created with BioRender.com.

Mitochondria are highly dynamic organelles that can create extensive intracellular networks by continually fusing and dividing (reviewed in Westermann, 2010). These processes regulate mitochondrial morphology. Mitochondrial fusion facilitates the interchange of mtDNA, mitochondrial proteins, and metabolites by fusing fragments of mitochondria. The mitochondrial fusion machinery is localized in OMM and IMM contact sites and is comprised of mitofusins, a protein family of dynamin-related GTPases, specifically the Fzo1 yeast homolog (Fritz et al., 2001) for outer membrane fusion and Mgm1 (Meeusen et al., 2006) for inner membrane fusion. In mammals, the mitofusin forms include MFN1 and MFN2 (H. Chen et al., 2003), and the Mgm1 ortholog, optic atrophy protein 1 (OPA1) (Cipolat et al., 2004). A recent study has identified small molecules, mitofusin activator small molecule (MASM7) and mitochondrial fusion inhibitor (MF18), that can regulate MFN1 and MFN2 activities (Zancharioudakis et al., 2022). Mitochondrial fission, on the other hand, is the fragmentation of the mitochondrial network. Mitochondrial fission is essential for the formation of new mitochondria as well as the removal of damaged mitochondrial components, which are eventually removed through mitophagy. It is regulated by a dynamin-related protein, Dnm1 in yeast (Bleazard et al., 1999) and DRP1 in mammals (Fonseca et al., 2019; Smirnova et al., 1998).

1.1.3. Mammalian mitochondrial functions

Mitochondria perform critical roles in the cell by the regulation of bioenergetics, metabolism, and signaling pathways (reviewed in Pfanner et al., 2019). Mitochondria are primarily known as the "powerhouse" of eukaryotic cells synthesizing adenosine triphosphate (ATP) via OXPHOS (Figure 1.2). The electron transfer occurring in Complexes I to IV releases energy which is then used to pump H^+ from the MM to the IMS. This results in a proton gradient which is utilized by Complex V to phosphorylate ADP into ATP (Boyer et al., 1973; Mitchell, 1961).
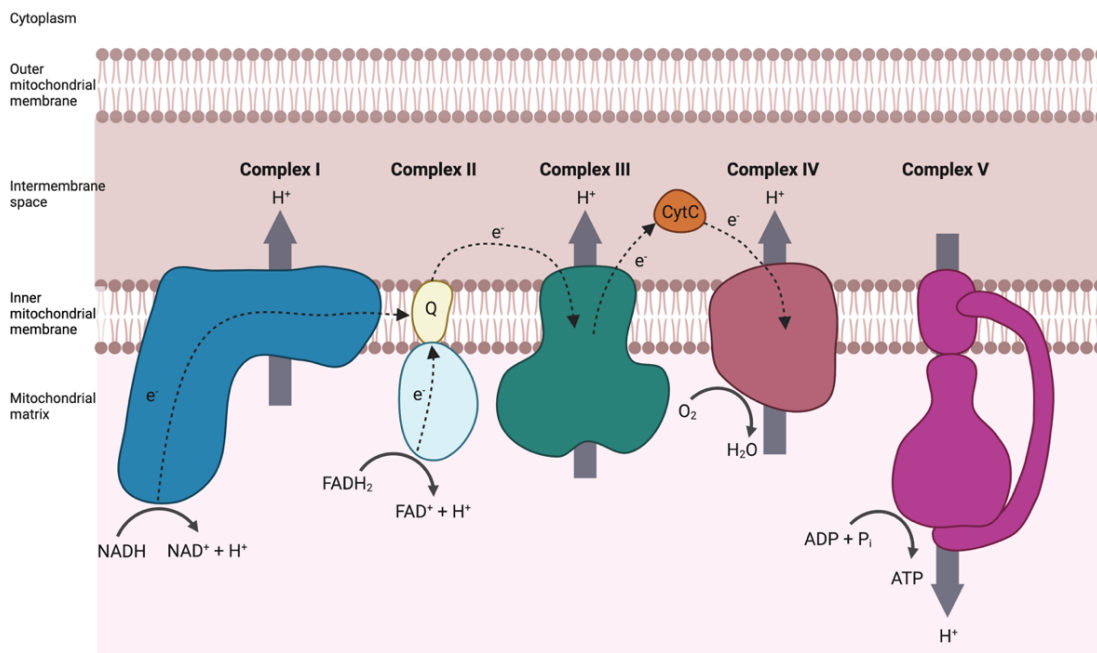
Figure 1.2 Mitochondrial oxidative phosphorylation (OXPHOS) machinery and the electron transport chain (ETC). Electron donors NADH and $FADH_2$ are oxidized by Complex I and Complex II, respectively. The released electrons are delivered to ubiquinone (Q), which transports them to Complex III. The electrons are then transferred to cytochrome c (C) and to Complex IV resulting in the reduction of O_2 to H_2O. Electron transfer is depicted by broken lines with arrowhead. H^+ are pumped from the matrix to the intermembrane space (depicted by the gray arrows) generating an electrochemical proton gradient which is then used by Complex V to synthesize ATP. Adapted from Letts & Sazanov, 2017. Created with BioRender.com.

Mitochondria are sites of metabolic pathways – the tricarboxylic acid (TCA) cycle (also referred to as Krebs or citric acid cycle), β-oxidation of fatty acids, amino acid synthesis, and nucleotide metabolism (reviewed in Pfanner et al., 2019). The TCA cycle, occurring in the MM, starts with combining acetyl CoA (derived from amino acids, fatty acids, and pyruvate oxidation) with oxaloacetate to generate citrate that is consumed and regenerated through a

series of enzymatic steps. The TCA is coupled to OXPHOS such that reducing agents NADH and FADH, which are byproducts of the TCA, are fed into the ETC and serve as electron donors (Figure 1.3) (Martínez-Reyes & Chandel, 2020; van der Bliek et al., 2017). Mitochondria are also involved in iron metabolism, specifically in heme synthesis, iron-sulfur (Fe/S) cluster (ISC) assembly, and cellular iron regulation. The ISC assembly machinery carries out three steps in the synthesis of mitochondrial Fe/S proteins: the [2Fe-2S] cluster is generated by the scaffold protein Isu1; the cluster then dissociates from Isu1 by Hsp70 chaperone system and is transported to the apoproteins by glutaredoxin Grx5; and various ISC components generate [4Fe-4S] clusters which are incorporated into the target apoproteins (reviewed in Lill et al., 2012).

Calcium ion signaling is also associated with mitochondria. Mitochondrial uptake of Ca^{2+} released by the ER occurs via the voltage-dependent anion channel (VDAC) located in the OMM and the mitochondrial calcium uniporter (MCU) channel (Baughman et al., 2011; de Stefani et al., 2011) located in the IMM (Figure 1.3). The regulation of mitochondrial bioenergetics and metabolism is influenced by Ca^{2+} in the mitochondria (reviewed in Rossi et al., 2019).

Mitochondria are sources of reactive oxygen species (ROS). During cellular respiration, ~1-2% of molecular oxygen is converted to superoxide anion ($O_2^{\bullet-}$), an ROS, due to incomplete reduction of O_2 at Complex I and Complex III. The incomplete O_2 reduction is the result of electron leak (Jastroch et al., 2010). The generation and elimination of ROS must be balanced for normal cellular function, and the imbalance causes oxidative stress, which can damage the cell (reviewed in Handy & Loscalzo, 2012).

Furthermore, mitochondria play a role in regulated cell death or apoptosis. The mitochondrial pathway of apoptosis is triggered by a variety of cellular stressors, such as DNA damage, which activates BH3-only proteins of the B cell lymphoma 2 (BCL-2) protein family. BH3-only proteins then activate the effector pro-apoptotic BCL-2 proteins, BAX and BAK. At the OMM, BAX and BAK are stabilized and form multimers generating lipid pores within the OMM resulting in mitochondrial outer membrane permeabilization (MOMP). MOMP leads to the release of soluble IMS proteins, such as cytochrome c (Figure 1.3). The lipid pores expand and form macropores over time, allowing the extrusion of the IMM through the OMM (reviewed in Bock & Tait, 2020). The responses elicited by MOMP also directly affect the regulation of inflammatory processes, which links the mitochondrial function in the control of inflammation (reviewed in Marchi et al., 2022).
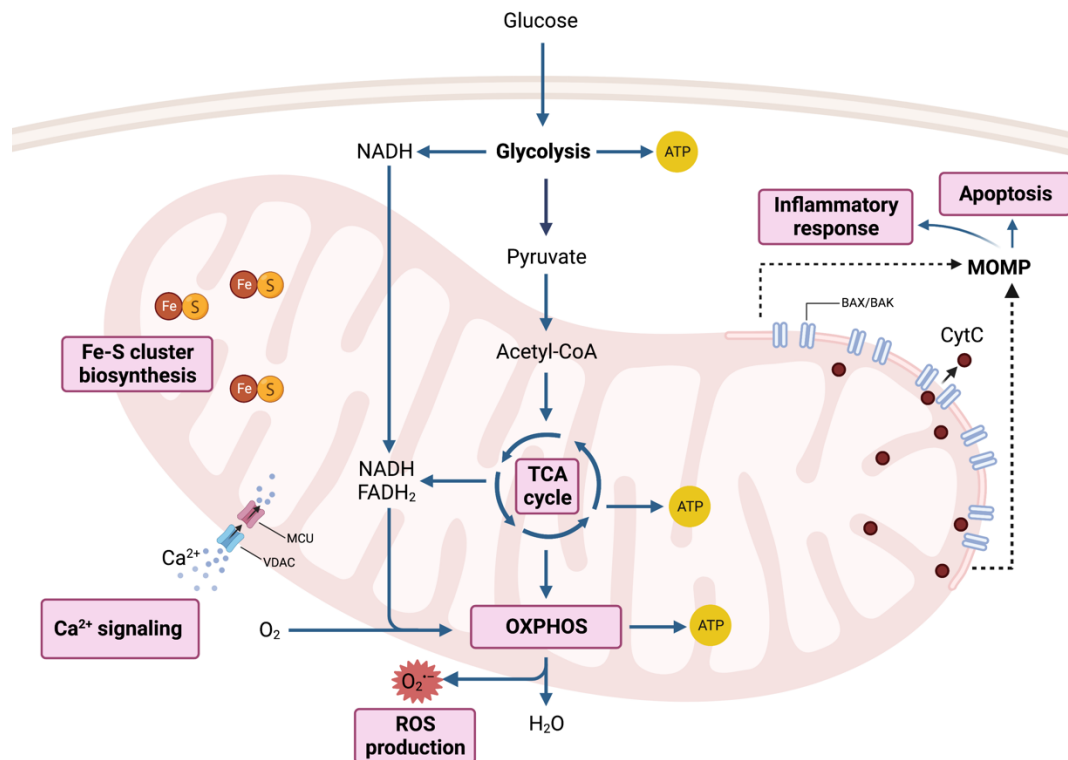
Figure 1.3 Mitochondrial functions. Mitochondria perform a wide range of functions. Some of the key functions are illustrated here in pink boxes – site of the TCA cycle, OXPHOS, ROS production, and Fe-S cluster biosynthesis. Mitochondria are also involved in Ca^{2+} signaling, apoptosis, and inflammatory response. Adapted from Bock and Tait, 2020; Rossi et al., 2019. Created with BioRender.com

1.2. Mammalian mitochondrial genome

1.2.1. Organization of the mitochondrial genome

The mammalian mitochondrial DNA (mtDNA) is a circular, double-stranded molecule located in the MM. mtDNAs are packaged, together with the mitochondrial transcription factor A (TFAM), in DNA-protein complexes referred to as nucleoids. Human fibroblasts contain ~1.4 mtDNA molecules per nucleoid and ~1.4 x 10^3 TFAM molecules per nucleoid or one TFAM molecule per 16.6 bp of mtDNA were found (Kukat et al., 2011) while ~1.1 copies of mtDNA per nucleoid are found in mouse embryonic fibroblasts (MEFs) (Kukat et al., 2015). TFAM binding and cross-strand binding leads to mtDNA compaction (Kukat et al., 2015). The compact packaging also affects mtDNA replication and transcription with high TFAM:mtDNA ratio being associated to inactivity of nucleoids to replication and transcription (Brüser et al.,

2021). Moreover, mtDNA copy number is also affected by TFAM. mtDNA copy number varies between cell types and tissues and most mammalian cells have on the order of thousands of copies per cell, with individual mitochondria often possessing multiple copies. Studies have shown that overexpressing TFAM resulted in increased copy number and disrupting it resulted in copy number reduction. Overexpressing TFAM in MEFs resulted in ~2.5-fold higher mtDNA copy number as compared to the wild type (WT) MEFs (Kukat et al., 2015) and a ~30-70% increase in mtDNA was observed in P1 artificial chromosome containing human *TFAM* gene (PAC-*TFAM*) mice (Ekstrand et al., 2004). On the other hand, heterozygous TFAM knockouts resulted in ~35-40% reduction in mtDNA copy number while the homozygous TFAM knockouts exhibited severe mtDNA depletion, severe OXPHOS deficiency, and embryonic lethality (Larsson et al., 1998).

The two complementary strands of mtDNA are referred to as heavy (H) and light (L) strands, based on the differences in their base composition (GT/CA ratio) resulting in different buoyant densities on alkaline cesium chloride (CsCl) gradients (Corneo et al., 1968). The human mtDNA is about 16.6 kb long containing 37 genes – 2 ribosomal RNAs (rRNAs), 22 transfer RNAs (tRNAs), and 11 messenger RNAs (mRNAs) encoding 13 polypeptides (Figure 1.4) (Anderson et al., 1981). The 13 polypeptides constitute some of the subunits of the OXPHOS (Anderson et al., 1981; Chomyn et al., 1983, 1985; Mariottini et al., 1986). The H strand encodes 10 mRNAs translated into 12 OXPHOS protein subunits (which include the following: cytochrome oxidase bc1 subunit CytB, cytochrome oxidase subunits CO1–CO3, NADH ubiquinone oxidoreductase subunits ND1–ND5, ND4L, and ATP synthase subunits ATP6 and ATP8), 2 rRNAs consisting of 12S and 16S, and 14 tRNAs while the L strand encodes a single mRNA translated into NADH ubiquinone oxidoreductase subunits ND6, and 8 tRNAs (Figure 1.1). Mitochondrial mRNA (mt-mRNA) and mitochondrial rRNA (mt-rRNA) genes are flanked by mitochondrial transfer RNA (mt-tRNA) genes in a condition referred to as the tRNA punctuation model (Ojala et al., 1981). The noncoding region (NCR), also referred to as the control region, is approximately 1,100 bp long, containing the promoters for transcription – heavy strand promoter (HSP) and light strand promoter (LSP), and regulatory sequences for mtDNA replication, which include the H-strand origin of replication (O_H). Located between the O_H and LSP are sequence elements, the conserved sequence blocks (CSB1-3), and the single termination-associated sequence (TAS) (Figure 1.4). Replication starting from the O_H and prematurely terminating in the TAS results in ~600 nt long DNA called
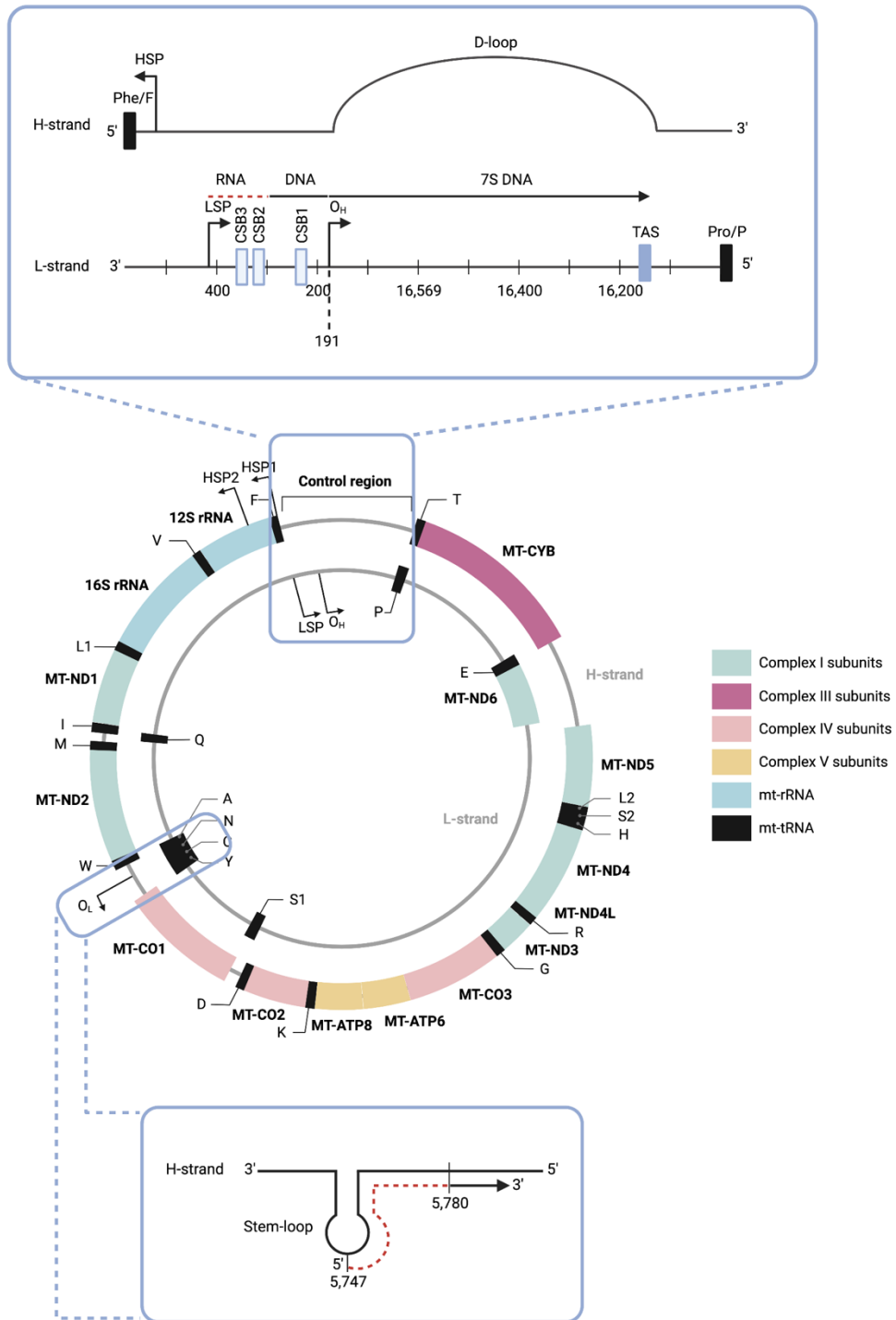
Figure 1.4 Replication of human mtDNA. The mtDNA consists of two circular strands: the heavy (H) and light (L) strands. Most of the protein-coding genes are located in the H strand and are designated here with colors based on the OXPHOS subunit their product belongs to. Two rRNAs, 12S and 16S, are also located in the H strand. MT-ND6, on the other hand, is located in the L strand. The mt-tRNAs, marked according to the single-letter amino acid code, are located in between protein-coding genes and rRNAs. Non-coding transcripts are assigned in grey. The control region contains replication and transcription regulatory elements (blue box at the top). Arrows indicate the direction of replication from the origin of replication in each strand (origin for H-strand replication, O_H; origin for L-strand replication, O_L) and the direction of transcription from the promoters (H strand promoter, HSP1 and HSP2; L strand promoter, LSP). RNA priming in the LSP and O_L are shown in the blue boxes. Adapted from Doimo et al., 2020. Created with BioRender.com.

7S DNA, which results in a triple-stranded structure known as the displacement loop (D-loop) (W. M. Brown et al., 1978). From O_H to two-thirds around the genome, in a group of five tRNA genes, the origin of replication directing the L-strand synthesis, O_L, is situated (Figure 1.4).

1.2.2. Mitochondrial DNA replication and maintenance

Mitochondrial DNA replication is a vital process required for the maintenance of mtDNA. It consists of the following steps: initiation, elongation, and termination (reviewed in Doimo et al., 2020; Falkenberg, 2018; Falkenberg et al., 2007; Falkenberg & Gustafsson, 2020; Gustafsson et al., 2016). mtDNA replication is mediated by DNA polymerase γ (POLγ), Twinkle, and mitochondrial single-stranded binding protein (SSBP1). The human POLγ contains one catalytic subunit (POLγA) with 3'–5' exonuclease activity for proofreading of the newly synthesized mtDNA and (in mammals) two accessory subunits (POLγB) that aid in increasing the POLγA catalytic activity (Bailey & Anderson, 2010; Farge et al., 2007; H. Gray & Wong, 1992). Twinkle (a T7 gp4-like protein with intramitochondrial nucleoid localization) is a helicase that initiates the unwinding of mtDNA. The mtSSB then stabilizes the single-stranded DNA.

While several models have been proposed for mtDNA replication, the long-standing and widely supported one is the strand displacement model (Figure 1.5) (T. A. Brown et al., 2005). In this model, initiation of replication of the H-strand occurs at the O_H region. First, an RNA primer is synthesized by POLRMT from the LSP site (Figure 1.4). In the LSP, the sequence of the CSB2 region, specifically within a G-rich stretch of 16 nucleotides prone to produce a large, secondary G-quadruplex (G4) structure that can terminate transcription (Wanrooij et al., 2010), causes POLRMT to stall, thereby resulting in a switch between replication and transcription. A novel conserved transcription pausing site near the L-strand transcription initiation site was mapped which may play a role with the transcription-replication transition site in CSB2 (Blumberg et al., 2017). In addition, Blumberg et al. also identified another pausing site in the H-strand, partially overlapping the O_L. These pausing sites were hypothesized to provide the replication machinery enough time to assemble (Blumberg et al., 2017). The switch from transcription to replication is then modulated by the mitochondrial transcription elongation factor (TEFM) (Agaronyan et al., 2015). The RNA generated can be prematurely terminated when TEFM is not incorporated and serve as RNA primer for mtDNA replication (Figures 1.4 and 1.5).
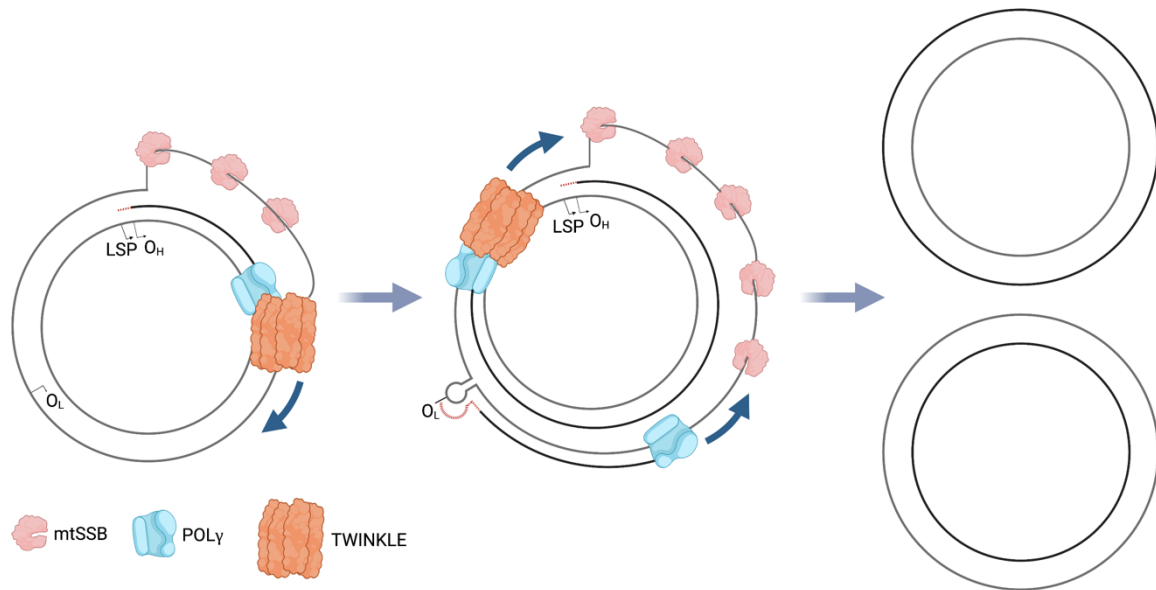
Figure 1.5 Strand-displacement model of mitochondrial DNA Replication. For the leading strand DNA synthesis, an RNA (red broken lines) is first synthesized at the LSP. TWINKLE unwinds the dsDNA while mtSSB coats the ssDNA to stabilize it and stimulate POLγ activity. POLγ then used the RNA as an RNA primer and a new DNA is synthesized at the O_H. When the replication machinery passes the O_L, a stem-loop structure is formed where an RNA primer is synthesized, and the lagging strand DNA synthesis is initiated. The replication machinery for both the leading and lagging strands travels around the mtDNA molecule to complete the strand synthesis. DNA replication is terminated back to the O_H and O_L and RNA primers are removed. Adapted from Rackham and Filipovska, 2022. Created with BioRender.com.

POLγ, catalyzes the replication in a continuous and unidirectional manner. TWINKLE unwinds the DNA at the replication fork and travels in a 5' to 3' direction on the parental H-strand (Korhonen et al., 2003) while the mitochondrial single-stranded DNA binding protein (mtSSB) stimulates the POLγ for the leading strand DNA synthesis and coats the single-stranded DNA (Figure 1.5). A study has found that there is substantial mtSSB occupancy right downstream of the D-loop region followed by a steady decrease of mtSSB occupancy towards O_L, with ~2,100 mtSSB molecules per mtDNA molecule that can completely cover the parental H-strand (Miralles Fusté et al., 2014). Replication at the lagging strand, then, begins when the synthesis of the leading strand reaches two-thirds of the genome exposing the O_L region in single-stranded form. A stem-loop structure is formed at the O_L to which POLRMT synthesizes an RNA primer which will be catalyzed by POLγ (Figures 1.4 and 1.5). The synthesis of the leading and lagging strands continues until newly replicated strands are completed (Figure 1.5). Before completion of replication, the RNA primers need to be removed first by RNase H1(Holmes et al., 2015). DNA ligase 3 (LIG3) then ligates the nascent strands (Lakshmipathy

& Campbell, 2001) and the topoisomerase 3α (TOP3α) separates the interlinked daughter molecules (Nicholls et al., 2018).

As an alternative to the strand-displacement model, there are two other models: the strand-coupled model and the ribonucleotide incorporation throughout the lagging strand (RITOLS) model. The strand-coupled model suggests that there is a unidirectional, coupled leading- and lagging-strand replication starting at O_H and proceeding unidirectionally around the entire mtDNA (Holt et al., 2000). Holt et al. analyzed human and mouse mtDNA replication intermediates using two-dimensional agarose gel electrophoresis (2D-AGE) and found two types of replication intermediates, one group was single-stranded which might be derived from the strand-displacement model and the other group was double-stranded which might be derived from coupled leading- and lagging-strand mtDNA synthesis and were predominant in cultured cells recovering from transient mtDNA depletion (Holt et al., 2000). Both the RITOLS and strand-displacement models share a unidirectional nature and the approximate location of origin of replication. The main difference is that the proponents of the RITOLS model detected tracts of RNA/DNA hybrid in mtDNA replication intermediates using 2D-AGE leading them to suggest that the displaced H-strand is coated by preformed processed RNA instead of the mtSSB in the strand-displacement model (Yasukawa et al., 2006). A 'bootlace' mechanism of the RITOLS model was then proposed wherein processed transcripts are sequentially threaded onto the lagging-strand template producing RNA/DNA hybrid tracts with a discontinuous RNA strand (Reyes et al., 2013). However, another study performed the same methods used by the proponents of the RITOLS model and found that when mtDNA is being purified, mtSSB is eliminated using proteinase K treatment revealing the H-strand in its single-stranded form, thus, allowing the majority of mitochondrial transcripts present in mtDNA preparations to anneal to their complementary areas in the parental H-strand generating RNA/DNA hybrids that can be mistaken for mtDNA replication intermediates (Miralles Fusté et al., 2014).

1.2.3. Mitochondrial transcription

Mitochondrial transcription plays a crucial role in gene expression and is also closely linked to mtDNA replication and maintenance. Mitochondrial transcription involves initiation, elongation, and termination steps (reviewed in D'Souza & Minczuk, 2018; Falkenberg et al., 2007; Fontanesi et al., 2020; Gustafsson et al., 2016; Rackham & Filipovska, 2022). Mitochondrial transcription is initiated at both the H-strand promoter (HSP) and L-strand promoter (LSP)

located at the control region (Figure 1.6A). Mammals usually have only one HSP but in humans, there are two HSPs – HSP1 and HSP2 (Figure 1.4) (Montoya et al., 1982, 1983). Transcript from HSP1 encompasses 12S and 16S rRNA, tRNA[Phe], and tRNA[Val] while transcript from HSP2 is polycistronic covering almost the entire H-strand. The LSP generates a transcript consisting of ND6 and 8 tRNAs. Interestingly, a recently published article discovered a second light strand promoter, LSP2, in the human mitochondrial genome and proposed that replication and gene expression is orchestrated from two distinct sites (Tan et al., 2022). Its physiological functions, though, remain to be fully characterized.

Transcription begins when transcription factor A (TFAM) binds to the upstream start site of LSP and HSP promoters, bending the mtDNA into a U-shape (Ngo et al., 2011; Rubio-Cosials et al., 2011). TFAM also recruits POLRMT to the promoters by linking its high-mobility group Box B domain to the helix in POLRMT's N-terminal region (Hillen et al., 2017). Transcription factor B2 (TFB2M) then binds to the initiation complex and induces promoter melting (Posse & Gustafsson, 2017). It is important to note that after the LSP region, the G4 structures at CSB2 can stimulate the termination of mitochondrial transcription (Wanrooij et al., 2010). However, when TEFM is incorporated, the G4 structures are weakened allowing PORLMT to transcribe the whole strand without having to stop at CSB2 (Agaronyan et al., 2015). As transcription elongation continues, near-genome length L-strand transcript is formed. Transcription is terminated before it reaches the promoters in both L- and H-strands (Figure 1.6A). Termination of transcription is mediated by termination factor 1 (MTERF1). MTERF1 has a preferential binding with the L-strand (Nam & Changwon, 2005). In a study of MTERF1 knockout in mice, the loss of MTERF1 has resulted in increased RNA levels downstream of the L-strand termination site suggesting that MTERF1 blocks transcription from LSP but steady-state levels of mt-rRNAs, mt-mRNAs, and mt-tRNAs from HSP were not altered (Terzioglu et al., 2013). In the L-strand, MTERF1 recognizes the 22-nt sequence in the tRNA[Leu] gene as the termination point for transcription (B. Kruse et al., 1989). A structural study has discovered that upon sequence recognition, MTERF1 unwinds the DNA and promotes base-flipping for stable binding, which is necessary for transcription termination (Yakubovskaya et al., 2010). Contrary to the well-established process of L-strand transcription termination, the mechanism of H-strand transcription termination has not yet been fully understood.

The resulting polycistronic HSP and LSP transcripts, then, undergo posttranscriptional regulatory processes (Figure 1.6B) – after processing of primary transcripts, mt-mRNAs are subjected to polyadenylation by mitochondrial poly(A) polymerase (mtPAP) (reviewed in

Rorbach & Minczuk, 2012); mt-rRNAs undergo chemical nucleotide modifications (reviewed in Rorbach & Minczuk, 2012); and mt-tRNAs require CCA sequence addition at the 3'-end followed by chemical nucleotide modifications (Suzuki, 2021; Suzuki et al., 2011).
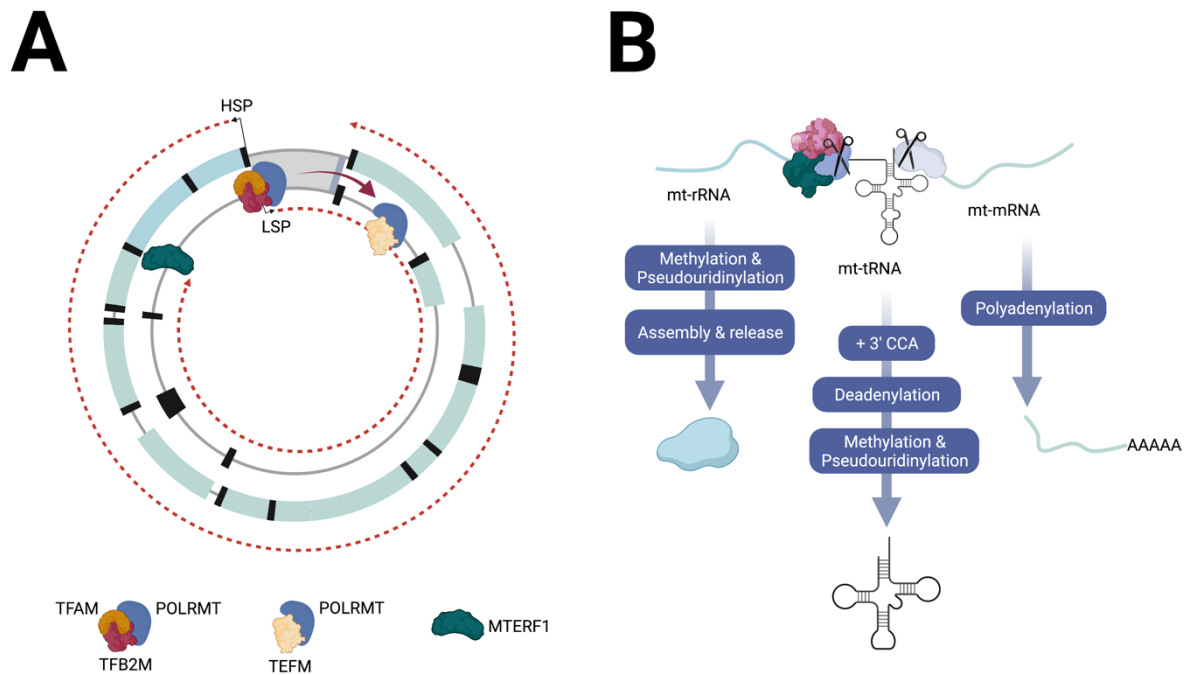
Figure 1.6 Mitochondrial transcription and posttranscriptional regulation. A. Transcription is initiated at the LSP and HSP by the transcription initiation machinery consisting of TFAM, TFB2M, and POLRMT, which synthesizes nascent RNA. TEFM aids in transcription elongation and MTERF1 terminates transcription. Adapted from Miranda et al., 2022. **B.** A number of posttranscriptional regulatory events, such as methylation and pseudouridinylation, deadenylation, and polyadenylation, take place to produce mature mt-rRNAs, mt-tRNAs, and mt-mRNAs. Adapted from Rackham and Filipovska, 2022. Created with BioRender.com.

1.2.4. Mitochondrial tRNA aminoacylation

Mitochondrial transfer RNAs (mt-tRNAs) play an important role in mitochondrial protein synthesis by decoding the genetic code of the mt-mRNA codons and translating them to the corresponding amino acids. Transfer RNAs typically adopt a cloverleaf secondary structure with the following parts: the acceptor stem with CCA end, the dihydrouridine arm (D arm), the T arm or TΨC arm, the variable loop, and the anticodon arm (Figure 1.7A). However, variations in the canonical structure are known within mitochondrial tRNAs, including the loss of the DHU-loop in the the mt-tS[GCN] of most animals (Steinberg & Cedergren, 1994). The acceptor stem is composed of seven base pairs formed by the 5' and 3' ends of the tRNA in

which the 3' CCA sequence and the discriminator base protrude from this stem. The discriminator base, which is the fourth nucleotide from the 3' end of the tRNA, determines tRNA aminoacylation or tRNA charging and is recognized by aminoacyl-tRNA synthetases. The anticodon, which is located at positions 34, 35 and 36, recognizes the mRNA codon positions 1, 2, and 3 on the mRNA by hydrogen bonding at the ribosome's A site. The first and second letters of the codon pair with the third (position 36) and second (position 35) locations of the anticodon by carefully adhering to Watson-Crick pairing. However, the base pairing between the mRNA codon's third letter and the anticodon's first position (position 34) does not necessarily adhere to the Watson-Crick pairing, but instead occurs in what is referred to as wobble pairing, which allows the 61 sense codons to be decoded by a small number of tRNAs (Crick, 1966).
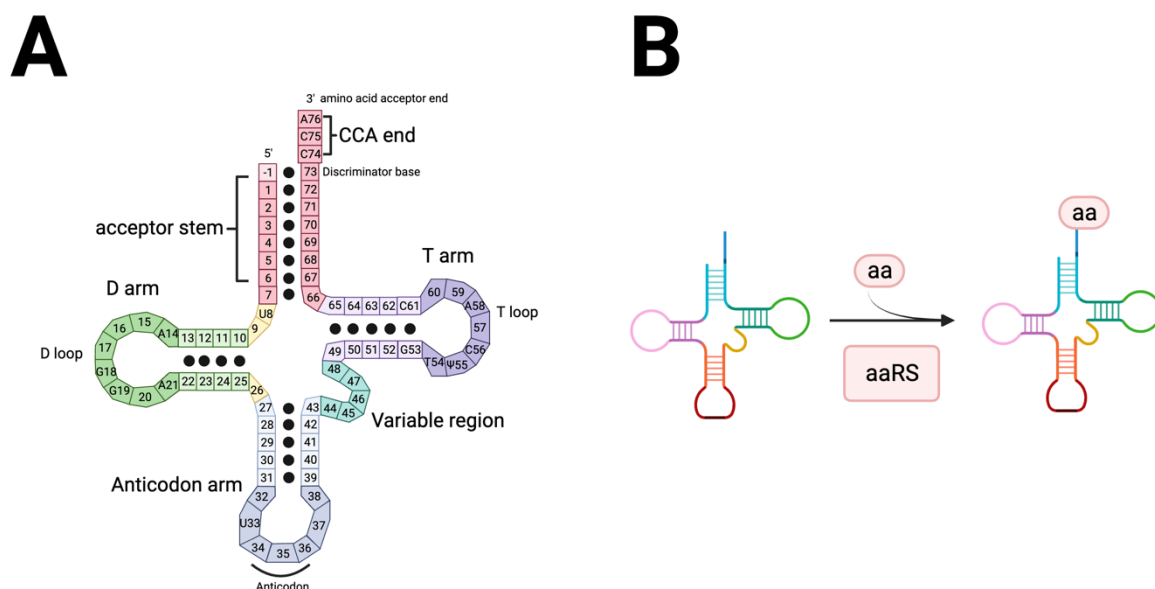
Figure 1.7 Structure and aminoacylation of mitochondrial tRNA (mt-tRNA). A. The acceptor stem with a CCA end, the D arm, the T arm, the variable loop, and the anticodon loop that recognizes specific codons on the mRNA comprise the cloverleaf structure of mt-tRNA. Watson-Crick base pairing indicated by ●. **B.** Aminoacylation or tRNA charging is an integral part of protein synthesis. This process is facilitated by aminoacyl-tRNA synthetase (aaRS) resulting in the attachment of amino acid (aa) to its cognate mt-tRNA. Adapted from Giegé & Eriani, 2023; Huot et al., 2019; and Suzuki, 2021). Created with BioRender.com.

mt-tRNAs must be charged with an amino acid that matches the sequence of its anticodon. This process is catalyzed by mitochondrial aminoacyl-tRNA synthetases (mt-aaRSs), which are nuclear-encoded and imported into the MM. Firstly, mt-aaRS forms an

aminoacyl intermediate by binding to ATP and amino acid. The amino acid is then transferred to the mt-tRNA resulting in an activated or charged mt-tRNA required for translation (Figure 1.7B). Defects in mitochondrial amino acid charging/aminoacylation reaction due to mutations in mt-tRNAs and mt-aaRSs can have a severe impact on protein synthesis, which can then result in several human disorders (Fine et al., 2019; Orellana et al., 2022; Tahmasebi et al., 2018). The variety of illnesses linked to mutations in mt-tRNAs and mt-aaRSs are mostly associated with a predilection for the central nervous system (CNS) (Sissler et al., 2017). Mutations in mt-tRNAs and the diseases they cause will further be discussed in Section 1.4.1. For mutations in the mt-aaRSs, CNS pathologies include leukodystrophies, encephalopathies, and Perrault syndrome (Sissler et al., 2017). An example of a leukodystrophy caused by mt-aaRS mutations is DARS2 leukodystrophy, a leukoencephalopathy with brainstem and spinal cord involvement and lactate elevation (LBSL), characterized by slowly progressive cerebellar ataxia, stiff or rigid muscles, and dysfunction of the dorsal column, with magnetic resonance imaging pattern of cerebral white matter abnormalities and selective involvement of brain stem and spinal tracts (van der Knaap et al., 2003). DARS2 leukodystrophy, is caused by mutations in mitochondrial aspartyl-tRNA synthetase (mtAspRS). Almost all LBSL patients have two compound heterozygous DARS2 mutations, with one at the 3' end of the second intron of DARS2 affecting the splicing of the third exon. This results in the exclusion of exon 3 in mtAspRS mRNA leading to a frameshift, premature stop, and the absence of functional protein largely in neuronal cell lines (Van Berge et al., 2012). There is a possibility that the splicing defect is "leaky" which allows the expression of a reduced quantity of wild type protein from this allele. Other leukodystrophies include EARS leukodystrophy, a leukoencephalopathy involving the thalamus and brainstem and lactate elevation caused by mitochondrial glutamate tRNA synthetase mutations and AARS2 leukodystrophy, an ovario-leukoencephalopathy, caused by mutations in mitochondrial alanyl-tRNA synthetase (Fine et al., 2019). In addition to affecting the CNS, mt-aaRSs mutations have also been linked to diseases in the cardiovascular, endocrine, musculoskeletal, and urinary systems (Sissler et al., 2017).

1.2.5. Mitochondrial translation

Mitochondrial translation is responsible for the synthesis of 13 mitochondrially-encoded proteins involved in OXPHOS to produce ATP. The mitochondrial translation machinery is composed of mt-mRNAs, mt-tRNAs, and the assembled mitoribosome. Mitochondrial translation is a multistep process involving initiation, elongation, termination, and ribosome recycling (reviewed in Fontanesi et al., 2020; Hällberg & Larsson, 2014; Kummer & Ban, 2021;

Ott et al., 2016). During translation initiation, matured mt-mRNAs are recruited to the mitoribosome. Since mammalian mt-mRNAs lack 5' untranslated regions (UTRs) (Montoya et al., 1981; R. J. Temperley et al., 2010) that, together with translation activators, promotes mRNA binding to the mitoribosome, a structural study of mammalian mitochondrial translation initiation machinery at 3.2 Å resolution using cryo-EM has revealed that the mitochondria-specific pentatricopeptide repeat (PPR) protein mS39 may facilitate mt-mRNA binding by crowning the mRNA entry channel and interacting with uridine-rich regions of the transcript's coding sequence (Kummer et al., 2018). Another structural analysis at ~3.0 Å resolution of the human mitoribosome has shown that the LRPPRC-SLIRP complex, leucine-rich PPR motif-containing protein (LRPPRC) and the stem-loop interacting RNA binding protein (SLIRP), is involved in delivering the mt-mRNA to the mitoribosomal subunit by means of a specialized platform created by mS39 (Aibara et al., 2020). When the mt-mRNA is coupled to the ribosomal small subunit (SSU), the mt-mRNA 5' start codon (AUG, AUA, and/or AUU) is selected by the initiator tRNA carrying the formylated methionine (fMet-tRNA^{Met}) in the ribosomal peptidyl (P) site (Bianchetti et al., 1977). In mammalian mitochondria, initiation factors IF2$_{mt}$ and IF3$_{mt}$ help recruit the fMet-tRNA^{Met}. IF2$_{mt}$ enhances the binding of the fMet-tRNA^{Met} to the P site while concurrently blocking the binding of the mt-tRNAs to the ribosomal aminoacyl (A) site (Spencer & Spremulli, 2004). A structural study of 28S mitoribosomal subunit and IF3$_{mt}$ complex has revealed the role of the mito-specific N terminal extension of IF3$_{mt}$ in the binding of the initiator tRNA to the 28S subunit while the mito-specific C-terminal extension functions in dissociating the initiator tRNA from the P-site in the absence of mRNA (Koripella et al., 2019). Following the selection of the start codon, the ribosomal large subunit (LSU) joins the SSU assembling into a monosome while the IFs disengage from the SSU, and the mt-mRNA is stably bound.

When the monosome is formed, it moves along the mt-mRNA elongating the nascent chain through a series of binding of aminoacylated mt-tRNAs that match the mt-mRNA codon, formation of peptide bonds, and displacement of deacylated mt-tRNAs. Mitochondrial elongation factor Tu (mtEFTu) transports aminoacylated mt-tRNAs to the mitoribosome aminoacyl (A) site (Schwartzbach & Spremulli, 1989). Following delivery, mtEFTu exits the mitoribosomes and is recycled by the guanine exchange factor, mtEFTs, to link with GTP to bind and deliver the subsequent aminoacylated mt-tRNA (Cai et al., 2000). The mitoribosome, then, simultaneously moves the mt-mRNA and mt-tRNAs upon addition of each amino acid to read the subsequent mRNA codon. This mRNA-tRNA translocation step is catalyzed by mitochondrial elongation factor G1 (mtEFG1) (Bhargava et al., 2004). Once the peptide bond

is formed, the deacylated mt-tRNA occupies the P-site, then moves to the E-site, and exits the mitoribosome.

Termination of translation occurs when the translation apparatus encounters the stop codon. The mitochondrial genetic code deviates from the universal genetic code, such that the standard stop codon UGA has been reassigned to encode tryptophan in vertebrate mitochondria, while the two arginine codons AGA and AGG have no cognate tRNAs and have instead been reassigned to stop codons (Anderson et al., 1981; Lind et al., 2013; Osawa et al., 1989; Watanabe, 2010). In human mitoribosomes, however, one study described that AGA and AGG stop codons are not recognized as termination codons because a −1 frameshift at the AGA and AGG codons were predicted to terminate the MTCO1 and MTND6 ORFs leading to the termination at the standard UAG stop codon (R. Temperley et al., 2010). However, more recent evidence suggests that AGA and AGG codons may act as functional stop codons in humans. Four proteins with putative release activity localizing in the mitochondria were identified: mtRF1a, mtRF1, C12orf65, and ICT1. The ribosome release factor (mtRF1a) decodes the standard stop codons UAA and UAG and stimulates the release of the newly synthesized polypeptide from the mtLSU (Soleimanpour-Lichaei et al., 2007). The mtRF1 shows a release activity at AGA and AGG non-canonical stop codons (Krüger et al., 2023). The ICT1 release activity occurs at the AGA and AGG stop codons (Krüger et al., 2023). A certain group of putative translation termination factors may be able to recognize the complex and release the partially synthesized chain when aminoacylated mt-tRNAs are insufficient (Kummer & Ban, 2021).

After the release of the nascent polypeptide chain, the mitochondrial ribosome recycling factor (mtRRF) (Rorbach et al., 2008) and the mitochondrial elongation factor G2 (mtEF-G2) (Tsuboi et al., 2009) split the ribosomes into individual subunits for ribosome recycling. Another protein, the GTP binding protein 6 (GTPBP6), with its dual function, facilitates the dissociation of mitoribosomes and their assembly (Lavdovskaia et al., 2020). The splitting, then, enables the ribosomes to re-enter mitochondrial translation.

1.3. Mitochondrial DNA mutations: Heteroplasmy and segregation

It has long been hypothesized that the mitochondrial genome is subject to high mutation rate, ~10-fold higher than that of the nuclear genome which is believed to be due to an inefficient DNA repair system, the absence of protective histone proteins, and its proximity to respiratory

chain complexes where reactive oxygen species (ROS) are generated (Bernt et al., 2013; W. M. Brown et al., 1979). Recent research, however, has shown strong proof refuting the notion that ROS are driver of mutagenesis (Itsara et al., 2014; Kauppila et al., 2018; Kauppila & Stewart, 2015; Kennedy et al., 2013; Sanchez-Contreras et al., 2023). A hallmark of oxidative damage is the presence of G>T mutations. A study utilizing duplex sequencing of mtDNA from human brain tissue from young and old individuals showed that the G>T mutations do not significantly increase with age (Kennedy et al., 2013). This is further supported by a very recent study utilizing deep sequencing that detected more than 89,000 independent somatic mtDNA mutations in aging mice showing that the second most common type of mutation, the G>T/C>A substitutions which indicate oxidative damage, did not increase with age irrespective of the type of tissue (Sanchez-Contreras et al., 2023). The predominant type of mutation across all tissues and which also increased with age are G>A/C>T substitutions, which can arise by replication errors or by cytidine deamination (Sanchez-Contreras et al., 2023) leaving it unclear if replication errors or oxidative cytidine deamination are the predominant source of mtDNA mutations.

MtDNA mutations can occur in the maternal germline and can then be transmitted to the offspring. MtDNA variants can be homoplasmic or heteroplasmic. Homoplasmy occurs when all the copies of mtDNA are identical. Its transmission is simple as all the maternal offspring will carry the homoplasmic mtDNAs. When two or more different variants exist in a cell, such as mutant and wild type mtDNAs, it is a condition known as heteroplasmy (Figure 1.8). At least one in 200 individuals harbors a heteroplasmic mtDNA mutations which shows how common it is in the general population, albeit at very low levels (Elliott et al., 2008). Heteroplasmic mtDNA mutations are transmitted in a more complex manner whereby the heteroplasmy level in each of the offspring is often different from that found in the mother.

Heteroplasmic mtDNA transmission was first observed in Holstein cows where two different mitochondrial genotypes were identified in cows in one generation within a single maternal lineage (Hauswirth & Laipist, 1982). The researchers suggested that this was due to the random segregation of these genotypes during oogenesis (Laipis et al., 1988; Olivo et al., 1983). The mitochondrial genetic bottleneck hypothesis has been proposed to explain the transmission and segregation of mtDNA variants (reviewed in Carling et al., 2011; Stewart & Chinnery, 2015). Several groups have subsequently studied the segregation of heteroplasmic mtDNAs by isolating single germ cells at different developmental stages and quantifying their mtDNA copy number. Cao et al. identified primordial germ cells (PGCs) using alkaline phosphatase histochemistry and estimated mtDNA copy number using quantitative real-time

PCR (qrt-PCR) in E7.5-E13.5 mouse embryos. They measured constant amount of mtDNA in PGCs across developmental stages (mean of 1,561 mtDNA copies for S cells, 1,989 mtDNA copies for M cells, and 2,879 for L cells) and an expansion of mtDNA levels during early oocyte maturation (primary oocytes at 20 μm diameter have 5.16 x 10^3 mtDNA copies and at 20-40 μm diameter have 5.83 x10^4 mtDNA copies) indicating that the bottleneck has no mtDNA reduction in PGCs but due to a small number of segregating units, each containing multiple mtDNA molecules (Cao et al., 2007, 2009). These findings indicate that the segregating units containing multiple mitochondrial nucleoids and that the bottleneck observed was caused by the segregation of homoplasmic multi-copy nucleoids instead of independent mtDNA molecules (Carling et al., 2011). A possible reason why Cao and colleagues did not observe mtDNA reduction in PGCs is that the quantitative real-time PCR for mtDNA copy number measurement was interfered with by the ALP histochemical staining used to isolate PGCs (Carling et al., 2011; Cree et al., 2008). Cree and colleagues, on the other hand, showed that there is reduction of mtDNA during embryogenesis, ~100-fold lower than in mature oocytes. To identify PGCs, they used fluorescently sorted PGCs expressing green fluorescent protein-tagged Stella. Reduction in mtDNA copies was observed during immediate preimplantation and postimplantation developmental stage, which generates the variation in heteroplasmy levels among offspring of heteroplasmic female mice. The group suggested that bottleneck is due to the partitioning of mtDNA molecules in different cells before and after implantation followed by replicating mtDNA between proliferating PGCs (Cree et al., 2008). In their model, replicating mtDNA molecules are segregating generating a variation in heteroplasmy levels. Another group, Wai and colleagues, isolated germ cells using a reporter transgene, enhanced green fluorescent protein (EGFP), and measured mtDNA copy number and heteroplasmy. The model proposed by Wai et al. is that there is a physical bottleneck in the earliest PGCs that enables selection against deleterious mtDNA mutations while the genetic bottleneck occurs during postnatal folliculogenesis due to the replication of a subpopulation of mtDNAs and not during embryonic oogenesis (Wai et al., 2008). It has been reported that aside from mtDNA selection during female germline maturation, a second step of selection occurs at the early embryonic stages of heteroplasmic mice (Latorre-Pellicer et al., 2019). Supporting earlier discoveries in mice, Floros et al. found a reduction in mtDNA levels in isolated PGCs from human embryos *in vivo*, ~1000-fold less than in oocytes (mean of 1.22 x 10^6 mtDNA molecules in oocytes and 1,446 mtDNA molecules in embryo). However, the smaller amount of mtDNA found in human PGCs suggests that there is tighter genetic bottleneck in humans than in mice resulting in a more rapid segregation of heteroplasmy (Floros et al., 2018).
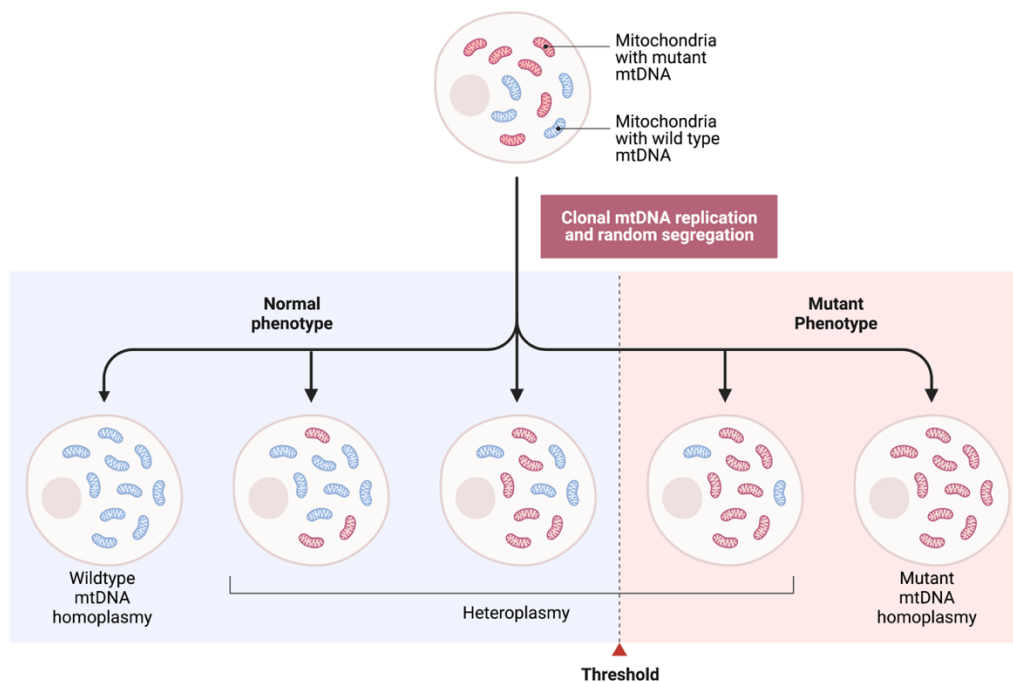
Figure 1.8 Mitochondrial DNA heteroplasmy. The presence of wild type and mutant mtDNAs in the mitochondria is referred to as heteroplasmy. Different heteroplasmic levels are caused by clonal mtDNA replication and random segregation in dividing cells. OXPHOS biochemical deficiency then results in an increase in mutant mtDNA proportions exceeding the biochemical threshold. Template from BioRender.com.

1.4. Mitochondria in disease

1.4.1. Mitochondrial DNA disease-associated mutations

Mitochondrial diseases are generally referred to as disorders of the respiratory chain (DiMauro, 2004). Mitochondrial diseases are clinically heterogeneous and can affect any tissue – with high-energy demand tissues, such as the heart, skeletal muscle, and brain being highly sensitive to mitochondrial dysfunction (Figure 1.9). A wide variety of clinical symptoms are also involved in mitochondrial diseases which may present as metabolic, neurological and neuromuscular disorders, cardiomyopathy, or diabetes among others (Macken, Lucassen, et al., 2021; Taylor & Turnbull, 2005). Furthermore, mitochondrial diseases can occur at any age. All these features thus make the clinical diagnosis of mitochondrial diseases challenging and complicated.

Since mitochondria are under dual genetic control of the mitochondrial genome and the nuclear genome, mitochondrial disorders can either result from mutations in mtDNA or

mutations in nDNA. According to a comprehensive assessment in Northeast of England, the prevalence rate of people at risk for a mitochondrial disease due to either nDNA or mtDNA mutations was 1 in 4,300; 2.9 per 100,000 due to nuclear DNA mutations; and 1 in 5,000 (20 in 100,000) due to mtDNA mutations (Gorman et al., 2015). Over 350 nuclear- and mitochondrial-encoded genes are associated with mitochondrial diseases (Mavraki et al., 2022). This section will focus primarily on mitochondrial diseases associated with mtDNA mutations. Pathogenic mtDNA mutations can affect the OXPHOS structural subunits or the mitochondrial protein synthesis machinery (Gorman et al., 2016). These mtDNA mutations can be point mutations, small deletions or insertions, or large rearrangements (Ylikallio & Tyynismaa, 2015a). Mutations in the mtDNA protein-coding genes affect the OXPHOS function and are widely known to be involved in multisystem and tissue-specific disorders. Pathogenic mt-tRNA and mt-rRNA mutations disrupt mtDNA translation, resulting in a deficiency in mitochondrial protein synthesis and diminished OXPHOS activity. Around 109 "Confirmed" disease-related mtDNA mutations have been reported in Mitomap database (https://www.mitomap.org) as of January 2024.

Researchers first recognized pathogenic mtDNA mutations that cause human diseases in 1988. These include mtDNA single, large-scale deletions discovered in patients with mitochondrial myopathy (Holt et al., 1988) and a single-nucleotide variant, nt11778 in ND4 changing the highly conserved amino acid from arginine to histidine, causing Leber's Hereditary Optic Neuropathy (LHON) (Wallace et al., 1988). Aside from LHON, recurring mtDNA mutations were associated with the most prevalent mitochondrial diseases, such as Leigh syndrome, mitochondrial encephalopathy, lactic acidosis and stroke-like episodes (MELAS) syndrome, myoclonic epilepsy with ragged red fibers (MERRF), and neuropathy, ataxia, and retinitis pigmentosa (NARP) syndrome (Gorman et al., 2016). Point mutations in specific mt-tRNA genes caused well-recognized classes of mitochondrial encephalomyopathies comprising of mitochondrial encephalomyopathy, MELAS, and MERFF. The most common single mutation to cause mitochondrial disease is m.3243A>G mutation in the MT-TL1 gene (mitochondrially encoded mt-tRNA^{Leu}) resulting in a wide range of phenotypically diverse diseases, such as myopathy, MELAS, diabetes mellitus, cardiac disease, inherited deafness, and gastrointestinal disorders (Boggan et al., 2019). Additionally, there is a wide range of m.3243A>G heteroplasmy in different tissues, with post-mitotic tissues exhibiting higher levels of mutant mtDNA while an age-related decline in m.3243A>G levels was occurring in blood (Grady et al., 2018; Veitia, 2018).

While many variants on the CR have been found, linking them to disease has been challenging. CR mutations may affect the regulation of mtDNA gene expression. In one study, it was shown that in a pedigree analysis with maternally inherited tubulointerstitial kidney disease, a homoplasmic substitution m.547A>T in the HSP was identified resulting in reduced tRNA[PHE] and tRNA[LEU1] levels, reduced mitochondrial protein translation, and a biochemical defect in the respiratory chain in fibroblasts (Connor et al., 2017). Another study investigated the possible role of CR mutations in cardiovascular disease with m.16145G>A and m.16311T>C mutations identified as potential genetic risk factors for stroke, while m.72T>C, m.73A>G and m.16356T>C mutations might act as possible beneficial genetic factors for myocardial infarction (Umbria et al., 2020).
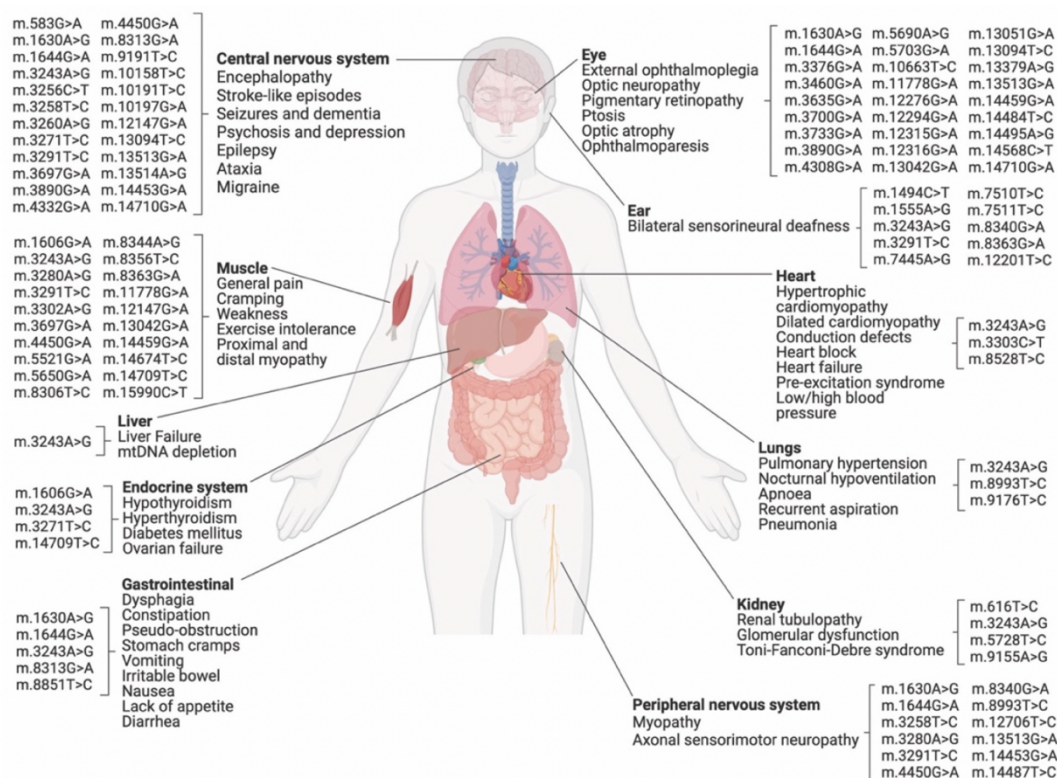
Figure 1.9 Mitochondrial DNA mutations associated with different diseases. Presented here are various mtDNA mutations causing mitochondrial diseases and their clinical features. These mutations can also be corrected using base editing technologies discussed in Section 1.4.3. Image from Kar et al., 2023. Licensed under Creative Commons Attribution (CC BY) license.

With further advancement of sequencing methodologies, the number of pathogenic variants will continually rise. In 2014, a genome-wide association study (GWAS) examining over 50,000 individuals with 11 major diseases (which include ankylosing spondylitis, ischemic stroke, multiple sclerosis, Parkinson's disease, primary biliary cirrhosis, psoriasis, Type-2

diabetes, coronary artery disease, hypertension, ulcerative colitis, schizophrenia) and healthy controls was performed to analyze the role of mtDNA variants in the said 11 diseases and results showed that mtDNA variants modifying the risk of developing one disease also modify the risk of developing other diseases (Hudson et al., 2014). As such, variants increasing the risk of two or more diseases were limited to (1) MT-CYB (m.14793, m.15218) encoding variants in cytochrome b (H16R, T158A) and (2) MT-CO3 (m.9477, m.9667) encoding variants in subunit 3 of cytochrome oxidase (complex IV, V91L, N154S) while the only non-synonymous protein encoding variant associate with reduced risk of several diseases was m.10398 in the MT-ND3 variant (complex I, T114A). The study also found that there were more functional variants associated with increased disease risk as compared to reduced risk.

1.4.2. Mouse models generated with mtDNA mutations.

Mitochondrial diseases are one of the most commonly occurring groups of inherited neurological disorders characterized by impaired mitochondrial OXPHOS resulting in energy deficiency and organ or multi-system dysfunction (Gorman et al., 2016; Macken, Vandrovcova, et al., 2021). Clinical management of symptoms have been implemented but effective treatments are still lacking (Pfeffer et al., 2013). To aid in understanding the mechanisms underlying mitochondrial diseases, several animal models exhibiting mitochondrial dysfunction have been developed (Kauppila et al., 2016; Ruzzenente et al., 2016; Trifunovic et al., 2004). The mouse is an important model to study human mitochondrial diseases since its genetic makeup is similar to that of humans. Physiologically, it also has circulatory, reproductive, digestive, hormonal, and nervous systems similar to humans (The Jackson Laboratory). Since mitochondrial diseases often affect postmitotic tissues, their physiological similarity is a big advantage (Ylikallio & Tyynismaa, 2015b). In addition, mice have a shorter life span (~2 years) compared to humans which makes it easier to evaluate the disease and its progression.

Interestingly, an established animal model Ndufs4 knockout (KO) mice with an impaired Complex I activity developing progressive encephalopathy, motor function decline, neuroinflammation, among other things, recapitulates human pathology associated with Leigh Syndrome (S. E. Kruse et al., 2008). Subsequent examination of different regions of the brains of Ndufs4 KO mice revealed that impairment of NDUFS4 led to a reduction in glutamate/α-ketoglutarate metabolism, which may contribute to the loss of specific neuronal populations (Johnson et al., 2020). Moreover, investigating the neuroimmune process has also shown that

depletion of microglial cells extended the life span and delayed the motor symptoms in Ndufs4 KO mice (Aguilar et al., 2022). Consequently, unlike the Ndufs4 KO mice, organoids or cells might not be able to give us insights into the cross-tissue or cross-organ mechanisms underlying mitochondrial diseases. Thus, developing mouse models is indeed necessary. However, at present, only a handful of mouse models with pathogenic mtDNA mutations were generated due to the difficulty in engineering the mitochondrial genome (reviewed in Dunn et al., 2012; Stewart, 2021). These obstacles consist of – the engineered mtDNA must be able to pass through the mitochondrial double membrane, reach a level of heteroplasmy for mitochondrial dysfunction to occur, and evade selective elimination of mtDNA molecules with decreased respiratory capability (reviewed in Dunn et al., 2012).

Modeling mitochondrial dysfunction and mitochondrial disease in mice employs several methods that either target the mtDNA or the nuclear-encoded genes involved in mtDNA replication and maintenance to produce specific pathogenic mtDNA mutations (reviewed in Stewart, 2021; Tyynismaa & Suomalainen, 2009). Direct manipulation of mtDNA, however, has proved to be challenging due to the inaccessibility within the mitochondrial double membranes, high copy number of mitochondria per cell, and minimal recombination (Dogan & Trifunovic, 2011; Tuppen et al., 2010). Indirect approaches were therefore used to introduce primary mtDNA mutations in mice. One way is by constructing transmitochondrial hybrids in which enucleated cells carrying altered mtDNA is fused with cells lacking mtDNA (ρ^0 cells) and introducing it to the mouse embryo. The following are some of the mouse models generated in this method: (1) Transmitochondrial mice carrying chloramphenicol-resistant (CAPr) mtDNA (with A2379T in the *16S* rRNA gene) with reduced Complex IV activity (Marchington et al., 1999). (2) Transmitochondrial 'mito-mice' carrying high levels of a heteroplasmic single mtDNA deletion was generated by isolating respiration-deficient cybrids with mtDNA carrying a deletion (ΔmtDNA4696) and introducing it to fertilized mouse embryos with enucleated cybrids through electrofusion (Inoue et al., 2000). The mutant mtDNA was maternally transmitted and the mice exhibited OXPHOS deficiency in the heart, skeletal muscle, and kidneys and developed anemia, myopathy, cardiomyopathy, deafness, and renal failure and died at 6 months. (3) Mice carrying two mutations in *COI* (T6589C, a mild mutation which is a missense mutation resulting in V421A) and *ND6* (13885insC, a severe mutation creating a frameshift mutation in ND6) showing germline selection against the severe mutation (Fan et al., 2008).

Manipulation of nuclear-encoded genes for mtDNA replication and maintenance involves constitutive or conditional gene knockout and transgenesis. The *Tfam* knockout mice

was developed by disrupting *Tfam* by targeting *loxP*-sites followed by excision of Tfam exons by *cre*-mediated recombination *in vivo* (Larsson et al., 1998). Heterozygous knockouts exhibited reduced mtDNA copy number, reduced mtDNA transcription, and respiratory dysfunction in the heart tissue. The 'Deletor' mice expressing mutant Twinkle cDNA carrying a mutation homologous to the mutation of human adult-onset progressive external ophthalmoplegia (PEO) (Tyynismaa et al., 2005). These mice exhibit accumulation of multiple mtDNA deletions leading to progressive respiratory dysfunction and late-onset mitochondrial disease (starting at 1 year old). Homozygous knock-in mice (*PolgA^{mut/mut}*), referred to as mtDNA-mutator mice, with an altered catalytic PolgA subunit containing alanine instead of aspartate residue of the second exonuclease domain (D257A), expresses PolgA proofreading-deficiency (Trifunovic et al., 2004). Compared to their WT siblings, these mice exhibit a threefold to fivefold increase in the levels of point mutations as well as an increase in deleted mtDNAs. The increase in point mutations was associated with COX deficiency in cardiomyocytes, heart enlargement, reduced fertility, and premature ageing. The mtDNA-mutator mice were further used to study the maternal transmission of random mtDNA mutations in the mouse germline with results showing that nonsynonymous mutations in protein-coding genes were strongly eliminated (Stewart et al., 2008). Mutations in mt-tRNA genes, however, are selected against in a lesser extent (Freyer et al., 2012). To transmit low levels of mtDNA mutations through the germline, heterozygous mtDNA-mutator (*PolgA^{wt/mut}*) female mice are a good resource (Ross et al., 2013a). One example is the generation of a mouse line with a pathogenic heteroplasmic m.5024C>T mutation in the tRNA^{ALA} gene using *PolgA^{wt/mut}* females bred with wild type males (Kauppila et al., 2016). Phenotypically, the C5024T mice exhibited reduced body mass in male mice and increased heart mass indicative of cardiomyopathy. As the mice age, selection against high levels of mt-tRNA^{ALA} mutations was observed in highly proliferative tissues, such as in colonic epithelium and blood. The resulting low-level mutations in the blood of older C5024T mice can also be seen in CPEO and m.3243A>G MELAS mutation. High levels of m.5024C>T mutation resulted in a substantial decrease in mt-tRNA^{ALA} levels, thereby impairing mt-tRNA^{ALA} stability, ultimately, leading to the impairment of mitochondrial translation (Kauppila et al., 2016).

Recently, a new technique used a bacterial cytidine deaminase enzyme, referred to as double-stranded DNA deaminase toxin A (DddA), to generate DddA-derived cytosine base editor (DdCBE) for mitochondrial base editing in human cells (HEK293T cells and U2OS cells) (Mok et al., 2020). The DddA_{tox} domain converts cytosine (C) to uracil (U) in dsDNA, however, this confers toxicity. To direct the DdCBE to the mitochondria and to inhibit the toxicity of

DddA$_{tox}$, the DdCBE consists of two constructs containing the following: DddA$_{tox}$ split in half, which is the inactivated toxin portion of DddA$_{tox}$, the dsDNA-binding TALE arrays, the mitochondrial targeting sequence directing the construct to the mitochondrial matrix, and the uracil glycosylase inhibitor (UGI) preventing the removal of uracil by uracil DNA glycosylase (UDG). Upon importation of the proteins into the mitochondrial matrix, the mitochondrial targeting sequence is lost. The two split DddA$_{tox}$ halves are brought together and activated by the binding of the TALE arrays to the mtDNA sequences. The DddA$_{tox}$ changes the targeted C into U. U is often taken out of the UDG, however, the UGI protein shields the altered base until DNA replication takes place. During replication, the DNA polymerase reads the U as a T resulting in the introduction of an A in the newly synthesized strand. DdCBEs, therefore, mediate C•G to T•A transitions. *In vivo* mitochondrial editing was performed in mouse using DdCBEs and has shown that mtDNA mutations generated can be transmitted to the next generation (Guo et al., 2022; Lee et al., 2021). The m.12918G>A mutation in MT-ND5 gene can cause various mitochondrial disorders in humans, as such, DdCBE pairs were injected into the mouse zygotes to generate the m.12918G>A mutation (Lee et al., 2021). Mimicking human mtDNA pathogenic mutations, mice with m.7763G>A and m.7741G>A mutations in mt-tRNA^{Lys} (in humans, m.8363G>A and m.8340G>A, respectively) and m.2820G>A in MT-ND1 and m.12918G>A in MT-ND5 (in humans, m.3376G>A and m.13513G>A, respectively) were generated by microinjection of DdCBE pairs' mRNA into mouse embryos with results showing that the said DdCBE-mediated mutations can be transmitted to the next generation and that off-target C•G to T•A transitions were detected at fairly high frequencies in spacing regions with specific DdCBE pairs (Guo et al., 2022).

1.4.3. Manipulation of mtDNA heteroplasmy

One of the approaches to target pathogenic mitochondrial genomes is by heteroplasmy shifting, wherein mtDNA heteroplasmy is shifted below the pathogenic threshold (reviewed in Jackson et al., 2020; Silva-Pinheiro & Minczuk, 2022). Over the years, several works have been directed on the use of nuclease-mediated mammalian mitochondrial genome engineering for heteroplasmy shifting in which specific nucleases are used to target the mutant mtDNA producing double-strand breaks, which will then be degraded, thus letting the wild type mtDNAs repopulate the mitochondria. The first experiments involved the use of mitochondrially targeted restriction endonucleases (mitoREs). A mitochondrially targeted PstI was engineered to cleave mtDNAs harboring PstI sites leading to the loss of the mitochondrial genome in cultured human cells (Srivastava & Moraes, 2001). This was also used in cultured

cells containing mouse mtDNA with PstI sites and rat mtDNA lacking PstI sites resulting in the accumulation of the rat mtDNA (Srivastava & Moraes, 2001). Complete elimination of the mutant mtDNA followed by repopulation of wild type mtDNA was observed using a mitochondrially targeted SmaI in cultured cells carrying m.8993T>G mutation (Tanaka et al., 2002). The m.8993T>G mutation is associated with neurogenic muscle weakness, ataxia and retinits pigmentosa (NARP), Leigh's disease, and hypertrophic cardiomyopathy. Another study also targeted the m.8993T>G mutation using mitoRE XmaI which resulted in the elimination of the mutant mtDNA (Alexeyev et al., 2008). In an *in vivo* study, a mitoRE ApaLI was expressed in cells of NZB/BALB heteroplasmic mice with the BALB mtDNA variant harboring an ApaLI site which resulted in BALB mtDNA depletion followed by NZB mtDNA repopulation (Bayona-Bafaluy et al., 2005). The use of mitoREs have proved to be a useful in tool in heteroplasmy shift towards elimination of mutant mtDNA, however, it is limited by the availability of pathogenic mutations known to introduce specific mitoRE site into the mtDNA. Additionally, when there is an extremely high mutation load, the elimination of mutant mtDNA may cause the mtDNA copy number to drop dangerously low.

Following MitoREs is the use of programmable mitochondrial nucleases, specifically, mitochondrially targeted zinc-finger nucleases (mtZFNs) and mitochondrially targeted transcription activator-like effector (TALE) nucleases (mitoTALENs). mtZFNs consist of engineered zinc finger nucleases (ZFNs) conjugated to *Fok*I restriction enzyme. Targeting the m.8993T>G mutation, an mtZFN was designed to cleave the mutant mtDNA resulting to reduced mutant mtDNA levels and subsequent repopulation of wild-type mtDNA (Gammage et al., 2014). A mtZFN was also designed to target the mtDNA deletion of 4977 bp, referred to as common deletion (CD), resulting in degradation of CD mtDNA and an increase of wild-type mtDNA proportion in cybrid cells rescuing the mitochondrial respiratory function (Gammage et al., 2014). Moreover, a study using mtZFN pairs, with mutant-specific monomer for the mutant mtDNA and wild-type-specific monomer for the adjacent sequence of the opposite strand, delivered by the adeno-associated virus in a heteroplasmic mouse model carrying pathogenic m.5024C>T exhibiting unstable mt-tRNA[Ala] levels successfully reduced the mutant mtDNA in the heart tissue and showed a significant increase in mt-tRNA[Ala] steady-state levels proportional to the heteroplasmy shifts observed in the mice and an improved mitochondrial metabolism (Gammage et al., 2018).

MitoTALENs consist of two monomers with a unique epitope tag and a mitochondria localization sequence at the N terminus with one monomer targeting the mutant sequence and the other monomer binding to the adjacent wild type mtDNA sequence. A mitoTALEN, referred

to as Δ5-mitoTALEN, was designed targeting the mutant mtDNA with ~5kb common deletion in human osteosarcoma cells that are heteroplasmic for the mtDNA common deletion (Bacman et al., 2013). This resulted in successfully decreasing the mtDNA deletion load. Another mitoTALEN, named 14459A-mitoTALEN, was constructed targeting the mutation m.14459G>A in MT-ND6 in osteosarcoma cybrid lines heteroplasmic for m.14459G>A (Bacman et al., 2013). Results showed a heteroplasmy shift with an increase in wild-type mtDNAs. A mitoTALEN, AAV9-mitoTALEN, was engineered to target and cleave m.5024C>T in mt-tRNA[Ala] (the same mouse model where mitoZFN was also designed) (Bacman et al., 2018). It was expressed *in vivo* through different ways of administration – intramuscular injection, systemic administration through retro-orbital injection, and intraperitoneal injection – which resulted in the AAV9-mitoTALEN being expressed in skeletal muscle and cardiac tissues. This led to a reduction of mutant mtDNA load and restoration of mt-tRNA[Ala] steady-state levels. Another gene editing platform was developed using mitochondrial-targeted meganucleases, referred to as mitoARCUS (Zekonyte et al., 2021). It was designed targeting the m.5024C>T mutation in the mt-tRNA[Ala] gene via intravenous injection using AAV9 vector and has shown effective mutant mtDNA elimination in liver and skeletal muscle resulting in mt-tRNA[Ala] level restoration (Zekonyte et al., 2021).

Another approach for heteroplasmy shifting is through base editing. The first type of base editing involves cytosine base editors. Cytidine deaminases catalyzing deamination of cytosine (C) to uracil (U) in Apolipoprotein B (apoB) mRNA were utilized in Drosophila, resulting in the generation of non-synonymous mutations using a mitochondrially-targeted cytidine deaminase, apoB mRNA editing catalytic polypeptide 1 (mito-APOBEC1) (Andreazza et al., 2019). It was then followed by the development of DddA-derived cytosine base editors (DdCBEs) facilitating C•G to T•A transitions (Mok et al., 2020). Since then, DdCBEs have been used in different organisms for mtDNA editing – in zebrafish (Guo et al., 2021; Sabharwal et al., 2021), mice (Lee et al., 2021), and human embryos (X. Chen et al., 2022). It is important to note, however, that DdCBEs can also lead to low-frequency off-target events on mtDNA and nDNA. Thousands of off-target single nucleotide variants (SNVs) enriched for C-to-T/G-to-A conversion are caused by DdCBE over the entire nuclear genome, which is twice as many as those caused by low-fidelity base editor BE3 (Wei et al., 2022). Improving the previously designed DdCBEs, Mok and colleagues used phage-assisted non-continuous and continuous evolution to evolve DddA variants with improved activity and expanded targeting scope. Results have shown that DddA6 and DddA11 enhanced the efficiency and utility of all-protein base editing (Mok et al., 2022). In addition, the DdCBEs were also used to knock out every

protein-coding gene of the mtDNA of mouse cells by introducing premature stop codons (Silva-Pinheiro et al., 2023). Another one is the development of Ddd_Ss-derived cytosine base editors (DdCBE_Ss) and introduction of mutations at multiple mtDNA loci. Finally, by introducing a single amino acid substitution from Ddd_Ss, the activity and sequence compatibility of DdCBE derived from DddA of *Burkholderia cenocepacia* (DdCBE_Bc) were improved (Mi et al., 2023). Engineered zinc finger deaminases (ZFDs) were then created following the development of DdCBEs (Lim et al., 2022). Optimized ZF-DdCBEs were delivered into the heart, skeletal muscle, and liver of post-natal mice with a single AAV9, to induce or correct disease-associated mutations in mitochondria and in the nucleus (Willis et al., 2022). Aside from cytosine base editors, mitochondrial adenine base editors were also reported. Custom-designed TALE DNA-binding arrays, referred to as TALE-linked deaminases (TALEDs), made of catalytically impaired, full-length DddA variant or split DddA and an engineered deoxyadenosine deaminase derived from the *E. coli* TadA protein induced targeted A-to-G editing in human mitochondria, with editing frequencies of up to 49% (Cho et al., 2022). mtDNA base editors (mitoBEs) combining a TALE-fused nickase and a deaminase for precise base editing generated A-to-G or C-to-T base editing with high specificity and efficiency of up to 77%, (Yi et al., 2023).

With the development and evolution of base editing technologies, along with clinical assessment, these have the potential to generate different animal models exhibiting mitochondrial diseases and aid in developing gene therapies. However, base editing does have a drawback, aside from off-targets, introduction of tRNA mutation in mice doesn't ensure that a phenotype will be obtained. Consequently, the approach we used in this thesis demonstrates COX-IV deficiency *a priori*.

2. RESEARCH AIMS

To better understand the mechanisms underlying mtDNA mutations and mitochondrial diseases, the generation of heteroplasmic mice with pathogenic mtDNA mutations is an important tool. However, heteroplasmic mice carrying pathogenic mtDNA mutations are not prevalent due to the difficulty in engineering the mitochondrial genome (Dunn et al., 2012; Stewart, 2021). One of the mouse models developed with increased levels of mtDNA point mutations is the mtDNA mutator mouse, exhibiting PolgA proofreading deficiency (Trifunovic et al., 2004). The mtDNA mutator mice were further used to study the maternal transmission of random mtDNA mutations in the mouse germline (Stewart et al., 2008). Consequently, the mtDNA mutator mice are a good resource for developing mouse lines with specific mtDNA mutations by breeding them with wild type strains to dilute the mtDNA mutations from the maternal line. Using this breeding methodology, in which heterozygous mtDNA mutator mice were bred with wild type mice in C57Bl/6NCrl background strain, a mouse line referred to as "tALA mice" or "C5024T mice" carrying a pathogenic heteroplasmic m.5024C>T mutation in the mt-tRNA[ALA] gene was developed which exhibits, among other things, increased heart mass indicative of cardiomyopathy, Complex IV deficiency in different tissues, a substantial decrease in mt-tRNA[ALA] levels and impairment of the mitochondrial translation (Kauppila et al., 2016)

To further study heteroplasmic mtDNA mutations *in vivo*, we developed a novel mouse model following the same breeding strategy in C5024T mice. Using this novel mouse model, henceforth denoted as "A5019G mice", we aim to answer the following:

1. What are the specific mtDNA mutations and their molecular and biochemical consequences in A5019G mice?
2. How do they affect the A5019G mice phenotypically?
3. With both mouse models carrying mt-tRNA[ALA] mutation, how do the A5019T mice compare to the previously characterized C5024T mice?

3. RESULTS

3.1. Identification of specific mtDNA mutations and their molecular and biochemical consequences

3.1.1. Generation of mouse line with pathogenic mtDNA mutations

The mtDNA-mutator mice (PolgA$^{MUT/MUT}$), which express a proofreading-deficient form of the catalytic subunit of nuclear-encoded mitochondrial DNA polymerase, PolgA^{D257A} (Trifunovic et al., 2004) can be used as a tool to generate mouse models of mtDNA disease (Kauppila et al., 2016). In both homozygous and heterozygous mice with the PolgA^{D257A} allele, mtDNA mutations were introduced in somatic tissues and germline by the proofreading deficient Polg (Ross et al., 2013b; Stewart et al., 2008). Female heterozygous mtDNA mutator mice (PolgA$^{+/MUT}$) transmit mtDNA mutations at about 1.34×10^{-4} mutations per base pair (Ross et al., 2013b) and these mice can be utilized to develop PolG-wild type mouse lineages carrying few linked mtDNA mutations (an average of 2-3 mutations per mtDNA). Kaupilla et al. generated mouse lines by crossing PolgA$^{+/MUT}$ males with wild-type C57BL/6NCrl females PolgA$^{+/+}$ to obtain PolgA$^{+/MUT}$ females, where wild-type mtDNA was reintroduced. The PolgA$^{+/MUT}$ females were then crossed with PolgA$^{+/+}$ males (1st backcross or N1) to generate founder females PolgA$^{+/+}$ with maternally inherited mtDNA mutations in a wild-type nuclear background. Subsequent backcrossing was performed to establish maternal lineages from the founder females (Kauppila et al., 2016). The mutant mice used in this thesis belong to one of the lineages in the mouse breeding (Figure 3.1).

3.1.2. Identification of mitochondrial dysfunction from colonic crypts of mutant mice

To determine the occurrence of mitochondrial dysfunction, the activity of the respiratory enzymes through histochemical analysis using cytochrome c oxidase/succinate dehydrogenase (COX/SDH) double labeling was performed in colonic crypts. Colonic crypts are tube-like glands found in the lining of the colon and rectum. Colonic (and small intestinal) crypts are used as they are prone to accumulate and clonally expand mitochondrial mutations, even in human and wild type mice (Greaves et al., 2011). Due to a small somatic bottleneck, a single crypt isolates and amplifies specific mtDNA mutations, allowing their identification and correlation with mitochondrial deficiency (Baines et al., 2014). Mitochondrial Complex IV dysfunction can be detected using a dual-step, COX/SDH histochemistry technique (Old & Johnson, 1989). Cells with normal functioning COX are stained brown from the localization of

the brown indamine polymer product in the mitochondrial cristae. Cells with low or absent COX activity, on the other hand, were not saturated by the brown product, but instead were stained blue from the visualization of SDH activity by reduction of nitroblue tetrazolium (NBT), an electron acceptor, to a blue formazan end product, indicating mitochondrial dysfunction (Old & Johnson, 1989). In the N3 and subsequent generations, COX/SDH screening was performed, and mitochondrial dysfunction was observed to be occurring in specific mouse maternal lineages (Figures 3.1 and 3.2).
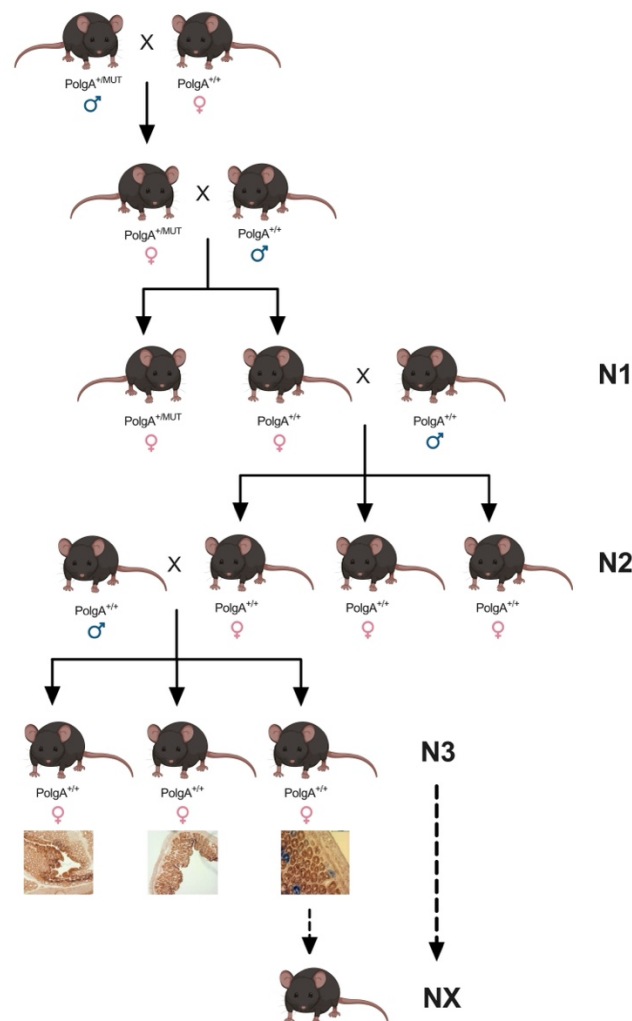
Figure 3.1 Breeding and screening of mouse lineages carrying mtDNA mutations. Heterozygous mutator mice (PolgA+/MUT) were used to introduce somatic mtDNA mutations. Further breeding was performed and starting from the N3 generation, screening of colonic crypts by COX/SDH staining was carried out to select mice with mitochondrial dysfunction. Adapted from Kauppila et al., 2016. Created with Biorender.com.
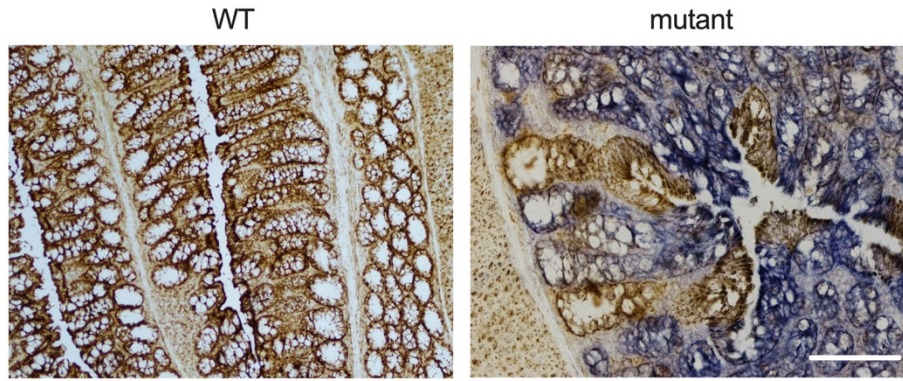
Figure 3.2 Mitochondrial dysfunction in colonic crypts of mutant mice. Colon tissue sections of WT and mutant mice stained using COX/SDH assay. Normal or COX-positive cells are shown in brown and COX-deficient cells are shown in blue. The scale bar represents 100 μm.

3.1.3. Identification of mtDNA mutations

With the detection of mitochondrial dysfunction in colonic crypts, crypts with normal COX activity and crypts with COX deficiency were then isolated individually using a laser-capture microdissection microscope. DNA was extracted and the whole length of mtDNA was amplified by PCR using 30 pairs of primers (Table 1 in Materials and Method chapter) and sequenced. Results revealed three mtDNA point mutations in a single mtDNA molecule cosegregating with mitochondrial deficiency: an A-to-G transition at position 5019 (m.5019A>G), an A-to-G transition at position 15200 (m.15200A>G), and an A-to-T transition at position 16232 (m.16232A>T) (Figures 3.3A and 3.3B). No further variants were found in the analysis of the mtDNA sequence.
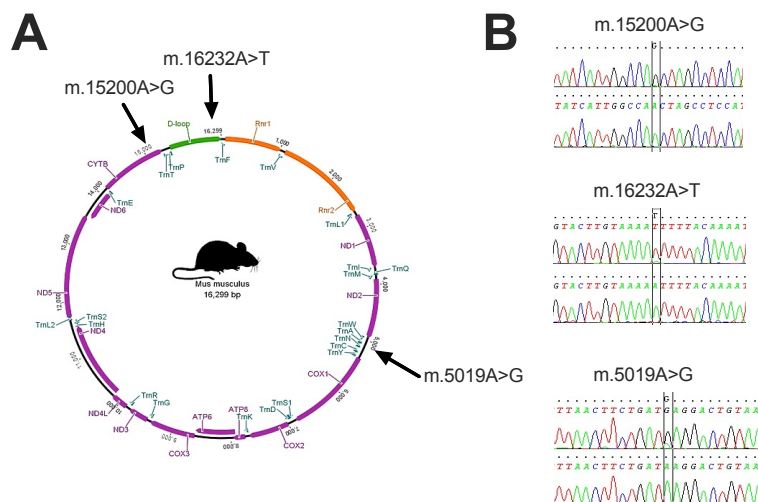
Figure 3.3 Mitochondrial DNA mutations in mutant mice. **A.** Location of the identified mtDNA mutations in the mouse mitochondrial genome. **B.** Sequencing reads of the three mutations.

The m.5019A>G mutation is located in the mitochondrial tRNA Alanine (mt-tRNA^Ala) gene (Figure 3.4A). To quantify the levels of the m.5019A>G mutation in colonic crypts and tissues, a pyrosequencing method was used. The mutation is predicted to produce a canonical G-C pairing compared to the naturally occurring wobble G-U pairing in the secondary structure of mt-tRNA^Ala, which will unlikely influence its stability. However, the mutation is situated in the acceptor stem which might affect the mt-tRNA^Ala aminoacylation (Figure 3.4B). Aminoacylation is the charging or pairing of the tRNA with its cognate amino acid.

Figure 3.4 m.5019A>G mutation in mt-tRNA^ALA. A. DNA sequence alignment between the WT reference sequence and several sequences from mutant animals showing the m.5019A>G mutation. Matching residues are displayed as dots. R represents an alignment with A and a G at the same position. **B.** Secondary structure of mt-tRNA^ALA with the arrow showing the location of the mutation in the acceptor stem. Created with BioRender.com.

Mitochondrial tRNA genes are over-represented in pathogenic mtDNA mutations compared to protein genes or rRNA genes, with more than 200 mt-tRNA mutations associated to various diseases due to the inhibition of tRNA aminoacylation (Abbott et al., 2014). In the Mitomap, 15 mutations are listed located in mt-tRNA[ALA] that have possible disease association (Supplementary Table 1). Of these, one is very strongly suspected to be pathogenic – the m.5650G>A mutation in the aminoacyl stem of the tRNA associated with myopathy. Another one is likely to be pathogenic, the m.5628T>C mutation associated with CPEO, DEAF enhancer, gout, and tic disorder. And five might be pathogenic, the m.5591G>A, m.5595G>A, m.5613T>C, m.5636T>C, and m.5652C>G mutations. The m.5650G>A mutation has been first reported from a patient with cerebral autosomal dominant arteriopathy with subcortical infarcts and leukoencephalopathy (CADASIL), who was also exhibiting myopathy with ragged-red fibers (Finnilä et al., 2001). The CADASIL was due to R133C mutation in *Notch3* and the myopathy was due to the mutation in the mt-tRNA[ALA] gene, the m. 5650G>A mutation, which modifies a segment in the mt-tRNA[ALA] acceptor stem. In another study, the m. 5650G>A mutation was subsequently defined in a young patient with reported severe proximal (limb-girdle) myopathy. Interestingly, the mother had relative mutation levels of the same mutation that matched or exceeded the afflicted daughter, and extensive COX-deficient muscle fibers. However, at the time of the diagnosis of the daughter, the mother did not suffer from myopathy but was identified to have mild mitochondrial disease symptoms (McFarland et al., 2008).

The m.15200A>G mutation is located in the Cytochrome b gene (Figure 3.5A). Since it is synonymous at amino acid Q352 in Cytb, it does not interfere with mitochondrial function (Figure 3.5B).

The m.16232A>T is located in the control region (CR), specifically in the light strand promoter (LSP) (Figure 3.6A). The CR plays a vital role in the regulation of mtDNA gene expression. Transcription initiation and synthesis of primer for mtDNA replication occur in the LSP (Chang & Clayton, 1986; Hixson & Clayton, 1985). The mutation, therefore, may have an effect on the transcription and/or replication of the mtDNA (Figure 3.6B).

Few patient mutations in the CR have been conclusively linked to diseases. One of these mutations is the m.547A>T, a homoplasmic substitution in the heavy strand promoter (HSP) that was identified in an analysis of pedigree with maternally inherited tubulointerstitial kidney disease (Connor et al., 2017). Tubulointerstitial kidney disease, a cause of progressive renal failure, is characterized by bland urinary sediment and histological evidence of interstitial fibrosis and tubular atrophy. The mutation altered transcription and impaired the activity of

HSP. Reduced levels of mt-tRNA[Phe] were also observed resulting in a defect in mitochondrial protein synthesis and a biochemical defect in the respiratory chain.

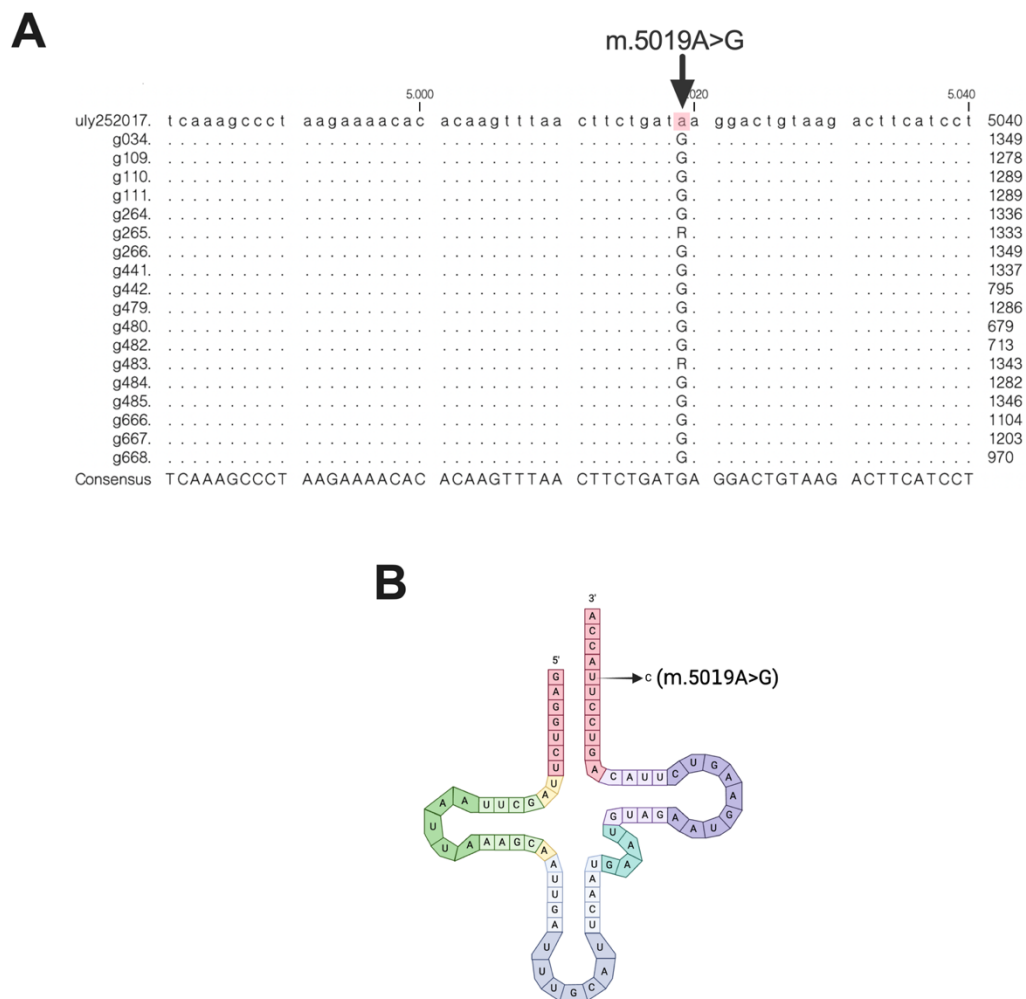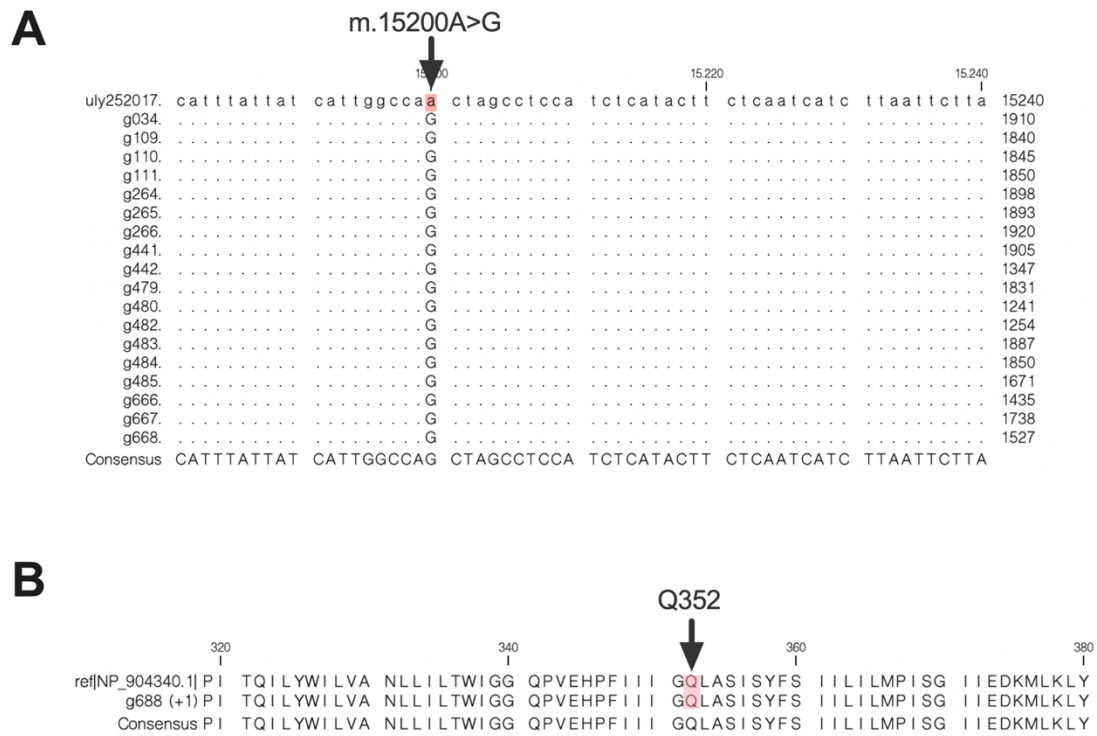**Figure 3.5 m.15200A>G mutation in Cytochrome b. A.** DNA sequence alignment between the WT reference sequence and several sequences from mutant animals showing the m.15200A>G mutation. Matching residues are displayed as dots. **B.** Protein sequence alignment between the WT reference sequence and mutant sequence reveals that the m.15200A>G mutation does not result in an amino acid change in Q352.

A

m.16232A>T

```
uly252017.  caaaatatgacttatattttagtacttgtaaaaatttacaaaatcatgttccgtgaacc  16258
    g034.   ...........................................T...........................  2907
    g109.   ...........................................T...........................  2841
    g110.   ...........................................T...........................  2834
    g111.   ...........................................T...........................  2840
    g264.   ...........................................T...........................  2898
    g265.   ...........................................T...........................  2894
    g266.   ...........................................T...........................  2918
    g441.   ...........................................T...........................  2923
    g442.   ...........................................T...........................  2336
    g479.   ...........................................T...........................  2820
    g480.   ...........................................T...........................  2259
    g482.   ...........................................T...........................  2255
    g483.   ...........................................W...........................  2875
    g484.   ...........................................T...........................  2850
    g485.   ...........................................T...........................  2670
    g666.   ...........................................T...........................  2431
    g667.   ...........................................T...........................  2725
    g668.   ...........................................T...........................  2518
Consensus   CAAAATATGACTTATATTTTAGTACTTGTAAAATTTTTACAAAATCATGTTCCGTGAACC
```

B

m.16232A>T

Figure 3.6 m.16232A>T mutation in the LSP region. A. DNA sequence alignment between the WT reference sequence and several sequences from mutant animals showing the m.16232A>T mutation. Matching residues are displayed as dots. W represents an alignment with T, U, and A. **B.** Location of the mutation (displayed by the arrow) and its proximity to the TFAM and Polrmt binding sites. Adapted from Posse et al., 2014. Created with BioRender.com.

3.1.4. m.16232A>T results in mild suppression of transcription initiation in vitro

To determine the effect of m.16232A>T mutation in mitochondrial transcription, *in vitro* transcription assay was conducted by the Falkenberg lab at Gothenburg University, Sweden. LSP templates of WT and with m.16232A>T mutation were constructed. One construct consisted of WT and WT promoters and the other with WT and m.16232A>T promoters (Figure 3.7A). TFAM, POLRMT, and TFB2M were subsequently added to simulate mitochondrial transcription. After the addition of ribonucleotide triphosphates (rNTPs), the reaction was incubated and stopped at different time intervals (0, 2, 5, and 10 min). Samples were then heated, separated in polyacrylamide gel, and viewed using phosphoimager. Results showed that at different DNA/TFAM concentrations (50, 25, 12, and 6 bp of mtDNA bp/molecule of

TFAM), the promoter with m.16232A>T mutation had a lower transcription rate compared to the WT promoter (Figure 3.7B). Specifically, at 12 bp mtDNA/TFAM molecule, a 20% decrease was observed in the promoter with m.16232A>T mutation (Figure 3.7C). Stopping the reaction at different time points also showed that the promoter with m.16232A>T mutation had a slower rate of transcription initiation at time points 5, 7.5, and 10 min (Figures 3.7D and 3.7E).
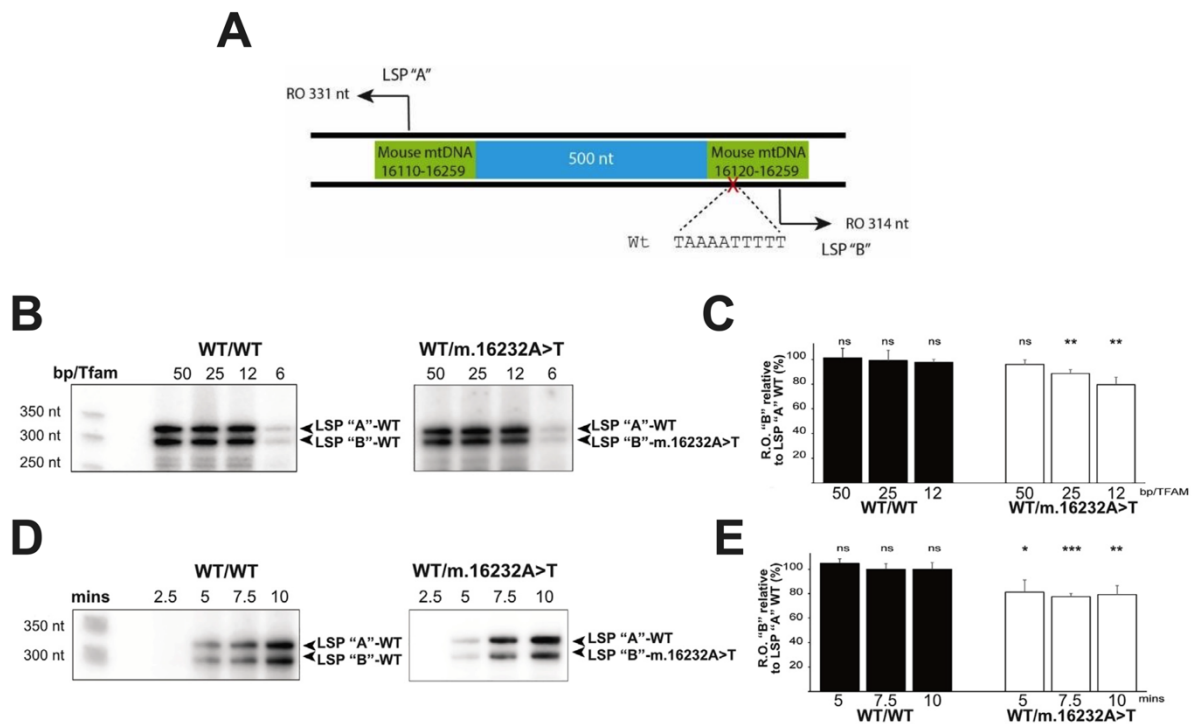
Figure 3.7 Analysis of transcription initiation *in vitro*. A. Schematic diagram of the construct carrying the m.16232A>T mutation. **B.** Comparison of transcription rate between WT LSP and LSP carrying m.16232A>T with different TFAM concentrations. Autoradiographs of wild-type (WT) and m.16232A>T transcripts at different DNA/Tfam concentrations. The left autoradiogram consisted of two WT promoters while the right autoradiogram consisted of WT and m.116232A>T promoters. **C.** Quantification of autoradiographs in B. **D.** Autoradiographs showing transcription initiation at different time points. The left autoradiograph consisted of two WT promoters while the right autoradiograph consisted of WT and m.116232A>T promoters. **E.** Quantification of autoradiographs in D. Data by Diaz and Falkenberg. Published article by Burr et al., 2023.

These *in vitro* transcription assay experiments revealed that the m.16232A>T mutation resulted in a very little reduction in transcription initiation and was lessened by adding more TFAM to the transcribed template.

3.1.5. Stable mitochondrial mRNA steady-state levels and mtDNA copy number in heart and intestinal epithelial tissues

To determine if the mild suppression of transcription initiation affects the mitochondrial transcriptome, steady-state levels of mitochondrial messenger RNAs (mt-mRNAs) were analyzed using the small intestinal epithelial tissue, which is highly regenerative. RNA was isolated from age-matched WT and A5019G mice and northern blot analyses were performed. Results showed that *mt-Nd5* and *mt-Co3* steady-state levels were not significantly different from that of the WT controls (Figures 3.8A and 3.8B). Steady-state transcript levels of *mt-Nd5*, *mt-Co2*, *mt-Co3*, and *mt-Atp6* were measured through reverse transcription qPCR (qRT-PCR) and confirmed the results of the northern blot analyses (Figure 3.8C). These results revealed that steady-state levels of mt-mRNAs are not reduced in the A5019G mice, so they are not affected by the mild reduction in transcription initiation efficiency of the m.16232A>T mutation.

Southern blot analyses of the mtDNA level were performed in small intestinal epithelial tissue and heart tissue of WT and A5019G mice. mtDNA level was stable in the small intestinal epithelial tissue (Figures 3.9A and 3.9B). Mitochondrial DNA copy number was measured using qPCR with the following probes: *mt-Co1*, *mt-Co3*, and *mt-Nd4*. Increased copy number was observed in A5019G mice as compared to WT mice (Figure 3.9E). In the heart, mtDNA level was also stable (Figures 3.9C and 3.9D). It was also supported by the qPCR data using *mt-Cyb*, *mt-Nd5*, *mt-Nd6*, and *mt-Atp6* probes which also showed no significant changes in mtDNA copy number (Figure 3.9F). We, therefore, conclude that the very mild decrease in transcription initiation observed *in vitro* has no impact on the copy number of mtDNA *in vivo*.

Overall, the findings of the experiments – *in vitro* transcription assay, mt-mRNA steady-state levels, and mtDNA copy number – indicate that, although a contributing role cannot be ruled out, the m.16232A>T mutation is not likely the major pathogenic mutation causing mitochondrial dysfunction.
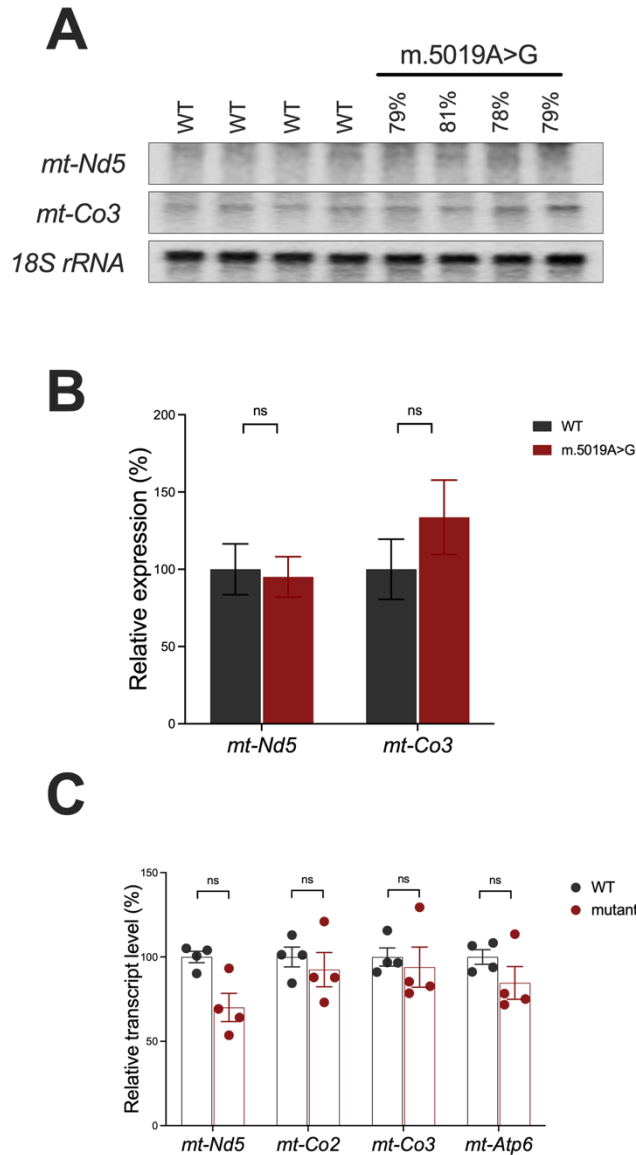
Figure 3.8 Steady-state levels of mt-mRNAs are stable in A5019G mice. A. Northern blot analyses of *mt-Nd5* and *mt-Co3* transcript levels in small intestinal epithelial tissue of WT and high-level m.5019A>G mutation mice at 46 to 53 weeks. Loading control *18S* rRNA. **B.** Quantification of Northern blotting in A. Values normalized to *18S* rRNA. Error bars ± SEM. Mann-Whitney U Test; ns not significant. **C.** RT-qPCR analysis *of mt-Nd5*, *mt-Co2*, *mt-Co3*, and *mt-Atp6* transcript levels in the small intestinal epithelial tissue of WT and high-level m.5019A>G mutation mice at 46 to 53 weeks. Values normalized to *18S* rRNA. Error bars ± SEM. Two-way ANOVA; ns not significant.
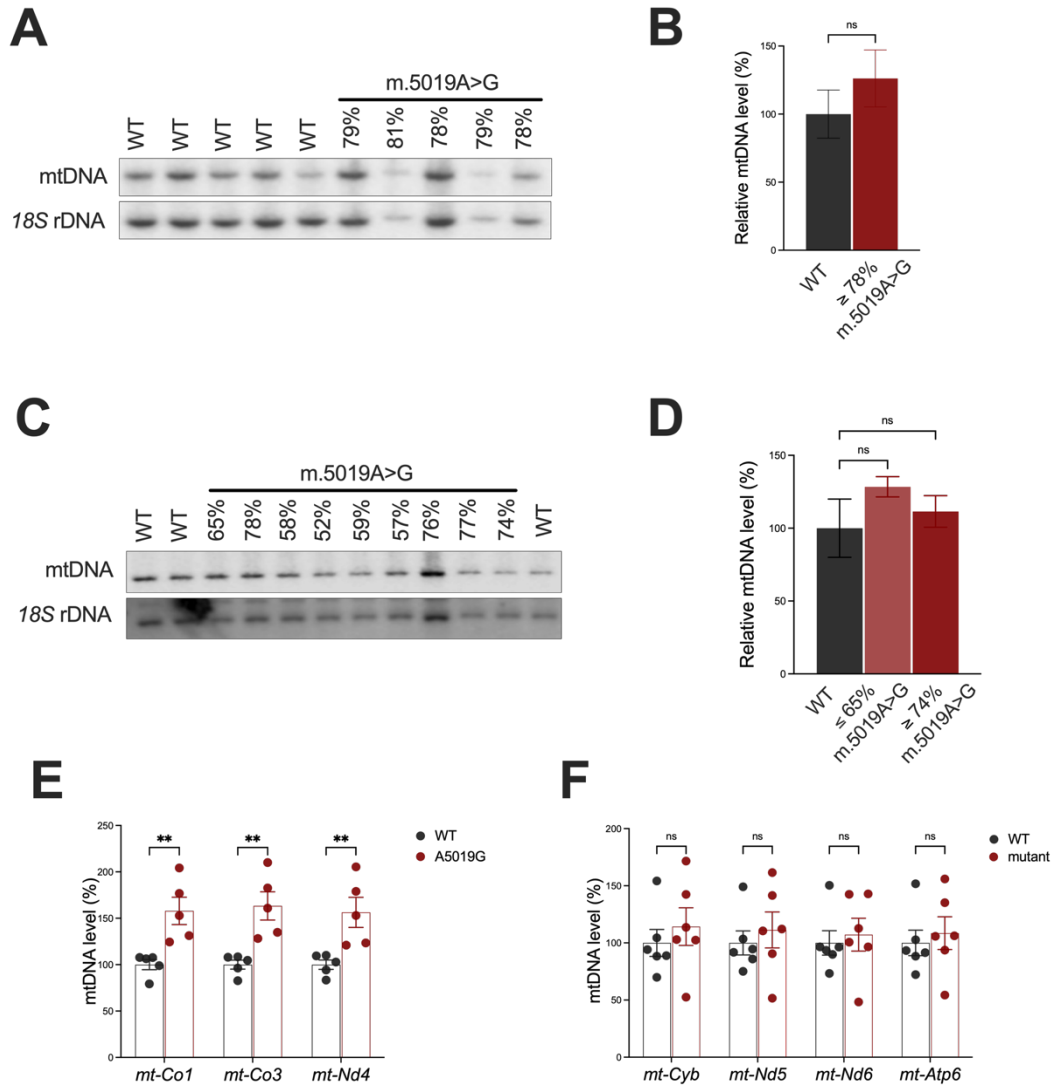
Figure 3.9 mtDNA copy number is not reduced in A5019G mice. A. Southern blot analysis of mtDNA levels in small intestinal epithelial tissue of WT and high-level m.5019A>G mutation mice at 50 to 60 weeks. Loading control: 18S rDNA. **B.** Quantification of Southern blotting in A. Values normalized to 18S rDNA. Error bars ± SEM. Mann-Whitney U Test; ns not significant. **C.** Southern blot analysis of mtDNA levels in heart tissue of WT and low- and high-level m.5019A>G mutation mice at 29 to 37 weeks. Loading control: 18S rDNA. **D.** Quantification of Southern blotting in C. Values normalized to 18S rDNA. Error bars ± SEM. Kruskal-Wallis Test; ns not significant. **E.** qPCR analysis of mtDNA levels in small intestinal epithelial tissue of WT and high-level m.5019A>G mutation mice at 50 to 60 weeks. Values normalized to 18S rDNA. Error bars ± SEM. Two-way ANOVA; ** $p < 0.005$. **F.** qPCR analysis of mtDNA levels in heart tissue of WT and high-level m.5019A>G mutation mice at 29 to 36 weeks. Values normalized to 18S rDNA. Error bars ± SEM. Two-way ANOVA; * $p < 0.05$, ** $p < 0.01$.

3.1.6. m.5019A>G affects mt-tRNA^ALA aminoacylation but not mt-tRNA^ALA stability

Since the m.5019A>G mutation is located in the acceptor stem of mt-tRNA^ALA, we investigated the effects of m.5019A>G on the aminoacylation and stability of mt-tRNA^ALA. The aminoacylation processes for tRNAs ensure that the correct amino acid is charged to the

correct tRNA. The amino acid is covalently attached to the 3' end of the tRNA and the charged tRNA is released and is ready to decode mRNA codons together with ribosomes. An aminoacylation assay was carried out by the Minczuk lab, MRC Mitochondrial Biology Unit, Cambridge, UK on SV-40 antigen transfection-immortalized Mouse Embryonic Fibroblast (MEF) derived from A5019G and WT mice. RNA preparations were subjected to periodate oxidation. Periodate oxidation of the 3′ end is specific to uncharged tRNAs, effectively inactivating the 3′ end for any further enzymatic reaction. The loss or retention of the 3' terminal nucleotide was then determined through PAGE and northern blotting. The occurrence of deacylation is shown by the size shift of a band in the deacylated control treated with NaIO₄. A band corresponding to deacylated mt-tRNA^{ALA} was observed in MEFs with 95% and 100% m.5019A>G mutation but not in WT showing that m.5019A>G mutation affects the aminoacylation of mt-tRNA^{ALA} (Figure 3.10).
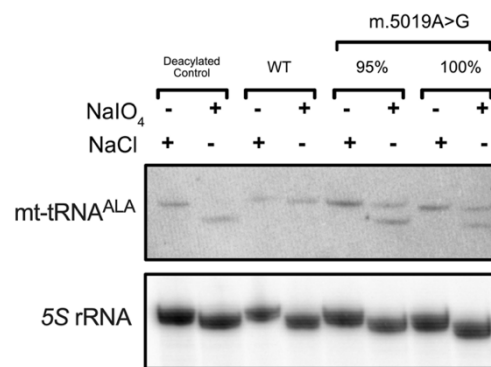
Figure 3.10 Occurrence of deacylation in mt-tRNA^{ALA} of MEFs carrying m.5019A>G mutation. Analysis of periodate (NaIO₄)-treated mt-tRNA^{ALA} subjected to gel electrophoresis. Loading control: 5S rRNA. Data by Nash, Powel, and Minczuk.

Steady-state levels of mitochondrial transfer RNAs (mt-tRNAs) were also analyzed to determine the effect of m.5019A>G mutation on mt-tRNA stability. Total RNA was isolated from heart tissue and small intestinal epithelial tissue of WT and A5019G mice with high m.5019A>G mutation levels, ranging from 77% to 86%. Mouse-specific biotin-labeled oligonucleotides were used to hybridize mt-tRNAs. Results showed that there was no difference in steady-state levels of mt-tRNAs located in LS and HS of A5019G and WT heart tissues (Figures 3.11A and 3.11B). Furthermore, in contrast to our observation with C5024T mice (with m.5024C>T mutation levels at 74% and 76%) (Kauppila et al., 2016), presenting significantly decreased mt-tRNA^{ALA} steady-state levels, A5019G mice (with m.5019A>G mutation levels at ≥77%) showed stable mt-tRNA^{ALA} steady-state levels (Figures 3.11C and

3.11D). mt-tRNA^ALA levels were also stable in the intestinal epithelial tissue of A5019G mice with ≥78% m.5019A>G mutation levels (Figures 3.11E and 3.11F). Taken together, these results showed that m.5019A>G does not affect mt-tRNA stability, more specifically mt-tRNA^ALA stability in both post-mitotic and highly proliferating tissues.
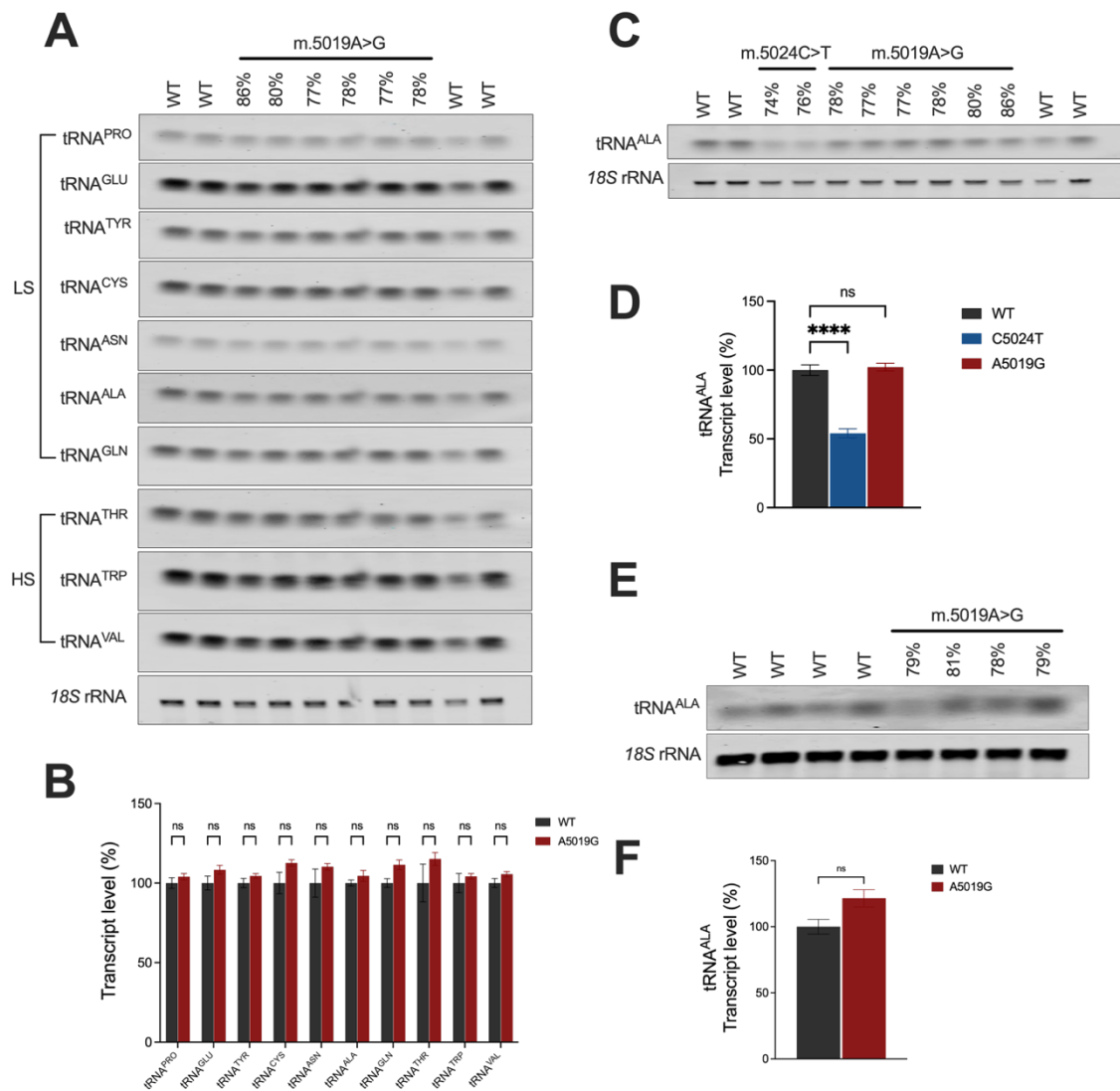
Figure 3.11 Steady-state levels of mt-tRNA^ALA are stable A5019G mice. A. Northern blot analyses and quantification of mt-tRNAs in heart tissue of WT and high-level m.5019A>G mutation mice at 29 to 36 weeks. Loading control: *18S* rRNA. **B.** Quantification of Northern blotting in A. Values normalized to *18S* rRNA. Error bars ± SEM. Mann-Whitney *U* test; ns not significant. **C.** Northern blot analyses of mt-tRNA^ALA in heart tissue of WT, C5024T, and A5019G mice at 29 to 36 weeks. Loading control: *18S* rRNA. **D.** Quantification of Northern blotting in C. Values normalized to *18S* rRNA. Error bars ± SEM. One-way ANOVA; **** $p < 0.0001$, ns not significant. **E.** Northern blot analyses of mt-tRNA^ALA in small intestinal epithelial tissue of WT and high-level m.5019A>G mutation mice at 46 to 52 weeks. Loading control: *18S* rRNA. **F.** Quantification of Northern blotting in E. Values normalized to *18S* rRNA. Error bars ± SEM. Mann-Whitney *U* test F; ns not significant.

3.1.7. m.5019A>G does not disrupt in organellar mitochondrial translation

The mitochondrial translation efficiency was then assessed by performing *in organello* translation carried out by Nina Bonekamp from our lab. 47 to 49-week-old mice harboring high levels of m.5019A>G mutation (79-82%) and age-matched WTs. Newly synthesized mitochondrial proteins were radiolabeled with [^{35}S] methionine/cysteine mix in the presence of emetine, a cytoribosome-specific inhibitor to ensure that the radiolabeled amino acids are incorporated only in the mitochondrial ribosome-synthesized polypeptides. The radiolabeled mitochondrial translation products were then separated by SDS-polyacrylamide gel electrophoresis and evaluated by autoradiography. Herewith, aberrant mitochondrial translation products were not observed in both tissues indicating that m.5019A>G mutation does not result in an *in* organellar translation defect (Figure 3.12A and 3.12B).
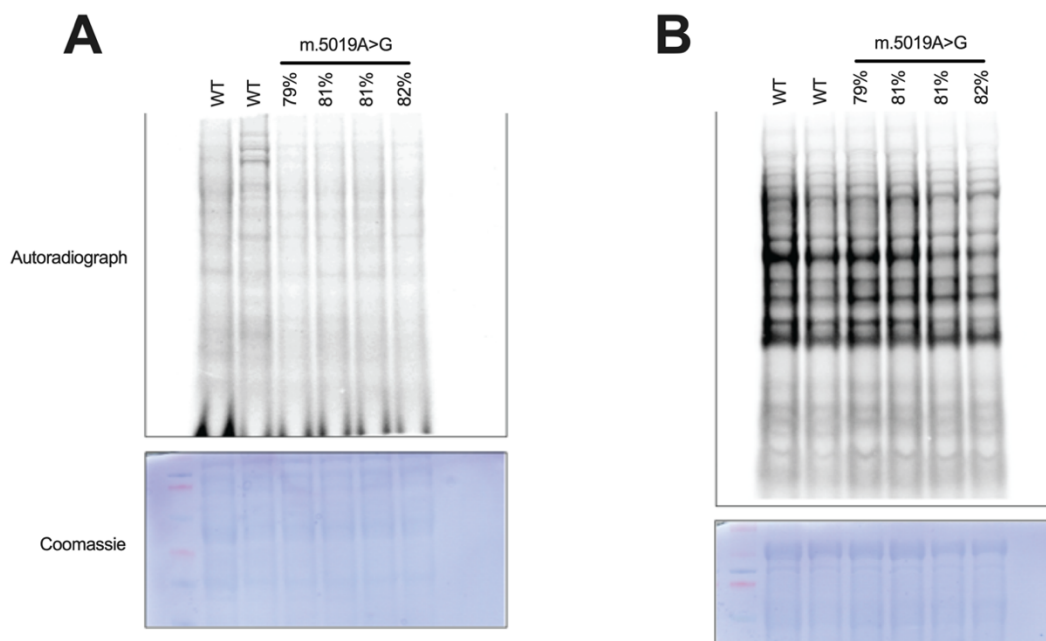
Figure 3.12 m.5019A>G does not impair in organellar mitochondrial translation. A. *In organello* translation assay using heart tissue of WT and A5019G mice. **B.** *In organello* translation using liver tissue of WT and A5019G mice. Both assays show normal translation products demonstrating the absence of in organellar translation defect. Gel images at the bottom display gel staining with Coomassie for loading control. Data by Nina Bonekamp.

3.2. Effects of mtDNA mutations in A5019G mice

3.2.1. Physiological and metabolic characteristics of A5019G mice

After investigating the functional consequences of the identified mtDNA mutations, we then evaluated whether physiological and metabolic changes were present in the A5019G mice. Indirect calorimetry was performed in WT and A5019G mice with ≥77% m.5019A>G mutation levels at 26 to 31 weeks and at 42 to 60 weeks to measure metabolic, behavioral, and physiological parameters. The mice were placed in metabolic cages (PhenoMaster) and allowed to acclimatize for 48 h before the readings were taken. For each age group, 12 mice per genotype (6 males and 6 females) were used. Different parameters were measured, and raw data was imported to *Cal*R software (Mina et al., 2018) to visualize and analyze the results. Respiratory gases, volume of oxygen consumption (VO2) and volume of carbon dioxide production (VCO2), were consistently lower in A5019G mice than the WT counterparts in both age groups but were not statistically different (Figures 3.13A-B and 3.14A-B). The respiratory exchange ratio (RER=VCO2/VO2), which indirectly shows the muscle's oxidative capacity to get energy, was the same between genotypes (Figure 3.13C and 3.14C). Food intake of 26-31-week-old A5019G mice at full day and light cycle was lower compared to WT (Figure 3.15A). All the other parameters, which include water intake, energy expenditure, locomotor activity, and ambulatory activity, were not significantly different between the genotypes (Figure 3.15A-C). For 42-60-week-old A5019G mice, food and water intake were higher than WT during the light cycle (Figure 3.16A). Locomotor and ambulatory activities were also higher in A5019G mice in full day, dark, and light cycles (Figure 3.16C). However, even though the activities were higher, the energy expenditure remained the same as that of the WT mice (Figure 3.16B).

Body weight and heart weight of 21 to 36-week-old and 49 to 68-week-old mice were also measured. Each age group consisted of WT (9 males and 9 females) and A5019G mice (9 males and 9 females) with ≥76% m.5019A>G mutation levels (Supplementary Table 2). At 21 to 36 weeks, no difference in body weight was observed in both A5019G males and A5019G females and their age-matched WTs (31.6 ± 1.0 g for A5019G males vs 33.3 ± 0.9 g for WT males; 24.3 ± 0.9 g for A5019G females vs 28.6 ± 1.6 g for WT females) (Figure 3.17A). At 49 to 68 weeks, A5019G males exhibited significantly lower body weight (30.1 ± 1.3 g) compared to WT males (46.5 ± 1.6 g) while there was no difference between A5019G females (26.5 ± 1.1 g) and WT females (32.5 ± 1.4 g) (Figure 3.17A). No significant difference in heart weights after sacrifice, between A5019G males (0.154 ± 0.006 g at 20-36 weeks; 0.176 ± 0.005 g at 49-68 weeks) and WT males (0.140 ± 0.004 g at 20-36 weeks; 0.177 ± 0.008 g at

49-68 weeks) and between A5019G females (0.135 ± 0.006 g at 20-36 weeks; 0.155 ± 0.010 g at 49-68 weeks) and WT females (0.122 ± 0.005 g at 20-36 weeks; 0.137 ± 0.005 g at 49-68 weeks) were observed in both age groups indicating that cardiomyopathy is not occurring in A5019G mice (Figure 3.17B).
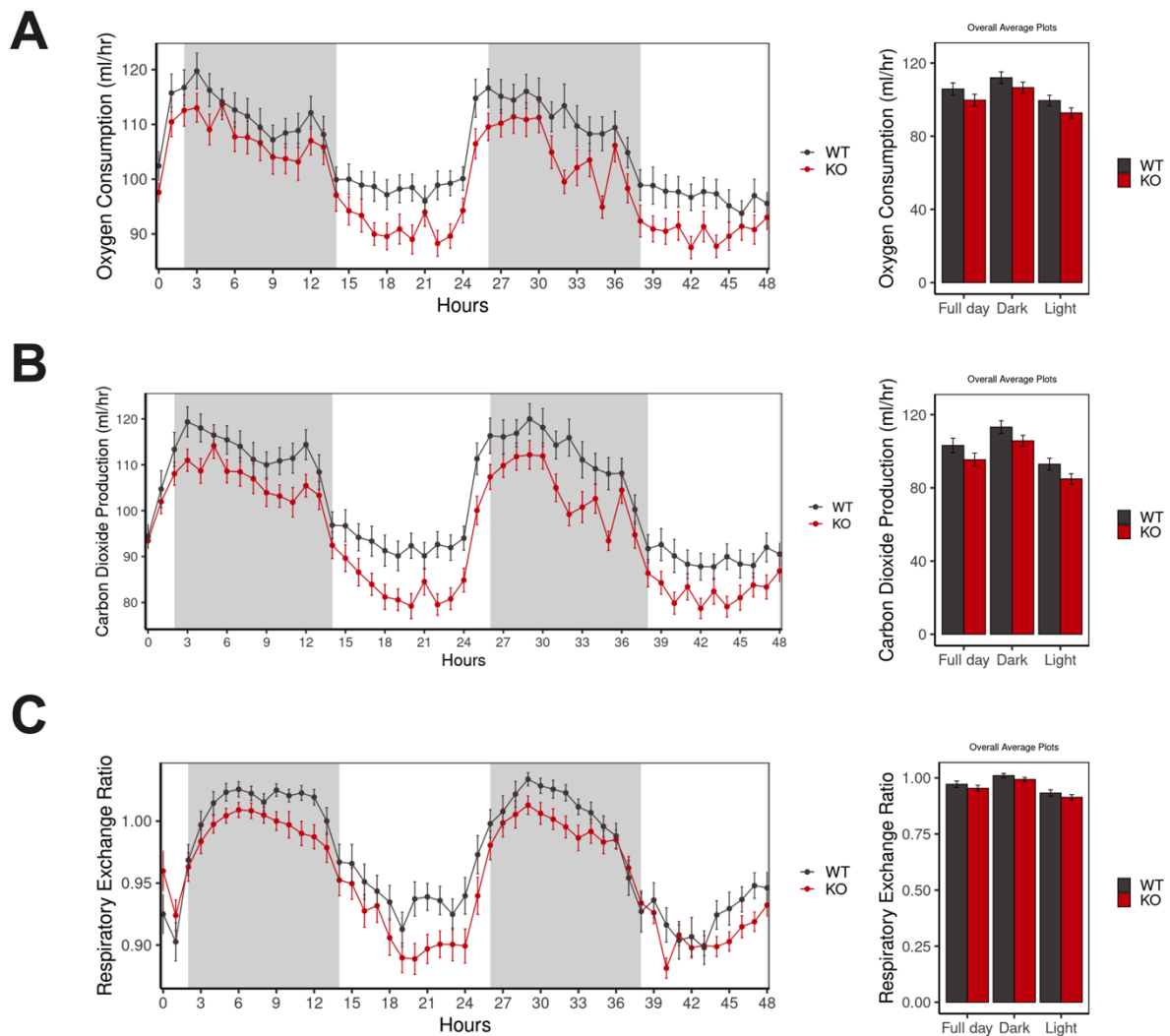
Figure 3.13 Indirect calorimetry analysis of WT and A5019G mice at 26 to 31 weeks. A. Mean whole-body oxygen consumption rate. **B.** Mean whole-body carbon dioxide production rate. **C.** Mean respiratory exchange ratio (RER). Measurements recorded on a cycle of dark (6:30 PM to 6:29 AM) and light (6:30 AM to 6:29 PM). n=12 per group. Error bars ± SEM. ANOVA.
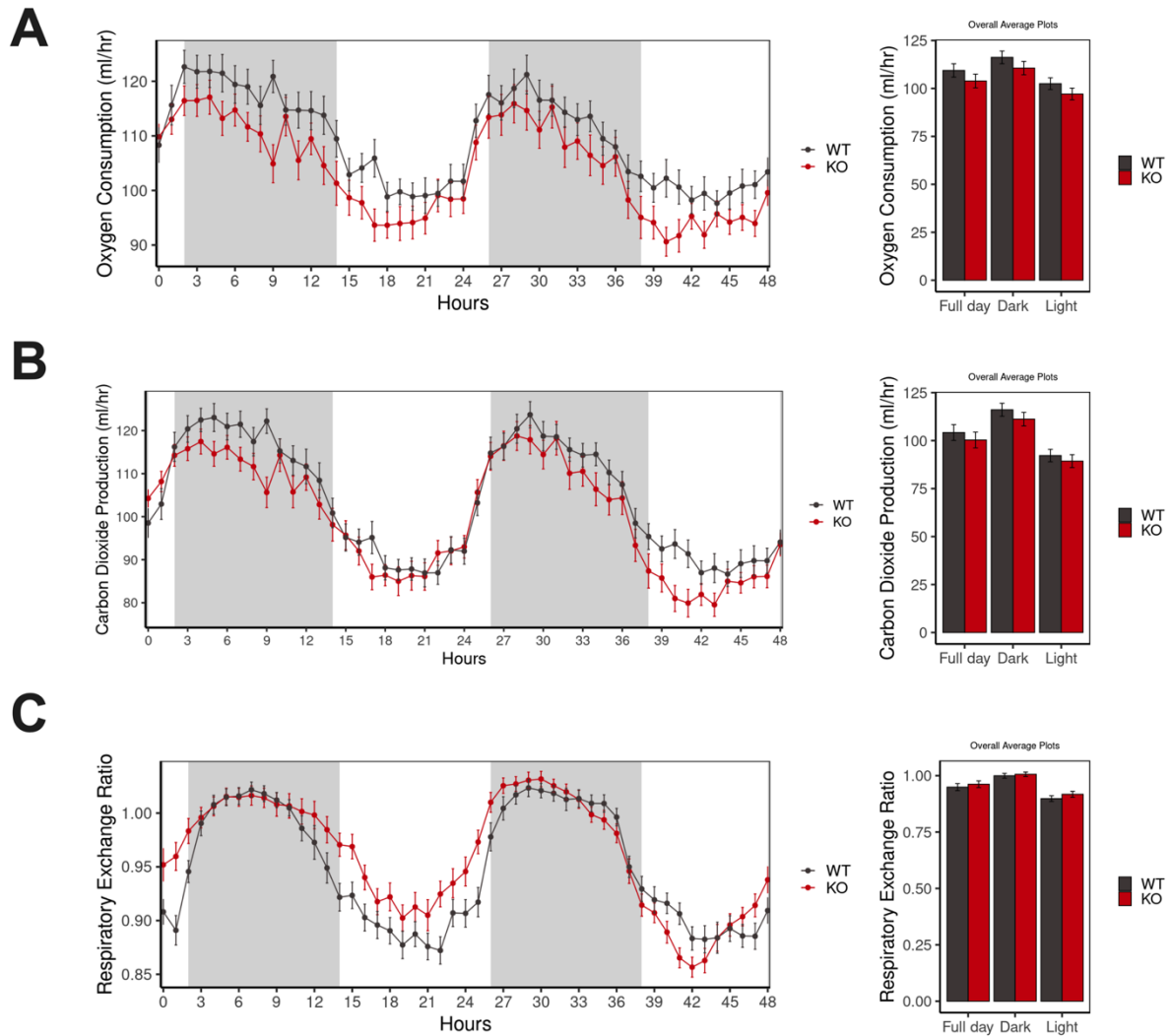
Figure 3.14 Indirect calorimetry analysis of WT and A5019G mice at 42 to 60 weeks. A. Mean whole-body oxygen consumption rate. **B.** Mean whole-body carbon dioxide production rate. **C.** Mean respiratory exchange ratio (RER). Measurements recorded on a cycle of dark (6:30 PM to 6:29 AM) and light (6:30 AM to 6:29 PM). Gray background represents dark photoperiod, white background represents light photoperiod. n=12 per group. Error bars ± SEM. ANOVA.
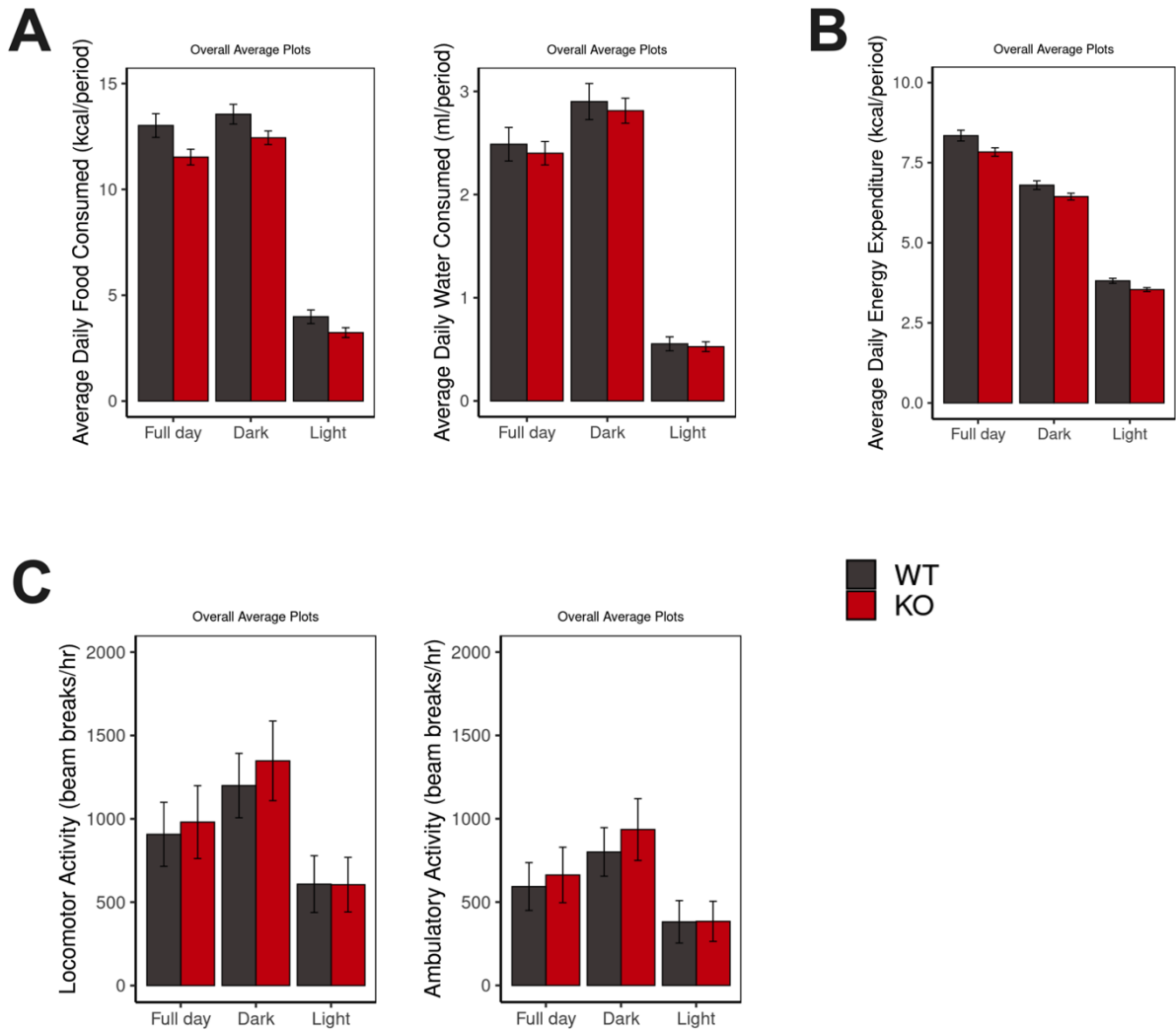
Figure 3.15 Indirect calorimetry analysis of WT and A5019G mice at 26 to 31 weeks. A. Average daily food and water consumption. **B.** Average daily energy expenditure. **C.** Locomotor and ambulatory activities. Measurements recorded on a cycle of dark (6:30 PM to 6:29 AM) and light (6:30 AM to 6:29 PM). n=12 per group. Error bars ± SEM. ANOVA.
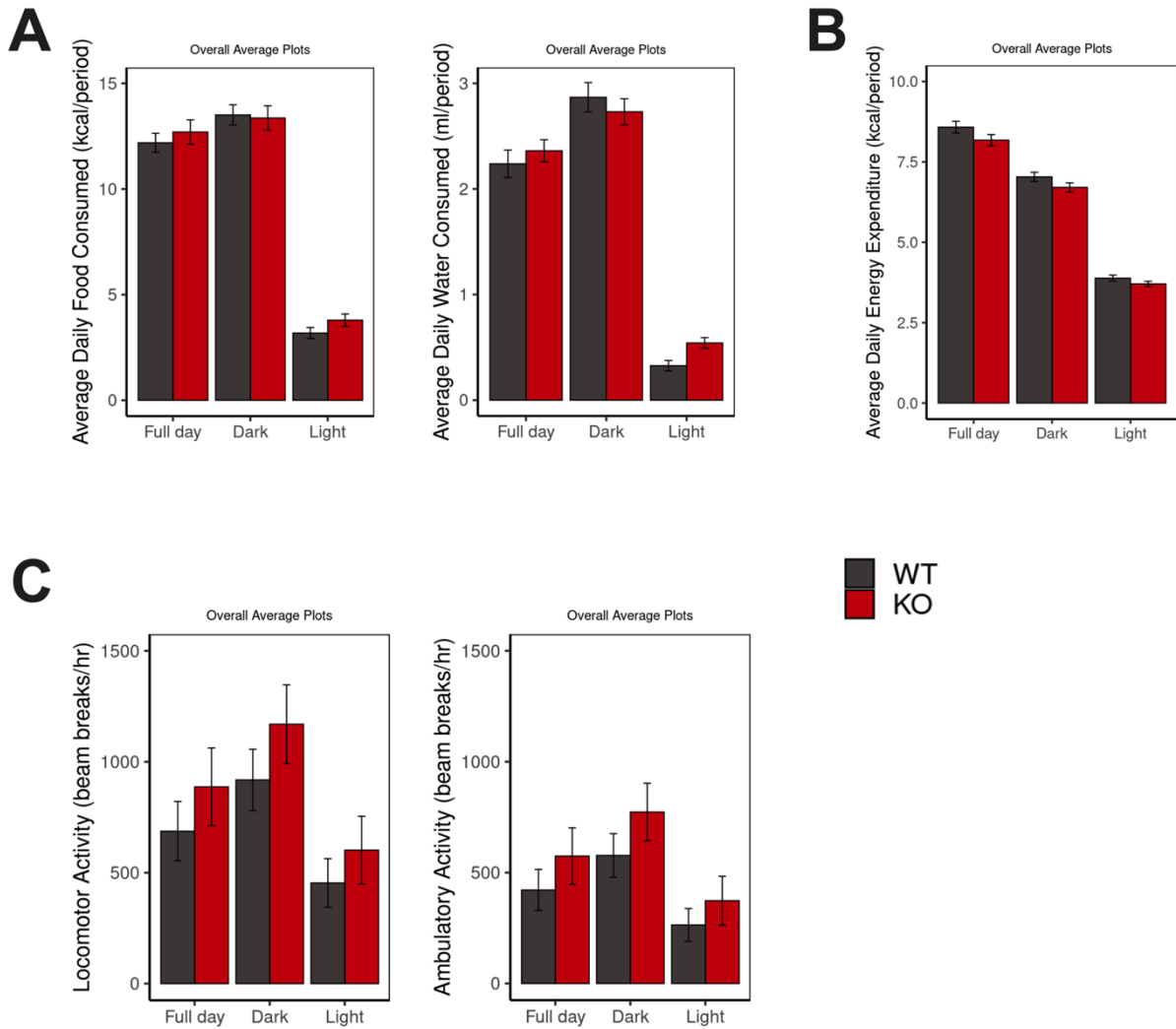
Figure 3.16 Indirect calorimetry analysis of WT and A5019G mice at 42 to 60 weeks. A. Average daily food and water consumption. **B.** Average daily energy expenditure. **C.** Locomotor and ambulatory activities. Measurements recorded on a cycle of dark (6:30 PM to 6:29 AM) and light (6:30 AM to 6:29 PM). n=12 per group. Error bars ± SEM. ANOVA.
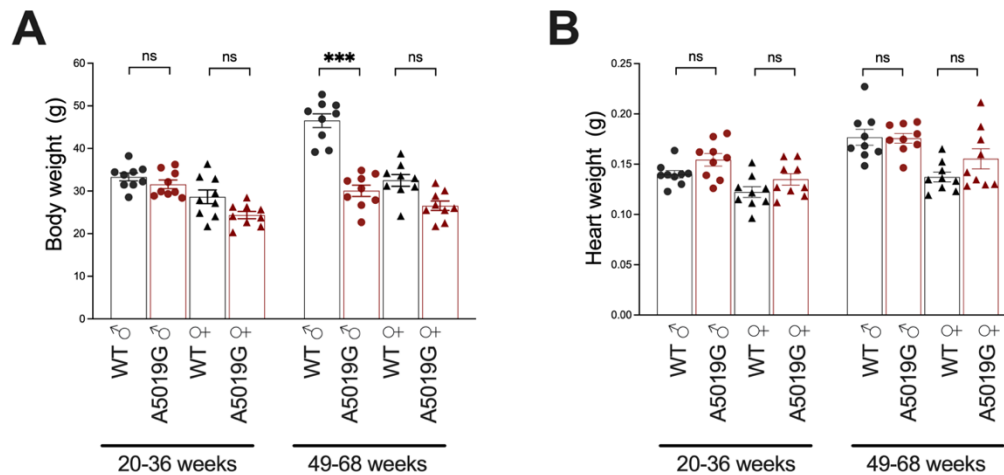
Figure 3.17 Physiological changes in A5019G mice. A. Body weight of male and female WT and A5019G mice at 20-36 weeks and 49-68 weeks. **B.** Heart weight of male and female WT and A5019G mice at 20-36 weeks and 49-68 weeks. n=9 per gender per genotype. Error bars ± SEM. Mann-Whitney U Test; *** $p < 0.0001$, ns not significant.

Based on the results of the phenotyping, m.5019A>G did not lead to alterations in energy expenditure. We did not see a change in metabolic rate in the A5019G mice. High locomotor activity was observed in older mice, but the energy expenditure was not affected. Male A5019G mice developed a lean phenotype as they grew older. On the other hand, there was no evidence of the characteristic heart enlargement associated with cardiomyopathy as seen in the C5024T mice (Filograna et al., 2019; Kauppila et al., 2016).

3.2.2. Heteroplasmy levels in different tissues

Different tissues consisting of heart, lung, liver, skeletal muscle, kidney, small intestine, and colon were collected from A5019G mice at 29 to 37 weeks and m.5019A>G mutation levels were measured by pyrosequencing (Figure 3.18A; Supplementary Table 3). Data showed that mutation levels across these tissues were consistent with the levels measured from ear clip samples of the same mice at the weaning age of 3 weeks. To compare the difference in mutation levels among tissue types, mutation level in ear clip at weaning age was then subtracted from mutation levels of different tissues (Figure 3.18B; Supplementary Table 4). Heart and skeletal muscle, which are post-mitotic tissues, consisted of lower levels of mutation as compared to highly proliferating tissue, small intestine, and colon. In A5019G mice, even with ageing, high mutation levels were consistent in highly proliferating tissues. This observation is in contrast with the observation in tALA mice carrying m.5024C>T mutation, wherein high mutation levels were selected against highly proliferative tissues.

COX/SDH histochemical staining was then performed in large intestine, in which colonic crypts were isolated using laser capture microdissection. COX-deficient (COX-) crypts and crypts with normal COX activity (COX+) were collected and m.5019A>G mutation levels were measured using pyrosequencing (Figure 3.18C; Supplementary Table 5). COX- crypts have significantly high mutation levels (mean=83.25%) as compared to COX+ crypts (mean=55.42%). This shows that the mutation segregates with mitochondrial deficiency, as measured by complex IV activity.
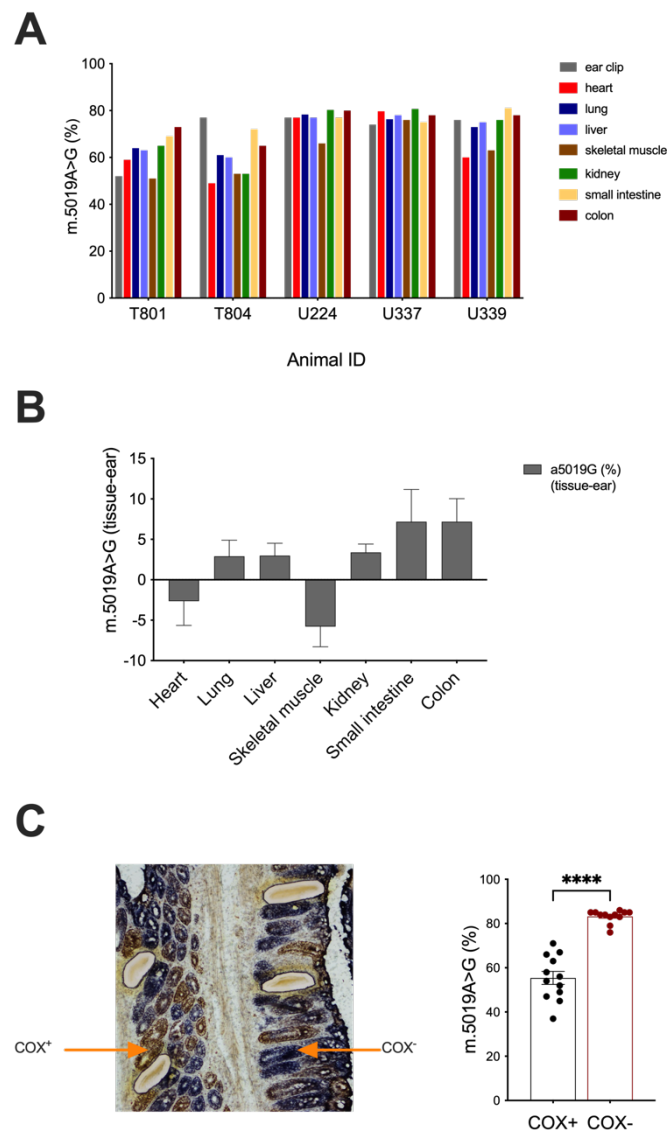
Figure 3.18 Heteroplasmy levels in different tissues of A5019G mice. A. m.5019A>G mutation levels in various tissues at 29 to 37 weeks. **B.** Heteroplasmy levels between tissues. Small intestine and colon with higher heteroplasmy levels; heart and skeletal muscle with lower heteroplasmy levels. **C.** Mutation levels in isolated colonic crypts with normal COX activity (COX+) and with COX deficiency (COX-).

3.2.3. Different tissues are affected by mitochondrial dysfunction

To investigate the occurrence of mitochondrial dysfunction, the activity of respiratory enzymes was analyzed in tissues of WT and A5019G animals with increasing mutation levels, at 29 to 37 weeks. Tissues from heart, kidney, liver, small intestine, colon, lung, and skeletal muscle (specifically gastrocnemius and soleus), and brain were cut into 10 μm sections and stained using the histochemical staining assay referred to as nitrotetrazolium blue exclusion (NBTx) assay (Simard et al., 2018). This assay uses the intermediate electron carrier phenazine methosulphate (PMS). If the mitochondrial activity is normal, PMS is reduced in Complex II and, afterward, re-oxidized by Complex IV (Figure 3.19A). This will then maintain the oxidized form of nitrotetrazolium blue chloride (NBT), rendering the tissue to be colorless. If Complex IV activity is impaired, PMS transfers electrons from Complex II to NBT resulting in the reduction of NBT and the formation of blue formazan crystals in COX-deficient mitochondria visualized by the blue staining in cells (Figure 3.19B). The intensity of the blue staining also indicates the level of COX deficiency – the darker the blue stain, the higher the level of COX deficiency. Image analysis was then performed to quantify COX deficiency. Ranges of blue optical densities were assigned to represent low (101-150), mid (151-200), and high (201-255) levels of COX deficiency.
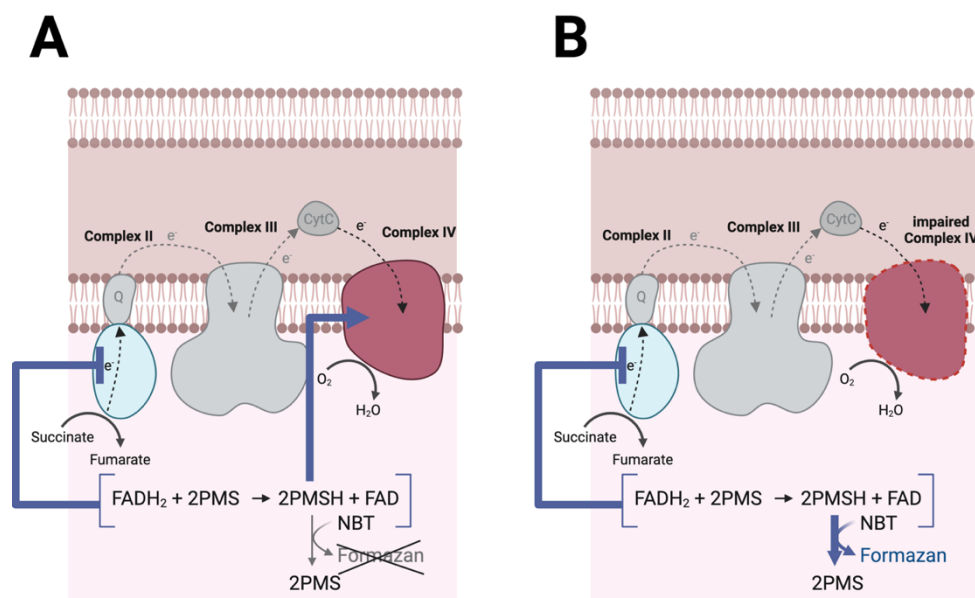
Figure 3.19 NBTx assay for visualization of COX deficiency. A. In cells with normal COX activity, PMS is reduced in Complex II and re-oxidized by Complex IV. NBT is left in its colorless, oxidized form. **B.** In cells with impaired COX activity, PMS is transporting electrons to NBT, causing blue formazan crystals to develop, thereby, the blue staining in the cells. Adapted from Simard et al., 2018. Created with BioRender.com.

In the heart tissue, normal COX activity was observed in WT mice. For low-level m.5019A>G mutation, at 59% and 63%, COX-deficient cells were sparsely occurring (Figure 3.20A). For high-level m.5019A>G mutation, at 72%, 75%, and 76%, blue stained cells, which correspond to COX-deficient cells, were occurring in higher density and at higher intensity of the blue color which can also be associated with high level of COX deficiency (Figure 3.20A). Quantifying the blue staining revealed that as the mutation level increased, percentage of blue staining was also increased, as well as the intensity of the blue color, (Figure 3.20B; Supplementary Table 6).

Normal COX activity was observed in WT, as well as in low-level mutants (at 53% and 65%) of the kidney tissue. COX-deficient cells were detected at 76% m.5019A>G. At 80% and 81%, higher blue pigment density was occurring (Figure 3.21A). The same as in the heart tissue, quantification of the blue staining in the kidney tissue showed that mitochondrial dysfunction was occurring at high-level mutants (Figure 3.21B; Supplementary Table 7).

In liver tissue, the absence of blue staining was observed in WT and also in low-level mutants (at 60% and 63%) indicating normal COX activity. With high-level mutants (at 75% and 77%), COX-deficient cells were occurring at high density (Figure 3.22A and 3.22B; Supplementary Table 8). Results in the heart, kidney, and liver tissues suggested that the threshold for the occurrence of mitochondrial dysfunction in these tissues was approximately 75%.

For small intestinal and colonic tissues, COX-deficient cells were occurring in both low-level mutants (at 69% in small intestine, at 65% in colon) and high-level mutants (≥72% in both) (Figures 3.23A–B and 3.24A–B; Supplementary Tables 9 and 10). In these tissues, the threshold was at approximately 65%. It was also observed that the blue stained cells were concentrated in the epithelial tissue lining the small intestine and colon, which has a high rate of cell turnover.

In the skeletal muscle (specifically the gastrocnemius and soleus) and in the lung tissue, blue-stained cells were sparsely occurring even in high-level mutants (≥72%) suggesting the rare occurrence of COX deficiency (Figures 3.25 and 3.26). Images were no longer placed for quantification analysis due to the very sparse blue staining. In contrast to previous research wherein skeletal muscles are primarily affected by mitochondrial dysfunction (Diaz et al., 2005), the skeletal muscle of A5019G mice exhibited a rare

occurrence of COX deficiency. It's possible that the m.5019A>G mutation affects the proliferating tissues more than the post-mitotic tissues.
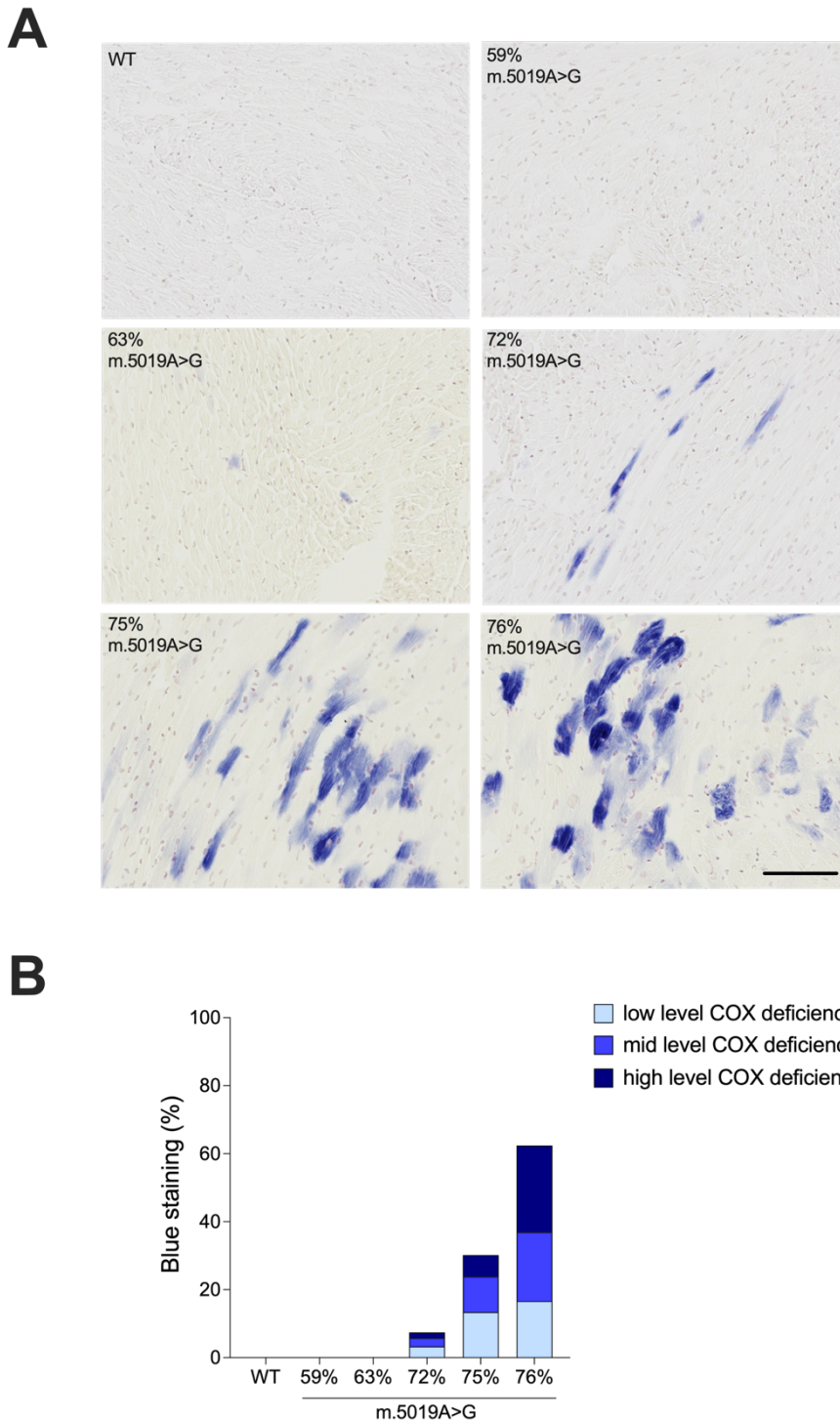
Figure 3.20 COX deficiency in heart tissue. A. Heart tissue sections of WT and A5019G mice with increasing m.5019A>G mutation levels stained using NBTx assay. Normal COX activity (indicated by the colorless state) in WT mice. COX deficiency (indicated by blue stain) in ≥72% m.5019A>G mutation levels. Scale bar represents 100 μm. **B.** Quantification of COX deficiency in heart tissue.
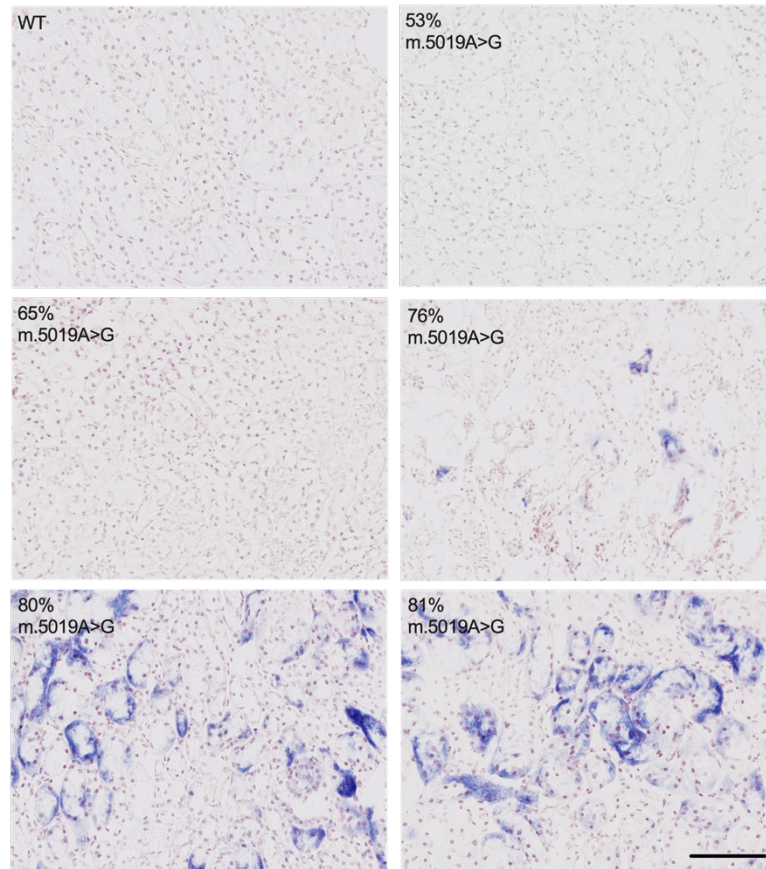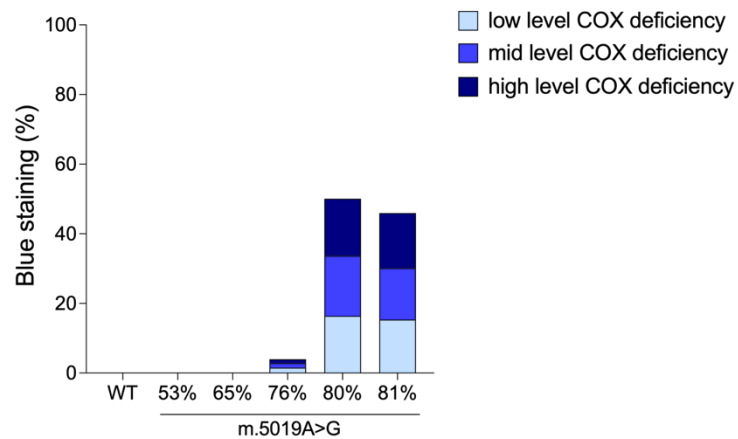
Figure 3.21 COX deficiency in kidney tissue. A. Kidney tissue sections of WT and A5019G mice with increasing m.5019A>G mutation levels levels stained using NBTx assay. Normal COX activity (indicated by the colorless state) in WT mice. COX deficiency (indicated by blue stain) in ≥76% m.5019A>G mutation levels. Scale bar represents 100 μm. **B.** Quantification of COX deficiency in kidney tissue.
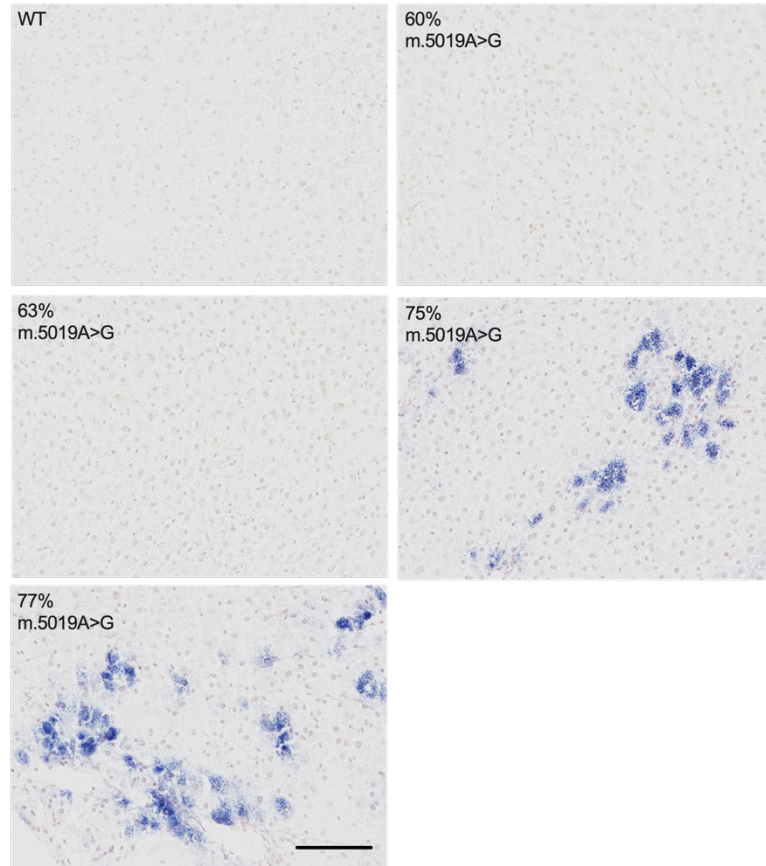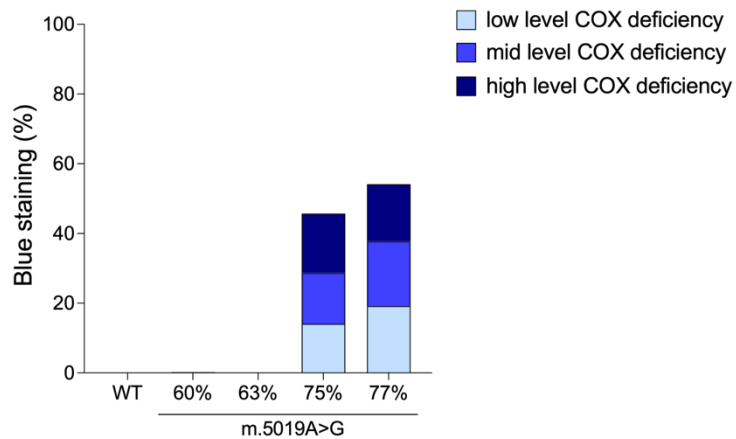
Figure 3.22 COX deficiency in liver tissue. A. Liver tissue sections of WT and A5019G mice with increasing m.5019A>G mutation levels stained using NBTx assay. Normal COX activity (indicated by the colorless state) in WT mice. COX deficiency (indicated by blue stain) in ≥75% m.5019A>G mutation levels. Scale bar represents 100 μm. **B.** Quantification of COX deficiency in liver tissue.
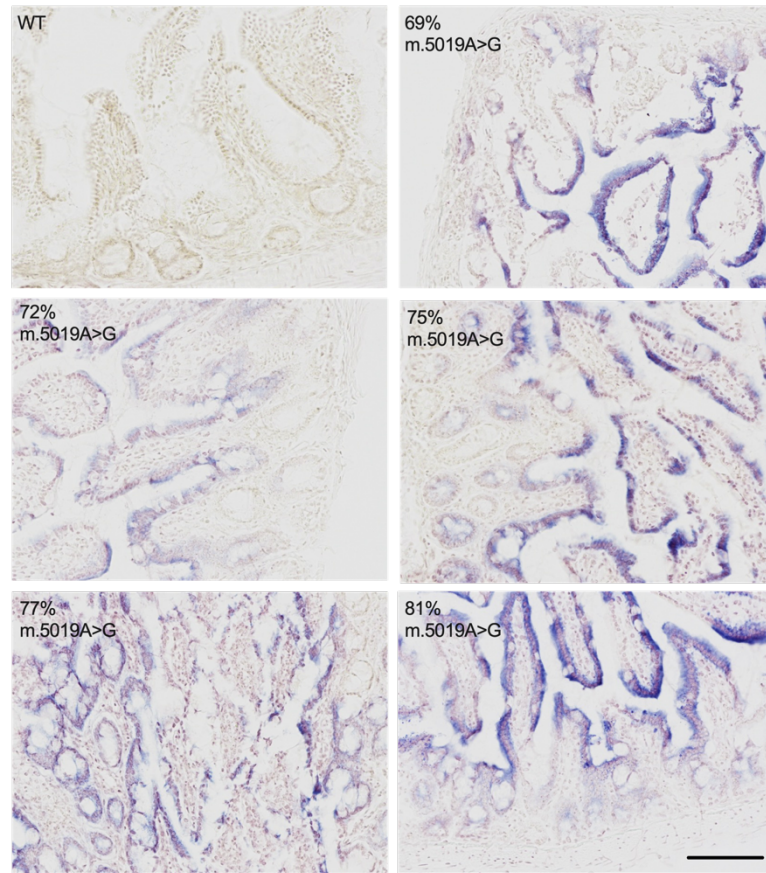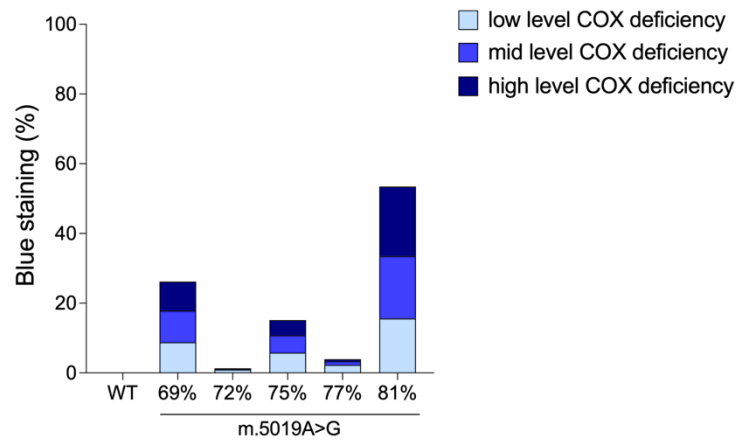
Figure 3.23 COX deficiency in small intestinal tissue A. Small intestinal tissue sections of WT and A5019G mice with increasing m.5019A>G mutation levels stained using NBTx assay. Normal COX activity (indicated by the colorless state) in WT mice. COX deficiency (indicated by blue stain) in ≥69% m.5019A>G mutation levels. Scale bar represents 100 μm. **B.** Quantification of COX deficiency in small intestinal tissue.
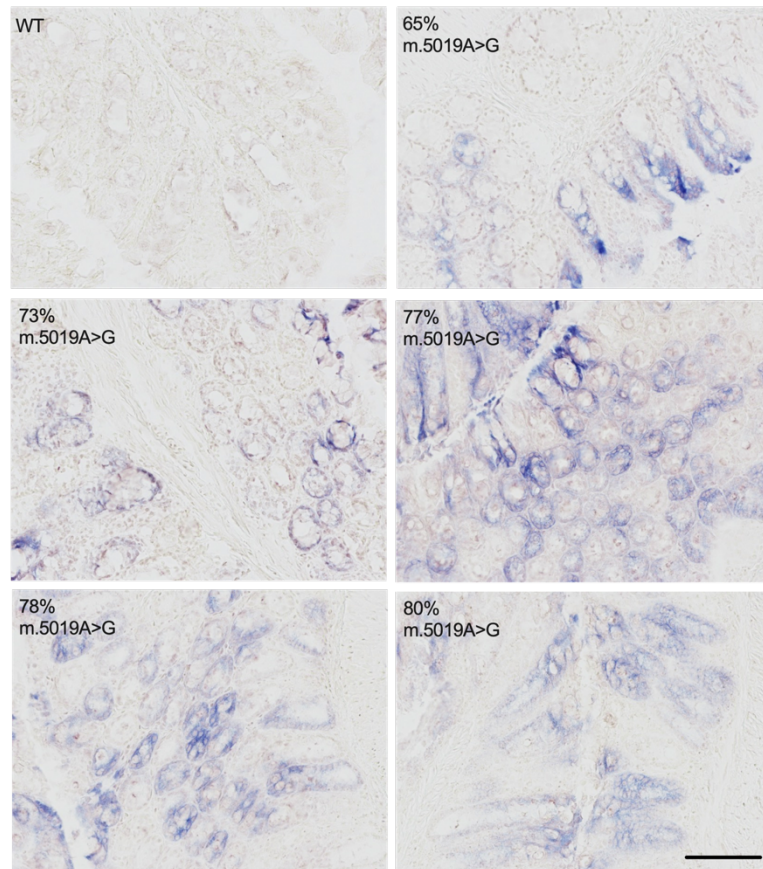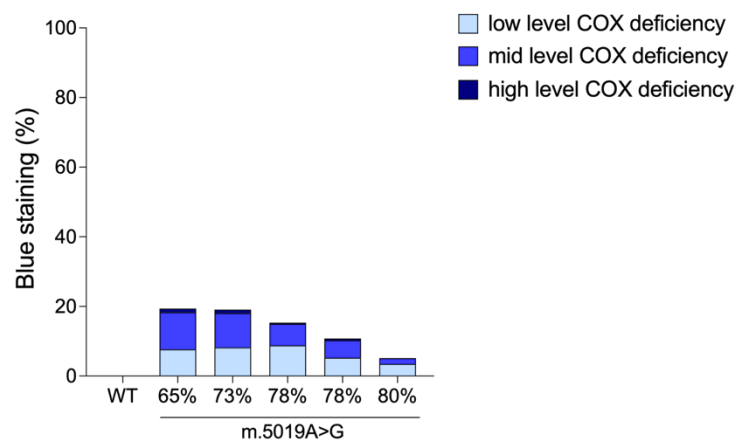
Figure 3.24 COX deficiency in colonic tissue. A. Colonic tissue sections of WT and A5019G mice with increasing m.5019A>G mutation levels levels stained using NBTx assay. Normal COX activity (indicated by the colorless state) in WT mice. COX deficiency (indicated by blue stain) in ≥65% m.5019A>G mutation levels. Scale bar represents 100 μm. **B.** Quantification of COX deficiency in large intestinal tissue.
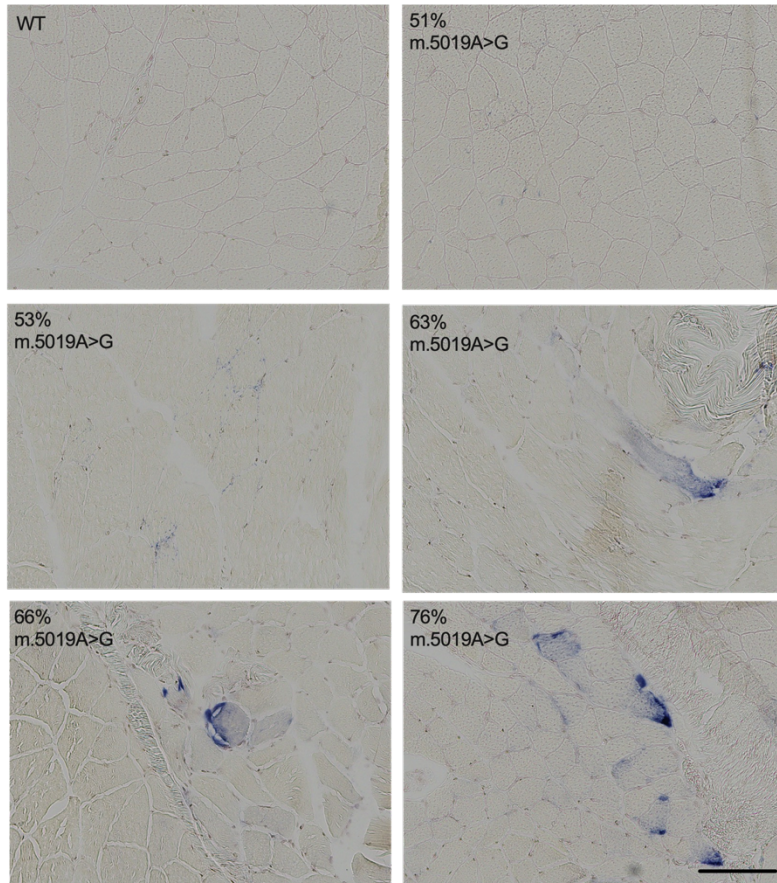
Figure 3.25 Rare occurrence COX deficiency in skeletal muscle. Gastrocnemius and soleus tissue sections of WT and A5019G mice with increasing m.5019A>G mutation levels stained using NBTx assay. Normal COX activity (indicated by the colorless state) in WT mice. Rare COX deficiency (indicated by the sparse blue stain) in ≥63% m.5019A>G mutation levels. Scale bar represents 100 μm.
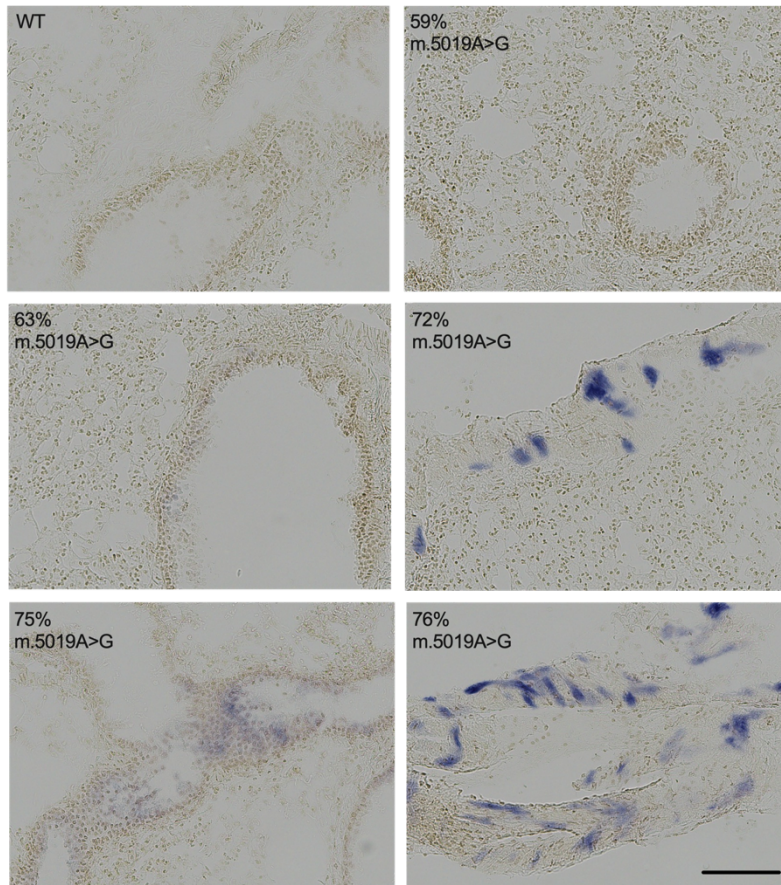
Figure 3.26 Rare occurrence COX deficiency in lung tissue. Lung tissue sections of WT and A5019G mice with increasing m.5019A>G mutation levels stained using NBTx assay. Normal COX activity (indicated by the colorless state) in WT mice. Rare COX deficiency (indicated by the sparse blue stain) in ≥72% m.5019A>G mutation levels. Scale bar represents 100 μm.

In the brain, COX-deficient cells were observed in specific regions – the choroid plexus and the hippocampus – of 100-week-old mice with 80% m.5019A>G mutation level (Figure 3.27). The choroid plexus consists of epithelial cells surrounding a core of capillaries and connective tissue (Lun et al., 2015). It functions in the production of cerebrospinal fluid (CSF) through excretion and secretion mechanisms (Lun et al., 2015; Wolburg & Paulus, 2010). High mitochondrial content, 12-15% of the cell cytoplasm, was present in the epithelium of the choroid plexus of primates and was associated with the secretory activities and maintenance of ionic gradients across blood-CSF barriers (Cornford et al., 1997). Choroid epithelial cells,

which are non-neuronal cells, are therefore heavily dependent on oxidative metabolism. In aging mice, accumulation of COX-deficient cells was observed in both the choroid plexus epithelial cells and in the CA (cornu ammonis) pyramidal neurons of the hippocampus (Cottrell et al., 2001). Transmembrane ionic gradient maintenance in neuronal cells also depends on ATP synthesis through OXPHOS (Cottrell et al., 2001). Hippocampal neurons play a vital role in learning and memory formation. Mitochondrial dysfunction in the hippocampus has been observed in aging mice contributing to memory loss (Olesen et al., 2020).
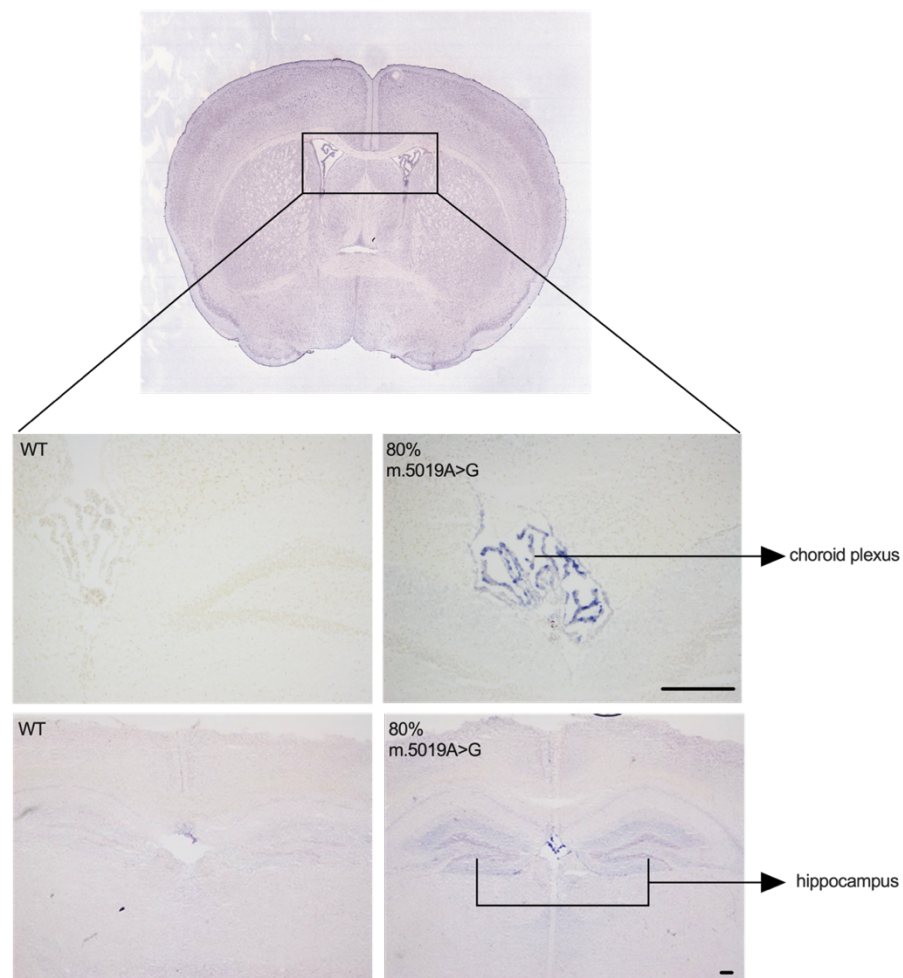
Figure 3.27 COX deficiency in brain tissue. Normal COX activity (as shown by colorless cells) in the brain of WT mice at 100 weeks while age-matched mice with 80% m.5019A>G heteroplasmy level display COX deficiency (blue stained cells) in the choroid plexus and hippocampus. Scale bar represents 100 μm. Data by Simard and Charl.

3.2.4. NDUF8 and MTCO1 protein steady-state levels are reduced in the small intestinal epithelial tissue but not in the heart

To measure the steady-state levels of specific proteins involved in OXPHOS, total protein was isolated from the small intestinal epithelial tissue and heart tissue of WT and A5019G mice. Western blotting was performed using the Total OXPHOS Rodent WB Antibody Cocktail (ab110413) with Beta-Actin as the loading control. Western blot analyses of the small intestinal epithelial tissue in both 20- to 25-week-old and 50- to 59-week-old mice showed that there is a significant reduction in NDUFB8, which is a nuclear-encoded subunit of Complex I, and MTCO1, a mitochondrially encoded subunit of Complex IV (Figure 3.28A–D). UQCRC2, a mitochondrially encoded subunit of Complex III, likewise showed a reproducible decrease, although quantification did not show a statistically significant difference (Figure 3.28A-D).
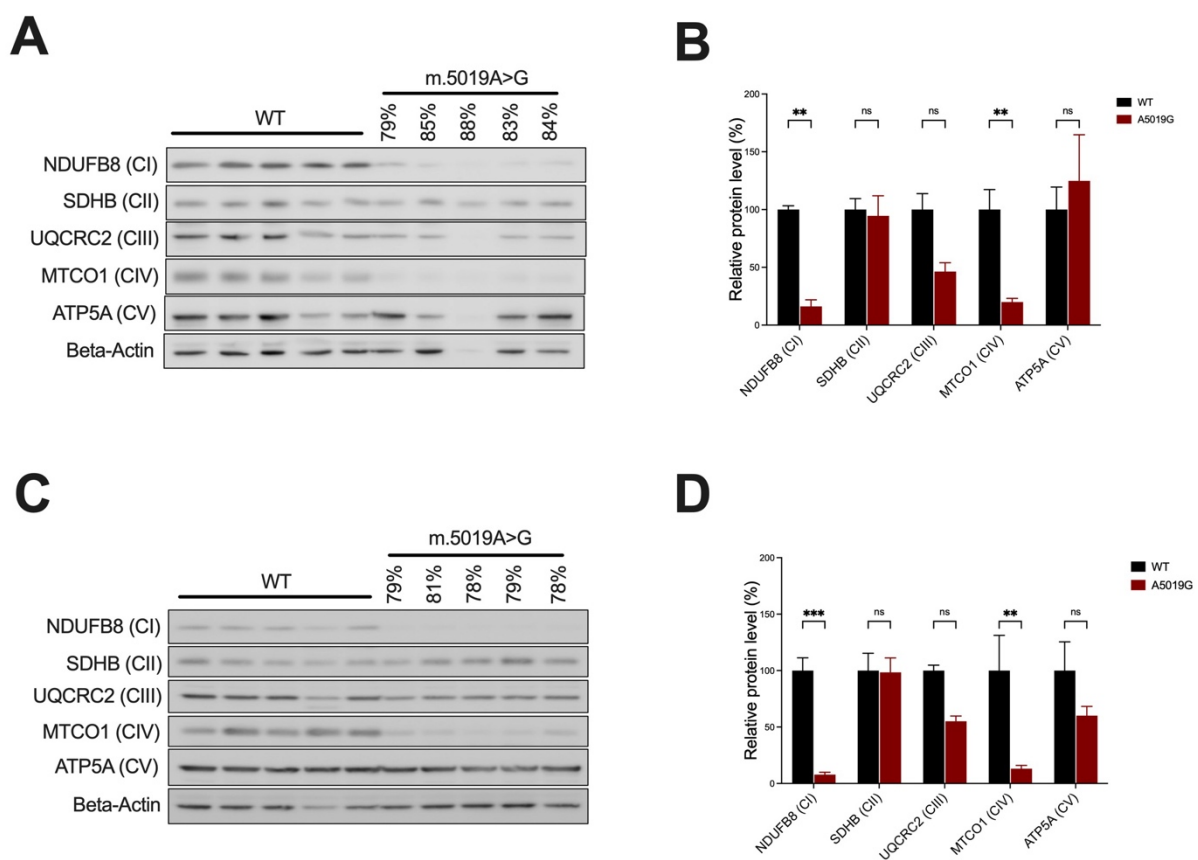
Figure 3.28 Reduced steady-state levels of specific OXPHOS protein subunits in the intestinal epithelial tissue. A. Western blot analysis of specific OXPHOS protein levels in small intestinal tissue of WT and high-level m.5019A>G mutation mice at 20 to 25 weeks. Loading control: Beta-Actin. **B.** Quantification of Western blotting in A. Values normalized to Beta-Actin. Error bars ± SEM. Two-way ANOVA; ** p<0.01, ns not significant. **C.** Western blot analysis and quantification of specific OXPHOS protein levels in small intestinal tissue of WT and high-level m.5019A>G mutation mice at 50 to 59 weeks. Loading control: Beta-Actin. **D.** Quantification of Western blotting in C. Values normalized to Beta-Actin. Error bars ± SEM. Two-way ANOVA; ** p<0.01, *** p<0.001, ns not significant.

In the heart tissue, however, no significant difference in the level of expression of specific OXPHOS protein subunits was observed between WT and A5019G mice (Figure

3.29A-B). The heart is a post-mitotic tissue with relatively slow mitochondrial turnover and biogenesis. One possible reason that the result in the heart tissue is different from the intestinal epithelial tissue is that based on the NBTx histochemical staining, the heart tissue showed a mosaic distribution of COX deficiency while COX deficiency is concentrated in the intestinal epithelial tissue. In the heart, normal and COX-deficient cells were mixed while the small intestinal epithelium were mainly composed of COX-deficient cells.
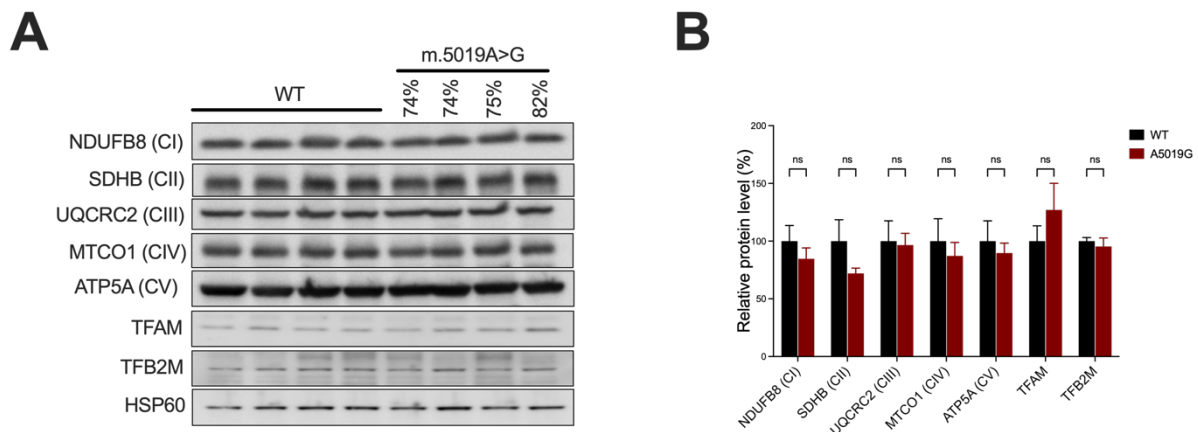
Figure 3.29 Stable steady-state levels of specific OXPHOS proteins in the heart tissue. A. Western blot analysis of specific OXPHOS protein levels in the heart tissue of WT and high-level m.5019A>G mutation mice at 29 to 36 weeks. Loading control: HSP60. **B.** Quantification of Western blotting in A. Values normalized to HSP60. Error bars ± SEM. Two-way ANOVA; ns not significant.

3.2.5. Protein subunits of respiratory Complex I and Complex IV are reduced in the intestinal epithelial tissue

Proteomics was performed in small intestinal epithelial tissue of WT and A5019G mice with ≥83% m.5019A>G mutation levels at 22-26 weeks and ≥81% m.5019A>G mutation levels at 58-66 weeks. A total of 7,691 proteins were quantified in the 22–26-week-old mice, of which 109 proteins showed a significant decreased in expression and 69 showed a significant increased (up) (Figure 3.30A). In 58–66-week-old mice, 7,621 proteins were quantified, 1,071 were decreased/down and 1,022 were increased/up (Figure 3.30B). Compared to 22–26-week-old mice, an almost 12-fold increase in the number of significantly changed proteins was observed in 58–66-week-old mice indicating that extensive changes occur in the intestinal epithelium proteome of A5019G mice as they aged. We also determined the number of mitochondrial proteins annotated based on Mito Carta 3.0, 11.1% of which were mitochondrial proteins in the 22–26-week-old mice and 10.8% in the 58–66-week-old mice (Figure 3.30C

and 3.30D, respectively). The log fold change (FC) values of mitochondrial proteins are listed in Supplementary Table 11.

Analyses of mitochondrial proteins revealed that in A5019G mice, expression of the majority of the respiratory complex protein subunits of Complex I and Complex IV were significantly reduced in both age groups (Figure 3.31A). Some of the protein subunits of Complex III were also reduced but the reduction was not as strong as those in Complexes I and IV (Figure 3.31A). The reduction in Complexes I and IV subunits is also consistent with western blot results of specific OXPHOS subunits (Figure 3.28). This is consistent with the mitochondria-specific translational defect (Murgia et al., 2019). Complex II, containing only nucleus-encoded subunits, was unaffected. Assembly factors of the OXPHOS complexes, on the other hand, were increased (Figure 3.31B), suggesting that it is likely a compensatory response for the reduced respiratory complex subunits. Proteins involved in mtDNA maintenance were either unchanged or increased (Figure 3.32A). Proteins involved in mtRNA metabolism were not affected in 22–26-week-old mice but were increased in 58–66-week-old (Figure 3.32B). Proteins for mitochondrial translation were increased significantly in the 58–66-week-old mice (Figure 3.33).

Overall, these results revealed that m.5019A>G mutation is primarily affecting the small intestinal epithelium, a highly proliferating tissue, characterized by proteomic changes consisting of reduced expression of Complex I and IV subunits, and a compensatory upregulation of proteins for OXPHOS assembly, mtRNA metabolism, and mitochondrial translation.
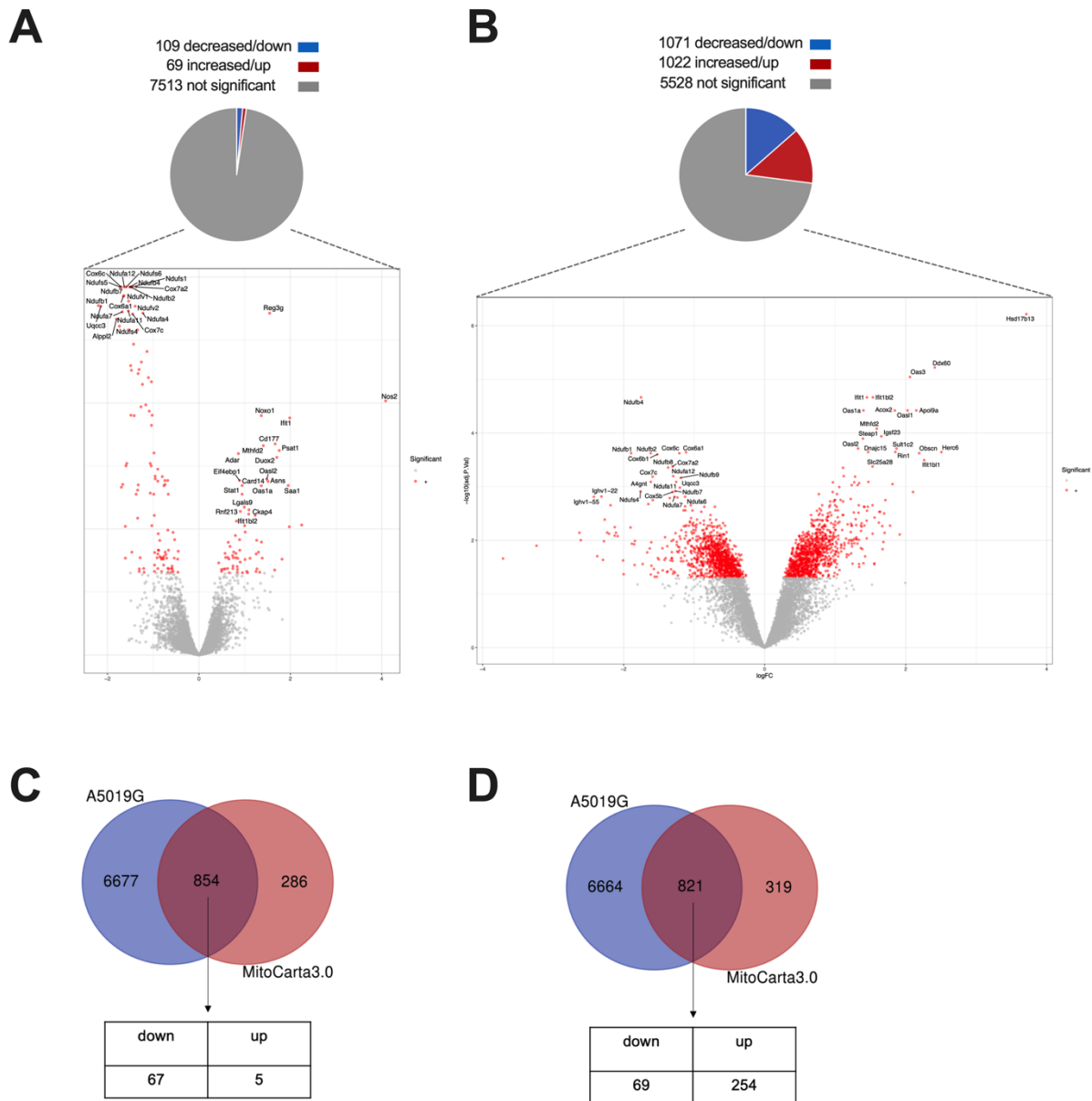
Figure 3.30 Identification of significantly changed proteins in A5019G mice. A. Volcano plot of significantly changed proteins in small intestinal epithelial tissue of A5019G mice at 22 to 26 weeks, n=5 per group, significance cut-off at p<0.05. **B.** Volcano plot of significantly changed proteins in small intestinal epithelial tissue of A5019G mice at 58 to 66 weeks**,** n=8 per group, significance cut-off at p<0.05. **C.** Venn diagram showing 854 annotated mitochondrial proteins identified in A5019G mice at 22 to 26 weeks. **D.** Venn diagram of the 821 annotated mitochondrial proteins in A5019G mice at 58 to 66 weeks.
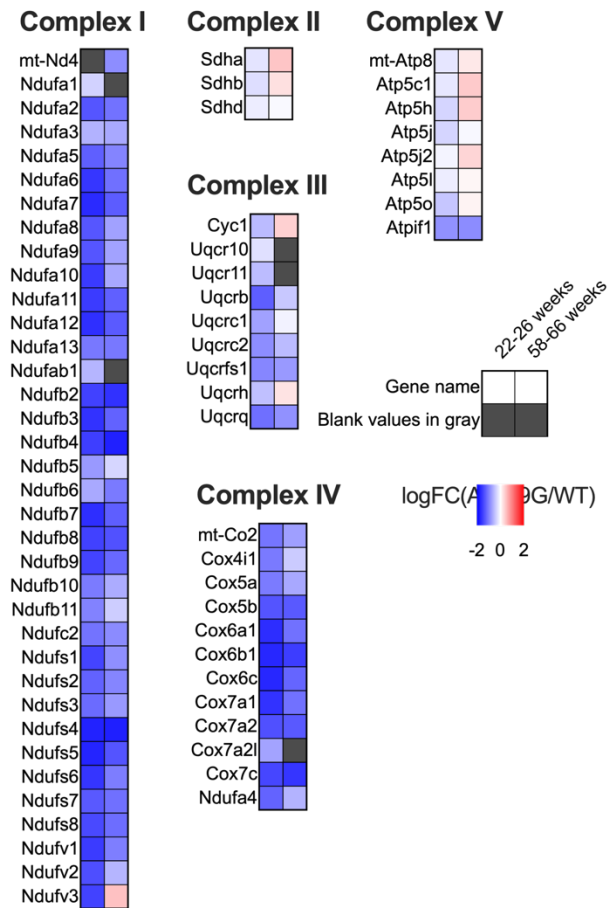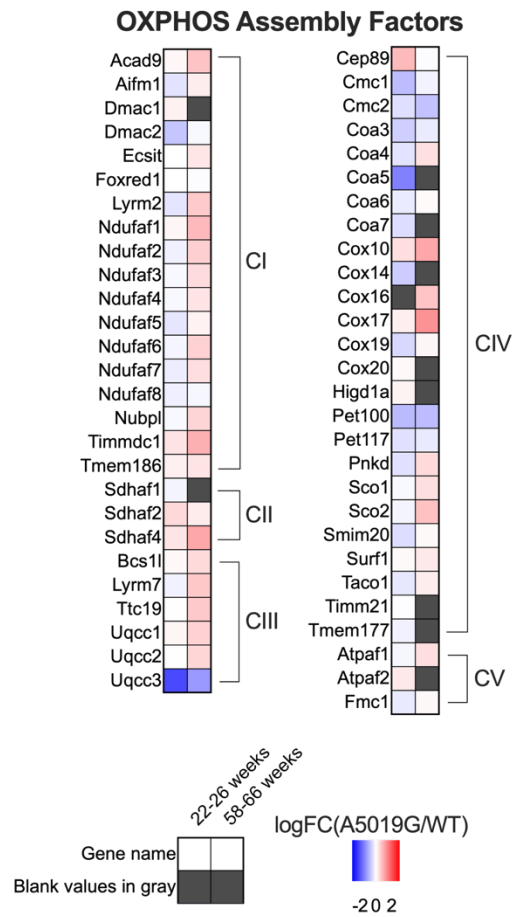
Figure 3.31 Reduced expression of subunits of respiratory chain complexes and increased expression of assembly factors. A. Heatmaps illustrating log fold-change in OXPHOS protein subunits in the intestinal epithelial tissue of A5019G mice at 22 to 26 weeks (first column) and at 58 to 66 weeks (second column). **B.** Heatmaps illustrating log fold-change in OXPHOS assembly factors in the intestinal epithelial tissue of A5019G mice at 22 to 26 weeks (first column) and at 58 to 66 weeks (second column).
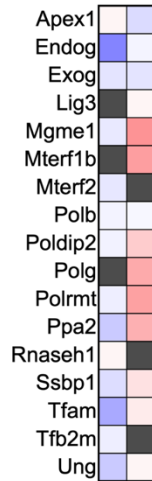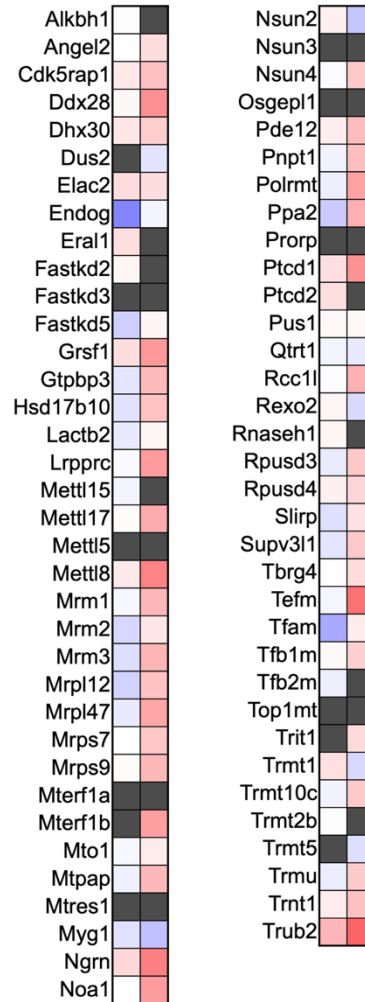
Figure 3.32 Expression of proteins involved in mtDNA maintenance and mtRNA metabolism. A. Heatmap illustrating log fold-change in mtDNA maintenance proteins in the intestinal epithelial tissue of A5019G mice at 22 to 26 weeks (first column) and at 58 to 66 weeks (second column). **B.** Heatmaps illustrating log fold-change in proteins for mtRNA metabolism in the intestinal epithelial tissue of A5019G mice at 22 to 26 weeks (first column) and at 58 to 66 weeks (second column).
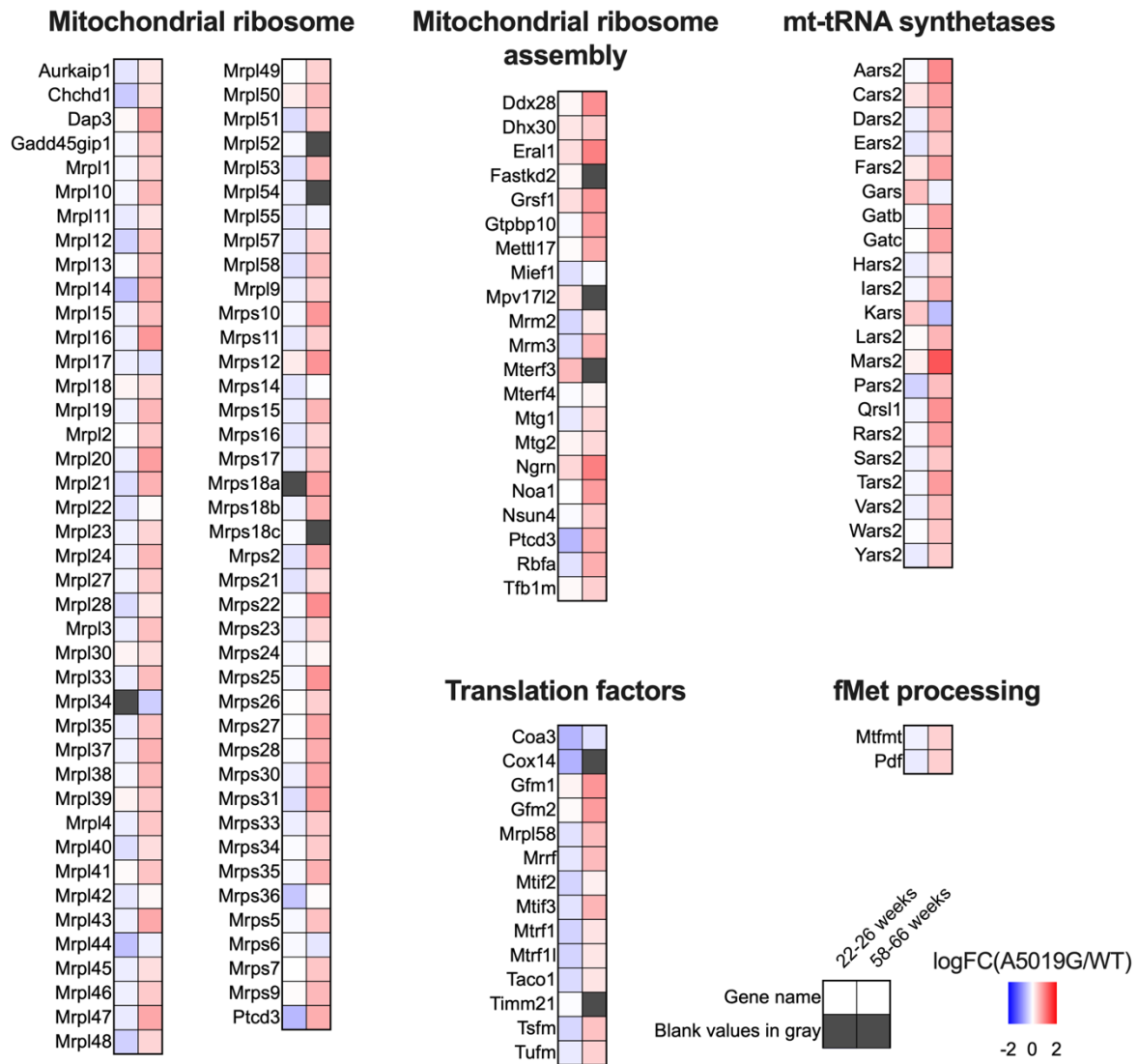
Figure 3.33 Increased expression of proteins involved in mitochondrial translation. Heatmaps illustrating log fold-change in proteins for mitochondrial ribosome and assembly factors, translation factors, mt-tRNA synthetases, and fMet processing in the intestinal epithelial tissue of A5019G mice at 22 to 26 weeks (first column) and at 58 to 66 weeks (second column).

3.2.6. Enriched biological pathways in A5019G mice

To further investigate the proteomic changes in A5019G mice, enriched biological processes were identified from the proteomics data of small intestinal epithelial tissue using Ingenuity Pathway Analysis (IPA) software (Qiagen). The most statistically significant canonical pathways are shown in Figure 3.34 together with their respective scores. The IPA z-score predicts the activation or inhibition of the specific signaling pathway. Of the perturbed pathways, mitochondrial dysfunction was on top. It also predicted that oxidative phosphorylation was strongly inhibited. Another predicted inhibited pathway included tRNA

charging. These results are consistent with the findings of the other experiments, such as in the histochemical staining and aminoacylation test. On the other hand, the sirtuin signaling pathway and BAG2 (Bcl-2-associated athanogene) signaling pathway were predicted to be activated. Sirtuins have a role in cell stress responses and in regulating metabolic processes, including mitochondrial quality control (Xu et al., 2023). BAG proteins function as co-chaperone by binding to Hsc/Hsp70 and coupling it to the proteosome (Behl, 2016).
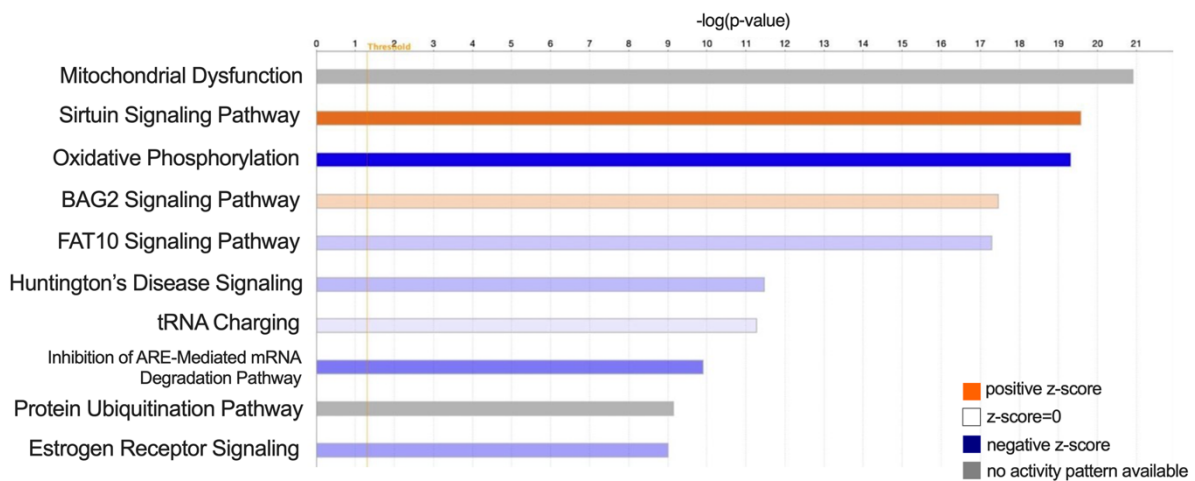
Figure 3.34 Ingenuity Pathway Analysis (IPA) of proteomic data in A5019G mice. List of top ten canonical pathways derived from IPA. The horizontal axis is the -log(p-value) and the vertical line (light orange) is the threshold for the p-value. Z-score corresponds to the prediction of activation (orange) or inhibition (blue) of specific signaling pathways.

3.3. Comparison of mt-tRNA^ALA mouse models: C5024T versus A5019G

3.3.1. Complex I and Complex IV protein subunits are more reduced in A5019G mice than in C5024T mice

After characterizing the A5019G mice, the next objective was to compare them to the previously developed C5024T mice carrying the m.5024C>T mutation that is only 5 bp apart from the m.5019A>G mutation in A5019G mice. Both mutations are located at the acceptor stem of mt-tRNA^ALA. Based on previous findings, the m.5024C>T mutation affects mt-tRNA^ALA stability (Kauppila et al., 2016) while, as shown in this study, the m.5019A>G mutation affects mt-tRNA^ALA aminoacylation. To further compare the two mouse models, proteomics was performed using the intestinal epithelial tissue of C5024T and A5019G mice at 22 to 26 weeks. 7,691 proteins were quantified, of which 70 proteins showed a significant decrease (down) in

expression and 3 proteins showed a significant increase (up) in C5024T mice (Figure 3.35A); in A5019G mice, 109 proteins were decreased/down and 69 proteins were increased/up (Figure 3.35B). Mitochondrial proteins annotated (Mito Carta 3.0) were also determined, wherein 11.1% consisted of mitochondrial proteins in both mouse models (Figure 3.35C and 3.35D). For proteins involved in OXPHOS, protein subunits in Complexes I and IV were more reduced in A5019G mice than in C5024T mice (Figure 3.36A) while levels of proteins for OXPHOS assembly factors were not significantly changed (Figure 3.36B). Supplementary Table 11 contains the log FC values of mitochondrial proteins.
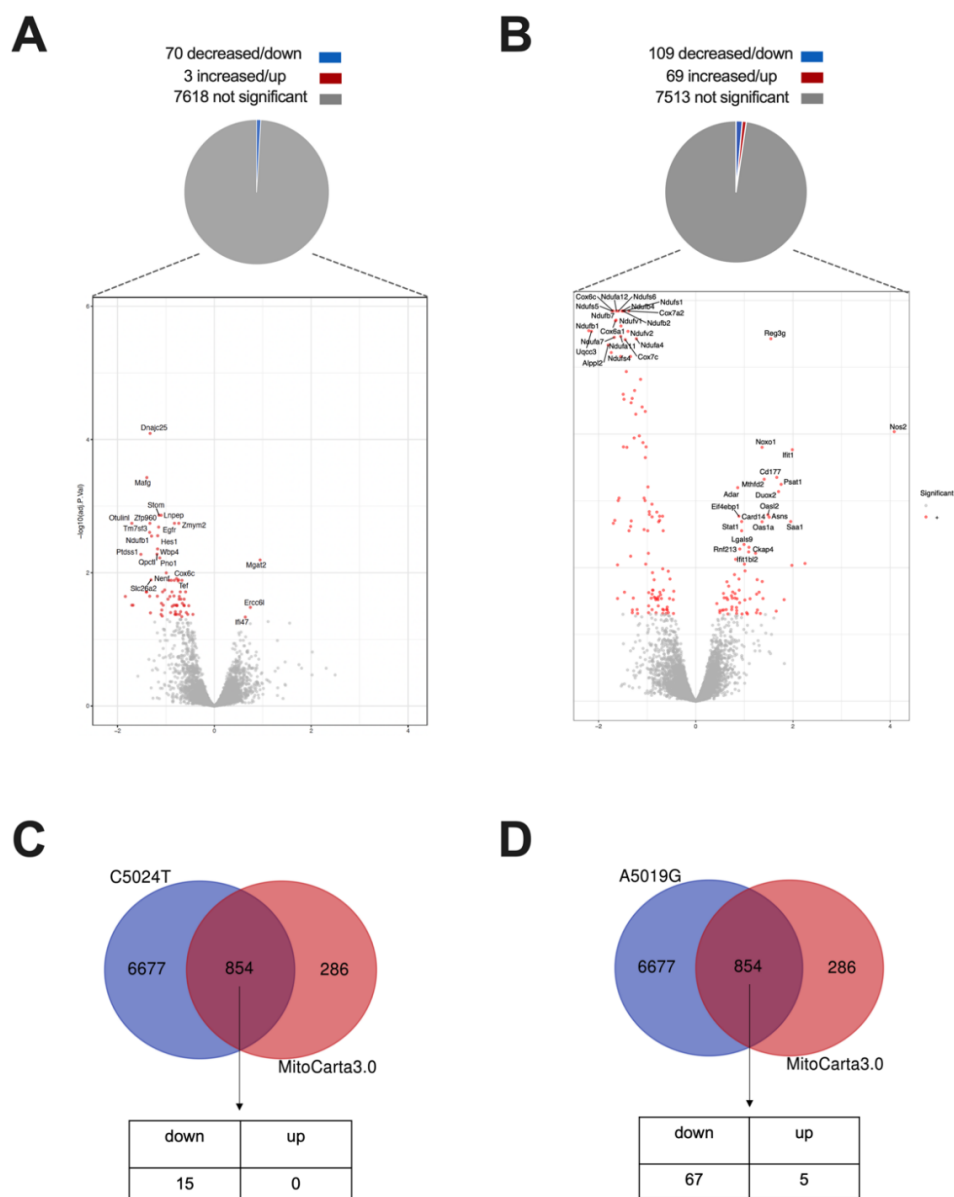
Figure 3.35 Identification of significantly changed proteins in C5024T and A5019G mice. A. Volcano plot of significantly changed proteins in small intestinal epithelial tissue of C5024T mice at 22

to 26 weeks, n=5 per group, significance cut-off at p<0.05. **B.** Volcano plot of significantly changed proteins in small intestinal epithelial tissue of age-matched A5019G mice, n=8 per group, significance cut-off at p<0.05. **C.** Venn diagram showing 854 annotated mitochondrial proteins identified in C5024T mice at 22 to 26 weeks. **D.** Venn diagram of the 854 annotated mitochondrial proteins of age-matched A5019G mice.
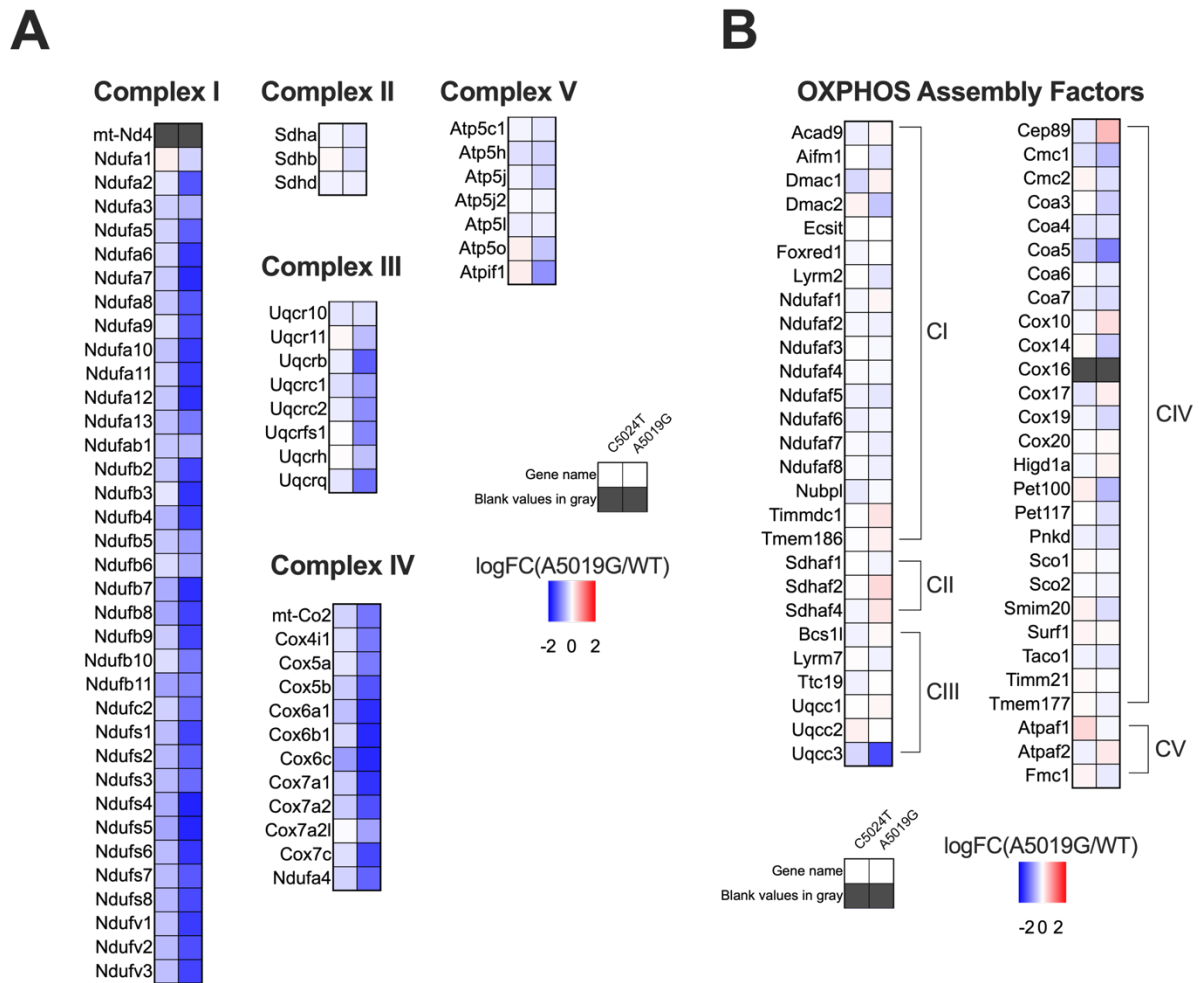
Figure 3.36 More reduced levels of subunits of respiratory chain Complex I and Complex IV in A5019G mice than in C5024T mice. A. Heatmaps illustrating log fold-change in OXPHOS protein subunits in the intestinal epithelial tissue of C5024T mice at 22 to 26 weeks (first column) and of age-matched A5019G mice (second column). **B.** Heatmaps illustrating log fold-change in OXPHOS assembly factors in the intestinal epithelial tissue of C5024t mice at 22 to 26 weeks (first column) and of age-matched A5019G mice (second column).

3.3.2. COX deficiency is occurring in different tissues in both C5024T and A5019G mice

NBTx assay was conducted in tissues of the C5024T and A5019G mice at 11 to 17 weeks. COX deficiency was observed in occasional cardiomyocytes in the C5024T mouse heart whereas the A5019G mouse heart presented a higher incidence of COX deficiency (Figure 3.37). Various tissues, including the liver, kidney, small intestine, and colon were also tested (Figure 3.38). In the liver, both mouse models showed COX-deficient hepatocytes, with C5024T mice displaying a lower incidence of COX deficiency. Conversely, compared to the A5019G mouse kidney, the kidney cells in the C5024T mice presented a higher incidence of COX deficiency. In the small intestine and colonic tissue samples, COX deficiency was detected in the intestinal epithelial cells in both mouse models. The A5019G small intestinal and colonic epithelial tissues showed a higher incidence of COX deficiency compared to the C5024T samples. Moreover, in the A5019G mouse colon, we also observed COX-deficient cells in the smooth muscle surrounding the colon. In contrast, we did not detect COX deficiency in the C5024T colonic smooth muscle until a very advanced age (Kauppila et al., 2016). In general, these results showed that both mutations affect OXPHOS through varied degrees of COX activity impairment in different tissues.
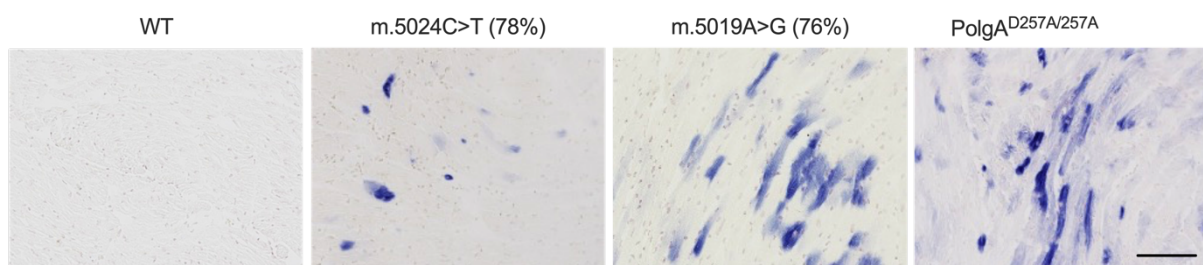
Figure 3.37 Higher incidence of COX deficiency in A5019G cardiomyocytes than in C5024T. NBTx stained heart tissue sections of WT as negative control, m.5024C>T mutation mice, m.5019A>G mutation mice, and PolgA$^{D257A/257A}$ as positive control. Normal COX activity shown by the colorless state of the cells, COX deficiency shown by blue-stained cells. Scale bar represents 100 μm.
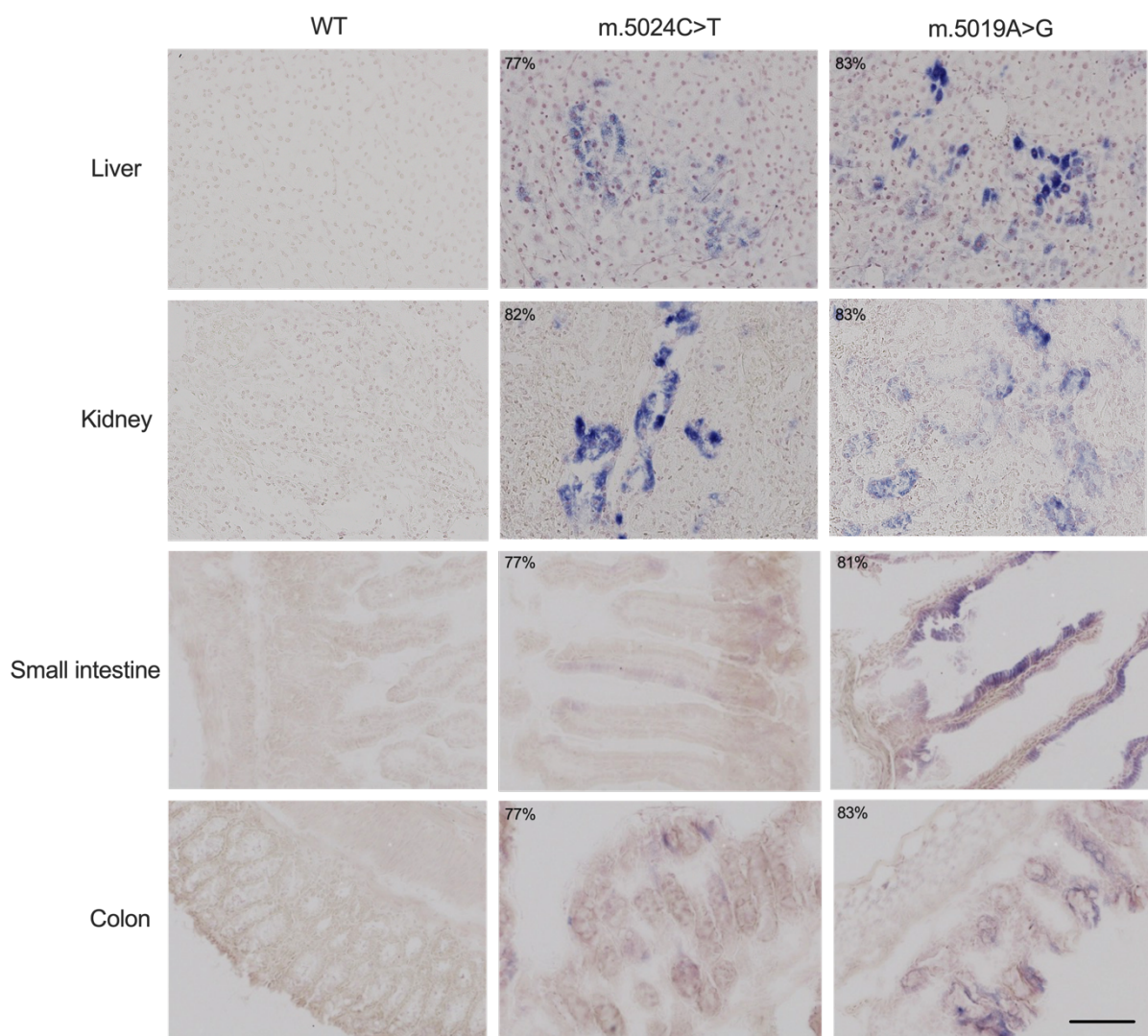
Figure 3.38 COX deficiency in various tissues of C5024T and A5019G mice. Occurrence of COX deficiency in the liver, kidney, small intestine, and colonic tissues of C5024T and A5019G mice at 11 to 17 weeks with milder COX deficiency in the small intestinal and colonic tissues of C5024T mice as compared to A5019G mice. Sections of different tissues of WT, high-level m.5024C>T mutation mice, and high-level m.5019A>G mutation mice stained using the NBTx assay. The colorless cells show normal COX activity, whereas the blue-stained cells indicate COX deficiency. Scale bar represents 100 μm.

4. DISCUSSION

The understanding of various mechanisms underlying mitochondrial dysfunction and mitochondrial diseases has progressed significantly over the years as a result of advances made in the field of mitochondrial research. However, the development of animal models with heteroplasmic mtDNA mutations recapitulating mitochondrial diseases has still been limited due to the challenges of introducing mutations in the mitochondrial genome. To address this, we have developed a mouse model carrying mtDNA mutations and investigated the molecular, biochemical, and phenotypic consequences of these mutations. We identified three linked mtDNA point mutations: the m.15200A>G mutation located in the CytB gene, the m.16232A>T mutation in the LSP region, and the m.5019A>G in the mt-tRNA^{ALA} gene. The m.15200A>G mutation is a synonymous mutation, which does not interfere with mitochondrial function. The m.16232A>T mutation caused a relatively minimal reduction in transcription initiation according to *in vitro* transcription assay results. Nevertheless, the mt-mRNA steady-state levels are not affected by this slower rate of transcription initiation, and the mtDNA copy number is not reduced. Consequently, although a contributing role cannot be ruled out, m.16232A>T mutation is not likely pathogenic. The m.5019A>G mutation located in the mt-tRNA^{ALA} does not alter mt-tRNA^{ALA} stability in both the heart (a post-mitotic tissue), and the small intestinal epithelium (a highly proliferating tissue). Instead, it affects the aminoacylation of mt-tRNA^{ALA}, as revealed in the aminoacylation assay using MEFs, the heart, and in the intestinal epithelium (Burr et al., 2023). It seemed to more profoundly affect the rapidly proliferating intestinal epithelial tissue, which exhibits proteomic changes, such as decreased expression of Complex I and IV subunits and compensatory upregulation of OXPHOS assembly, mtRNA metabolism, and mitochondrial translation proteins. The m.5019A>G mutation is, therefore, the major pathogenic mutation causing mitochondrial dysfunction in this novel mouse model, and thus we refer to these mice as A5019G mice.

During aminoacylation or tRNA charging, specific amino acid is ligated to the adenosine in the conserved 3'-terminal CCA sequence of the tRNA by aminoacyl-tRNA synthetase (aaRS) resulting in an aaRS-tRNA complex. In relation to mt-tRNA^{ALA}, the resulting complex is then referred to as AlaRS·tRNA^{ALA}. Structural and biochemical analyses have shown that a single G3-U70 wobble base pair in the acceptor stem of mt-tRNA^{ALA} plays an important role in attaining its selectivity by promoting a conformational change recognized by AlaRS which results in its efficient aminoacylation (Naganuma et al., 2009, 2014). In this study, we found that protein expression of mitochondrial aminoacyl-tRNA synthetase Aars2 is up in

A5019G mice at 58 to 66 weeks, which is possibly a compensatory mechanism since the aminoacylation efficiency of mt-tRNA^{ALA} is affected.

Since mt-tRNAs are necessary for mitochondrial protein synthesis, strong correlations exist between mitochondrial diseases and pathogenic mt-tRNAs mutations (Suzuki et al., 2020). The pathogenic mutation identified in our mouse model, m.5019A>G mutation, is in the mt-tRNA^{ALA} gene. Based on previous reports, human patient mutations in mt-tRNA^{ALA} gene are more commonly associated with isolated myopathy, in contrast to mutations in other mt-tRNA genes that are associated with various symptoms, such as multisystemic diseases. 15 mt-tRNA^{ALA} mutations have been reported in the Mitomap database as of January 2024 in which 7 have a high chance of being pathogenic – m.5650G>A (pathogenic), m.5628T>C (likely pathogenic), m.5591G>A (possibly pathogenic) m.5595G>A (possibly pathogenic), m.5613T>C (possibly pathogenic), m.5636T>C (possibly pathogenic), and m.5652C>G (possibly pathogenic) with pathogenicity scoring based on MitoTIP (Sonney et al., 2017). One of the previously identified mt-tRNA^{ALA} mutations is the m.5650G>A mutation which was first reported in a patient with cerebral autosomal dominant arteriopathy with subcortical infarcts and leukoencephalopathy (CADASIL) and myopathy (Finnilä et al., 2001). This patient was also harboring a concomitant R133C mutation in the Notch 3 gene causing CADASIL. Although myopathy was identified, the patient's phenotype was dominated by neurological complications, such as memory loss, cognitive impairment, and ataxia, which are indicative of CADASIL. Adding more complexity is that these neurological complications are also frequently exhibited in mitochondrial diseases, thus making it challenging to assess the proportional contribution of each condition to the patient's phenotype. The m.5650G>A mutation was then reported in a family in which the daughter exhibited a pure myopathy, and the mother was eventually diagnosed with a mild mitochondrial disorder, though she had never sought treatment for her symptoms (McFarland et al., 2008). This case clearly demonstrates that the m.5650G>A mutation can result in highly variable phenotypes. In this family, the m.5650G>A mutation is heteroplasmic, with an above 95% threshold, and is located in the acceptor stem of mt-tRNA^{ALA}. Another reported heteroplasmic mt-tRNA^{ALA} mutation located in the acceptor stem is m.5591G>A mutation causing pure myopathy in a patient, specifically affecting limb-girdle muscles (Swalwell et al., 2006). The mutation results in the disruption of a Watson-Crick base pair in the aminoacyl acceptor stem and biochemical defect in Complexes I, III, and IV.

The muscle biopsy of patients harboring m.5650G>A and m.5591G>A mutations revealed significant COX-deficient fibers (McFarland et al., 2008; Swalwell et al., 2006).

Complex IV deficiency was also observed in the skeletal muscle of A5019G mice although it was just a rare occurrence. Histochemical staining in different tissues of A5019G mice showed that the relative frequency of Complex IV deficient cells varied across different tissues, with the intestinal epithelium being the one extremely affected. Looking at the morphology and physiology of the intestinal epithelium, it is a highly regenerative tissue and is composed of a single layer of cells arranged into crypts and protrusions, referred to as villi. Residing at the base of the crypts are terminally differentiated Paneth cells and multipotent intestinal epithelial stem cells (IESCs) which are responsible for proliferation and differentiation, thus resulting in the continuous renewal of the intestinal epithelial cell layer (Van Der Flier & Clevers, 2009). Proliferation and differentiation are high energy-demanding processes that require high oxygen consumption and mitochondrial biogenesis (Jornayvaz & Shulman, 2010; Urbauer et al., 2021). In general, proliferating cells exhibit enhanced glucose uptake resulting in high glycolytic activity, but only a small portion of glucose is used as a source for ATP production, leading to low mitochondrial OXPHOS activity, while the majority of glucose is converted into lactate (Zhu & Thompson, 2019). Interestingly, high mitochondrial activity, in addition to high glycolytic activity, was observed in highly proliferative cells, Lgr5+ crypt base columnar cells (CBCs), as compared to the neighboring Paneth cells based on the findings using mouse small intestine and small intestinal organoid (Rodríguez-Colman et al., 2017). Paneth cells, through glycolysis, also provide lactate to fuel mitochondrial OXPHOS in Lgr5+ CBCs (Rodríguez-Colman et al., 2017). On the other hand, colonic IESCs, through anaerobic glycolysis, convert glucose into lactate (Y.-Y. Fan et al., 2015). Metabolic processes in IESCs, therefore, require mitochondrial activity and mitochondrial fitness is crucial in regulating the IESC niche (Guerbette et al., 2022; Urbauer et al., 2021).

Another mouse model, referred to as tRNA^{ALA} mice or C5024T mice, with a pathogenic, heteroplasmic m.5024C>T mutation was previously developed and characterized in the lab (Kauppila et al., 2016). The m.5024C>T mutation results in a substantial decrease in the steady-state levels of mt-tRNA^{ALA} and a decreased in mitochondrial protein synthesis *in organello*, thereby affecting mitochondrial translation. Physiological abnormalities observed included elevated heart mass in mice 50 weeks old or more, an indicator of cardiomyopathy, and male mutant mice being thinner than normal mice. In contrast to C5024T mice, steady-state levels of mt-tRNA^{ALA} are not affected in A5019G mice, instead, aminoacylation is impacted. The presence of deacylated mt-tRNA^{ALA} molecules, with high relative levels of the m.5019A>G mutation may, therefore, result in an increased ratio of uncharged or deacylated mt-tRNA^{ALA} molecules to charged or aminoacylated mt-tRNA^{ALA} molecules. The impacted

process of aminoacylation then leads to difficulties in translation in Complexes with mtDNA encoded subunits, especially Complexes I and IV. Physiologically, reduced weight in male mice was also occurring, but heart enlargement was not observed. Using single-cell transcriptomic analysis in E8.5 embryos of A5019G and C5024T mice, further investigation was performed to determine the mechanisms of the two mutations (Burr et al., 2023). Results revealed that even though these two mutations are located only 5 base pairs apart in the mt-tRNA[ALA] molecule, different transcriptional responses are occurring directly affecting the organogenesis process (Burr et al., 2023). These findings then show that these two mutations are differentially controlled either at the cellular or tissue level and that tissue selectivity that distinguishes mitochondrial diseases in humans first appears during fetal development in the uterus.

Altogether, this study provides insights into the mechanisms regulating mtDNA heteroplasmy and mitochondrial dysfunction, specifically involving the m.5019A>G mutation in the acceptor stem of the mt-tRNA[ALA] and its effect on aminoacylation resulting in mitochondrial translation defect.

Avenues for future research include utilizing the A5019G mice to test various mammalian mitochondrial genome engineering techniques aimed at reducing mtDNA heteroplasmy and rescuing the animals from OXPHOS biochemical defects. Similar to how C5024T mice were treated with mtZFN containing wild-type-specific monomer and mutant-specific monomer that targeted the m.5024C>T mutation, as well as with mitoTALEN, these mitochondrial nucleases can also be engineered to target the m.5019A>G mutation in A5019G mice (Bacman et al., 2018; Gammage et al., 2018). A5019G mice can also be utilized with recently developed base editing technologies, such as DdCBEs or ZF-DdCBEs. The pathophysiology of mitochondrial dysfunction in the intestinal epithelium of A5019G mice can also be further examined, given that this tissue is profoundly affected and that it plays a crucial role in the mucosal immune system in addition to its roles in digestion and absorption (Peterson & Artis, 2014).

5. MATERIALS AND METHODS

5.1. Generation and maintenance of mice

5.1.1. Mouse husbandry

The mice used in this study were on the C57Bl/6NCrl background strain (Charles River Laboratories, Germany, strain code 27). The mice were housed in the Max Planck Institute for Biology of Ageing (MPI-AGE) Animal Facility and were kept under a constant temperature of 21°C, humidity of 50-60%, and a 12-hour light/dark cycle using a fully automated climate and light control system. The mice were kept with individual ventilation under specific pathogen-free conditions, were provided with drinking water, and were fed *ad libitum* on a standard diet (ssniff M-H Low-Phytoestrogen) or through an enhanced diet with the newly weaned mice or during breeding (ssniff M-Z Low-Phytoestrogen) by Ssniff Spezialdiaeten GmbH. All mice experiments were approved by the Landesamt für Natur, Umwelt und Verbraucherschutz Nordrhein-Westfalen (LANUV) in accordance with the German and European Union regulations, (permit numbers 84-02.02.2015.A103, 81-02.04.2020.A082, 84-02.05.50.15.004, 84-02.04.2016.A420 and 81-02.04.2020.A011). All animal procedures were performed following the guidelines and recommendations of the Federation of European Laboratory Animal Science Associations (FELASA).

5.1.2. Generation of mice with mtDNA mutations

Mutant mice were generated as described before (Kauppila et al., 2016) wherein germline-transmissible mtDNA mutations were generated using female mice which are heterozygous for the PolgA^{mut} allele. To generate heterozygous PolgA$^{+/MUT}$ females, PolgA$^{+/MUT}$ males were crossed with wild-type C57BL/6N females PolgA$^{+/+}$. The PolgA$^{+/MUT}$ females were then crossed with PolgA$^{+/+}$ males. The female offspring with the PolgA$^{+/+}$ genotype were crossed with PolgA$^{+/+}$ males. This was the first backcross (N1). The resulting N2 generation contains females with maternally inherited mtDNA mutations and WT nuclear genome, referred to as founder females. Continuous backcrossing of these females with WT C57Bl/6N males was performed to establish maternal lineages with segregating and clonally expanding maternally inherited mtDNA mutations. In the N3 generation, females were sacrificed. COX/SDH double staining was performed in the colon to screen for the presence of mitochondrial dysfunction. Whole mtDNA sequencing was then conducted from eight of the lineages to identify mtDNA mutations, of which A5019G mice belong to one of the mouse lineages.

5.2. Histochemical assay

5.2.1. Tissue preparation for histochemical assay

Snap-frozen tissues of the heart, kidney, liver, colon, small intestine, skeletal muscle, lung, and brain that were stored at -80°C were cut into 10 μm thick sections using the Cryostat microtome. The sections were then mounted onto the Superfrost plus microscope slides (Thermo Scientific). The slides were stored in sealed slide mailers at -80°C prior to performing the histochemical assay.

5.2.2. Laser-capture microdissection

The colonic tissues for laser-capture microdissection were cut into 18 μm thick sections using the Cryostat microtome. The sections were mounted on polyethylenenaphthalate (PEN) slides (Leica Microsystems). The slides were then stored in sealed slide mailers at -80°C prior to performing the histochemical assay. The samples were subjected to COX/SDH assay as described below and air-dried after dehydration. Single COX-positive and COX-deficient colonic crypts were cut using the laser microdissection microscope LMD7000 (Leica Microsystems). The tissue section was viewed under the 20X objective. White balance was performed, and the single crypts were cut with the following laser setting: power=10 and aperture=5 (Taylor et al., 2003).

5.2.3. COX/SDH assay

The sections were pre-incubated in 1 mL of 0.1M phosphate-buffered saline (PBS) pH 7.0 for 10 min at 18°C. PBS was removed and the following mixture was added to the sections: 800 μL of 3,3'-diaminobenzidine (DAB), 200 μL of 500 μM cytochrome c, and 10 μL catalase. The slides were incubated at 37°C for 30 to 45 min and were then washed in 3 changes of 0.1M PBS. The following mixture was then prepared: 5 mg of nitroblue tetrazolium (NBT), 3.2 mL 0.1M PBS, 400 μL 1.3M sodium succinate, 400 μL 2mM phenazine methosulphate (PMS), and 40 μL sodium azide. From that mixture, 1 mL was applied per slide. The slides were incubated at 37°C for 30 min and were washed in three changes of 0.1M PBS. The sections were dehydrated through increasing EtOH concentrations (50%, 70%, 96%, 100%, 100%) for 2 min in the first three concentrations and for 5 min in the 100% concentrations. The slides were placed in xylene (100%, 100%) for 5 min each and were mounted with Cytoseal, after which the slide cover was put in place (Ross, 2011).

5.2.4. NBTx assay

The sections were pre-incubated in 1 mL of 0.1M PBS for 10 min at 25°C. PBS was removed and NBTx solution (5 mg NBT, 3.2 mL 0.1M PBS, 400 μL of 1.3M sodium succinate, and 400 μL of 2mM phenazine methosulphate) was then added (Simard et al., 2018). 1 mL of NBTx solution was pipetted and spread on each slide. The slides were incubated at 25°C for 20 min. The sections were then washed in dH$_2$O for 2 to 5 min and dehydrated through a series of increasing concentrations of EtOH (50%, 70%, 96%, 100%, 100%) for 2 min in the first three concentrations and for 5 min in the 100% concentrations. The slides were placed in xylene (100%, 100%) for 5 min each and were mounted with Cytoseal, after which the slide cover was put in place (Simard et al., 2018).

5.3. Microscopic visualization

5.3.1. Image acquisition, processing, and analysis

Images were obtained using the Nikon eclipse Ci microscope. Images from NBTx assay samples were processed in the ImageJ/Fiji software (Schindelin et al., 2012) wherein a single macro command/script (Supplementary Data) runs to perform white balance, color deconvolution and threshold (Huang & Wang, 1995), total image analysis, and computation of mean intensity and standard deviation values. After stacking the processed images, the total number of pixels for each intensity value, set in a 0 to 255 range, was assessed with the histogram command.

5.4. Molecular biology methods

5.4.1. Total DNA extraction from tissues

Ear-clip or tail biopsies were lysed by adding 80 μL DNA extraction buffer (25mM NaOH, 0.2mM EDTA) and incubated at 96°C for 45 min. 80 μL of 40mM Tris pH 7.5 – 8.0 was then added to neutralize the lysate. This DNA extraction procedure was used for DNA samples in pyrosequencing and mtDNA sequencing. DNA samples were stored at 4°C until further use. For DNA samples used in quantitative polymerase chain reaction (qPCR), DNA was extracted from snap-frozen heart and small intestinal epithelial tissue using Gentra Puregene Tissue Kit (Qiagen) following the manufacturer's instructions.

5.4.2. Total DNA extraction from laser-capture microdissected tissue samples

After COX/SDH assay, single COX-positive and COX-deficient colonic crypts were cut using the laser microdissection microscope LMD7000 (Leica Microsystems), collected into sterile 0.2 mL PCR tube with 10 μL lysis buffer (50 mM Tris-HCL pH 8.5, 1% Tween-20, 20 mg/mL proteinase K), and centrifuged at 14,000 rpm for 15 min. The samples were then incubated for at least two hours at 55°C followed by a heat-inactivation step at 95°C for 10 min (Taylor et al., 2003). The DNA extract was then used for whole mtDNA sequencing and pyrosequencing.

5.4.3. Whole mtDNA sequencing

Ear clip or tail biopsies and single colonic crypt DNA samples were used for whole mtDNA sequencing. PCR was performed using 30 overlapping M13-tagged primer pairs (Table 1). The PCR reaction consisted of the following: 4 μL 5X PCR buffer, 3.2 μL dNTP mix, 1 μL 10 μM forward primer, 1 μL 10 μM reverse primer, 8.25 μL ddH₂O, 0.05 μL Taq polymerase, and the corresponding DNA volume per type of sample. For ear clip or tail biopsy DNA samples, 40 μL of extracted DNA was diluted with 160 μL ddH₂O was used and 2.5 μL of DNA was used for PCR. For single colonic crypt DNA samples, 1 μL of DNA was used. PCR cycle conditions are listed in Table 2 (Ross et al., 2013a).

Table 1. Sequences of primers used for whole mtDNA sequencing.

Primer	Forward primer sequence (F-seq)	Reverse primer sequence (R-seq)
M13	TGTAAAACGACGGCCAGT	CAGGAAACAGCTATGACC
mp1	(M13F-seq)ATGAACACTCTGAACTAATCC	(M13R-seq)ACTTTGACTTGTAAGTCTAGG
mp2	(M13F-seq)AGAGAAGGTTATTAGGGTGG	(M13R-seq)GGATAAGGTGTTTAGGTAGC
mp3	(M13F-seq)CCATTCCACTTCTGATTACC	(M13R-seq)AAAAGCATGGGCAGTTACG
mp4	(M13F-seq)CTGCTCCTATTATCACTACC	(M13R-seq)GATATAGAGGACTAAGGAGC
mp5	(M13F-seq)TGTCCTAGAAATGGTTCCAC	(M13R-seq)GTACAATAGGAGTGTGGTGGCC
mp6	(M13F-seq)TTGATGAGGATCTTACTCCC	(M13R-seq)GTAGGTTGAGATTTTGGACG
mp7	(M13F-seq)AATCGGTTCTATTCCACTGC	(M13R-seq)AGAATTTGATTGATGTGGTGG
mp8	(M13F-seq)AGGAAAATCAGCACAATTTGG	(M13R-seq)ATGATGTTGGAGTTATGTTGG
mp9	(M13F-seq)CACTCATTCATTGACCTACC	(M13R-seq)TCATTTCAGGTTTACAAGACC
mp10	(M13F-seq)GAAACTTTATCAGACATCTGG	(M13R-seq)GCTGAATTAGCAAGAGATGG
mp11	(M13F-seq)TGTATCCCATAAACACAAAGG	(M13R-seq)TGCGGTACTAGTTCTATAGC
mp12	(M13F-seq)AGAAAGCGTTCAAGCTCAAC	(M13R-seq)AGAACACTATTAGGGAGAGG
mp13	(M13F-seq)TCACTATTCGGAGCTTTACG	(M13R-seq)GATAGTAGAGTTGAGTAGCG
mp14	(M13F-seq)AATGGCGGTAGAAGTCTTAG	(M13R-seq)GCTGATGTAAAGTAAGCTCG

mp15	(M13F-seq)GATACATACTATGTAGTAGCC	(M13R-seq)TTGATGTATCTAGTTGTGG
mp16	(M13F-seq)CACATACATTTACACCTACTACC	(M13R-seq)TTAATGAAGATAACAGTGTACAGG
mp17	(M13F-seq)AAAAAAATTAATGATTTCGACTC	(M13R-seq)CATGAAGCGTCTAAGGTGTG
mp18	(M13F-seq)CATCATCACTCCTATTCTGC	(M13R-seq)GTACTTGAGTGTAGTAGTGCT
mp19	(M13F-seq)ACAGCTATGTACAGCATACG	(M13R-seq)TCTGATGTGTAGTGTATGGC
mp20	(M13F-seq)GCTTTCCACTTCATCTTACC	(M13R-seq)CACAGTTATGTTGGTCATGG
mp21	(M13F-seq)AGAGAACTACTAGCCATAGC	(M13R-seq)TACTCATACTAACAGTGTTGC
mp22	(M13F-seq)TTGACCTTTCAGTGAAGAGG	(M13R-seq)TTGTTTCTGCTAGGGTTGAG
mp23	(M13F-seq)CAAGCCCTCTTATTTCTAGG	(M13R-seq)TTTTTTCGGCGGTAGAAGTAG
mp24	(M13F-seq)GGAATAGTGGGTACTGCAC	(M13R-seq)TTGCTCATGTGTCATCTAGG
mp25	(M13F-seq)TCCAACTTGGTCTACAAGAC	(M13R-seq)GTTTTTAGTTTGTGTCGGAAGCC
mp26	(M13F-seq)CTACTCACCAATATCCTCAC	(M13R-seq)TTTTAAACTAATTACCATTTACTCTG
mp27	(M13F-seq)ACCATCTTAGTTTTCGCAGC	(M13R-seq)GCTAGATTAGCTAGACTTGC
mp28	(M13F-seq)TCTTCATTCTTCTACTATCCC	(M13R-seq)GACAAATCCTGCAAAGATGC
mp29	(M13F-seq)TACTACCATCATTCAAGTAGC	(M13R-seq)GTATAGTAGGGGTGAAATGG
mp30	(M13F-seq)CTTATCTTAACCTGAATTGGG	(M13R-seq)TCTATGGAGGTTTGCATGTG

Table 2. PCR conditions for whole mtDNA sequencing using M13-tagged primers.

Step	Temperature, Time	Cycles
Initial denaturation	94°C, 3 min	
Denaturation	94°C, 35 sec	
Annealing	54°C, 45 sec	25 cycles
Extension	72°C, 2 min	
Final extension	72°C, 5 min	
Hold	8°C, ∞	

PCR clean-up was performed using ExoSAP-IT reagent (Thermo Fisher Scientific). The mixture was incubated at 37°C for 15 min, then inactivated by incubating at 80°C for 15 min. The following master mix was prepared (3 μL water, 1.5 μL 5X Sequencing buffer, 0.17 μL 10 μM primer, and 1 μL Big Dye) and added to the ExoSAP-IT reaction (4.33 μL). PCR cycle conditions are listed in Table 3.

For sequencing clean-up, the Big Dye X-terminator Clean-up protocol was used. 10 μL Big Dye X-terminator solution and 45 μL SAM solution were added to 10 μL sequencing reaction and mixed. Heat-sealing was then applied using the heat-sealing unit at 150°C for 2

sec. The samples were mixed for 20-30 min, centrifuged at 10,000 rpm for 2 min, and loaded to the sequencer, ABI 3730 DNA Analyzer (Thermo Fisher Scientific) for Sanger sequencing. The sequences were resolved with 50 cm capillary arrays and long sequencing run protocols. Sequence assembly was performed using SeqScape Version 2.7 and CLC Main Workbench 7.

Table 3. PCR conditions during the PCR clean-up.

Step	Temperature, Time	Cycles
Initial denaturation	96°C, 1 min	
Denaturation	96°C, 10 sec	
Annealing	58°C, 15 sec	25 cycles
Extension	60°C, 2 min	
Hold	8°C, ∞	

5.4.4. Pyrosequencing

Quantification of m.5019A>G was performed by pyrosequencing using PyroMark Q24 Advanced pyrosequencer (Qiagen). DNA was extracted from ear-clip or tail biopsies. PCR and sequencing primers were designed using Pyromark assay design software v. 2.0 (Qiagen) (Table 4). Sequencing primers and Pyromark annealing buffer (Qiagen) were mixed and added to the sequencing plate. Pyromark binding buffer (Qiagen), Streptavidin Sepharose TM high-performance beads (GE Healthcare), and distilled water were added to the PCR products. The solution was then mixed for 6 min. The solution was purified and denatured using a Pyromark Q24 vacuum workstation (Qiagen) with 70% EtOH, Denaturing buffer, and Washing buffer (Qiagen) and was then heated at 90°C for 2 min. Sequencing was performed using Pyromark Gold Q24 reagents (enzyme mixture, substrate mixture, dATPαS, dGTP, dCTP, and dTTP) following the manufacturer's instructions. Heteroplasmy levels (percentage of mutant base in the sample) were analyzed using the PyroMark analysis software (Qiagen).

Table 4. Primers and their corresponding sequences used in pyrosequencing.

Primer	Sequence
5019-PCR-F	5'-ATACTAGTCCGCGAGCCTTCAAA-3'
5019-PCR-R-BTN	5'-[Btn]AATTGCAAATTCGAAGGTGTAGA-3'
PS-5019aG-Seq	5'-CACACAAGTTTAACTTCTGA-3'

5.4.5. RNA extraction

Total RNA was extracted from snap-frozen tissues using the TRIzol Reagent (Life Technologies). Tissues were pulverized and 50-100 mg were collected. 500 μL of TRIzol was added followed by 200 μL chloroform. After vortex and centrifugation, the upper phase was transferred to a new tube. RNA precipitation was performed by adding 500 μL of isopropanol. The resulting RNA pellet was then washed with 75% EtOH and resuspended in 50 μL nuclease-free water.

5.4.6. Quantitative PCR and Reverse transcription qPCR

For quantitative PCR (qPCR), DNA samples used were extracted with Gentra Puregene Tissue Kit (Qiagen) and DNA concentration was measured with the Nanodrop. A subset was then diluted to the final concentration of 2.5 ng/μL. A standard curve covering the dilution factor range was created. PCR mix consisting of TaqMan mix, Probe (Table 5), and nuclease-free water was prepared and added to the DNA. The samples were run on the QuantStudio 6 RealTime PCR System (Applied Biosystems).

For reverse transcription qPCR (RT-qPCR), 10 μg RNA was used. DNase treatment was performed by adding the following to the RNA: 5 μ<L 10X TURBO DNase buffer (Thermo Fisher Scientific), 1 μL TURBO DNase, and water up to 50 μL final volume. The mixture was incubated at 37°C for 20-30 min. 5 μL DNase Inactivation Reagent was then added to the mix and incubated at RT for 5 min with occasional mixing. The mix was centrifuged at 10000 x g for 1.5 min and the supernatant was transferred to a new tube. DNase-treated RNA was then used for cDNA synthesis using the High-Capacity cDNA Reverse Transcription Kit (Applied Biosystems). 10X RT Buffer, 25X dNTP mix (100mM), 10X random primers, Reverse Transcriptase, and nuclease-free water were added to 1.6 μg of DNase-treated RNA. The RT reaction was incubated in the following conditions: 25°C for 10 min, 37°C for 120 min, and 85°C for 5 min. A subset of the cDNA was diluted to 1:10. A few μL of the non-diluted cDNA were pooled, and serial dilutions were made. Each point was in triplicate. PCR mix included the following: 4.8 μL TaqMan mix, 0.5 μl Probe (Table 5), 3.7 μL nuclease-free H_2O, and 1 μL cDNA. The plate was spun at 1,200 rpm for 1 min. The samples were run on the QuantStudio 6 RealTime PCR System (Applied Biosystems).

Table 5. Taqman probes used in qPCR and RT-qPCR.

Taqman probe	Species	Catalog number
mt-Atp6	Mouse	Mm03649417-g1
mt-Co1	Mouse	Mm04225243_g1
mt-Co2	Mouse	Mm03294838_g1
mt-Co3	Mouse	Mm04225261_g1
mt-Cytb	Mouse	Mm04225271_g1
mt-Nd2	Mouse	Mm04225288_s1
mt-Nd4	Mouse	Mm04225294_s1
mt-Nd5	Mouse	AIHSNT9
mt-Nd6	Mouse	AIVI3E8
18S rRNA	Human	Hs99999901_s1

5.4.7. Northern blot

Total RNA was extracted from frozen ground heart and small intestinal epithelial tissue using TRIzol reagent (Life Technologies). 2 µg of RNA sample was used, and NorthernMax-Gly Sample Loading Dye (Ambion) was added to the sample (1:1 ratio). Samples were denatured at 65°C for 20 min, then placed on ice for 2 min, and were loaded to 1.2% RNA MOPS/formaldehyde gel. Run was performed at 80V for 15 min, then 120V for 2 hr and 15 min. RNA migration was checked in the UV transilluminator. The gel was incubated in DEPC water for 15 min (2X). The Hybond-N+ nylon hybridization membrane (GE Healthcare) was incubated in DEPC water for 15 min. The gel and the membrane were then incubated in 20X saline-sodium citrate (SSC) buffer for 20 min. RNA transfer setup was assembled for the separated RNA in the gel to be transferred to the nylon membrane through the capillary system. A glass dish was filled with 20X SSC halfway and a glass plate and blotting paper was placed as a salt bridge. Blotting papers soaked in 20X SSC were placed on top of the salt bridge. The gel was then placed face down on top of the blotting papers. Then the Hybond-N+ membrane (Amersham) was placed on top of the gel. Blotting papers soaked in 20X SSC were placed on top of the membrane. A stack of paper towels was placed on top then with a glass plate and a filled 1 L glass bottle. The transfer was left overnight. Then, the membrane was incubated in 2X SSC for 5 min under slow agitation, air dried, and UV-crosslinked twice using UVC500 crosslinker (GE Healthcare).

For mt-mRNAs, RNA was labeled with radioactive probes (Table 6) by first incubating the membrane in 15 ml PerfectHyb Plus Hybridization buffer (Sigma) at 65°C for ~1 hr. RNA probe was prepared using the Prime-IT II Random Primer Labeling kit (Agilent Technologies)

consisting of the following: Random 9-mer primers (Agilent), mRNA probe (30 ng/μL), and DEPC water. The mixture was incubated at 95°C for 5 min to denature the primers, then placed on ice for 2 min. The following were then added to the master mix: 5X dCTP buffer (with all dNTPs except dCTPs) (Agilent), Exo (Roger, Munoz-Gomez, & Kamikawa) Klenow polymerse 5 U/μL (Agilent), and 50 μCi α-^{32}P-CTP (PerkinElmer). The mixture was incubated at 37°C for 15 min to 1 hr and the probe was purified using G-50 columns (IllustraTM Probe Quant TM G-50 Micro Columns, GE Healthcare). 50 μL purified probe was added to the hybridization buffer used in pre-incubating the membrane and incubated at 65°C overnight. The membrane was first washed with 25 mL 2X SSC plus 0.1% SDS at room temperature for 15 min. Then washed with 25 mL 2X SSC plus 0.1% SDS at 65°C for 15 min. Then washed with 25 mL 0.2X SSC plus 0.1% SDS at 65°C for 15 min. The membrane was sealed in a plastic bag and exposed to a phosphor screen by placing them both in a film cassette. The film was scanned using Typhoon FLA 7000 (GE Healthcare) to visualize the mRNA.

For mt-tRNAs, a non-radioactive procedure was performed. RNA was first transferred to the Hybond-NX nylon hybridization membrane (Amersham). After overnight transfer and UV-crosslinking, the membrane was incubated with pre-hybridization solution (5 mL 20X SSC, 0.4 mL 1M Na_2HPO_4 pH 7.6, 14 mL 10% SDS, 0.2 mL 25X RNA secure (Ambion), and 20 μL 100 mg/ml Heparin) at 50°C for 1 hr. 10 μL of biotinylated oligonucleotide probes (100 μM) specific to mitochondrial tRNAs was then added to the pre-hybridization solution and incubated at 50°C for 3 hours or overnight. The membrane was then washed with 20 mL oligo hybridization wash (30 g SDS, 90 mL 20X SSC pH 7.2, 15 mL 1M Na_2HPO_4 pH 7.6, and DEPC-water up to 600 mL) at 50°C for 5 min and 20 min. Signal detection was performed by adding 20 mL hybridization TBST (0.05% Tween-20), 0.75 μL Streptavidin secondary (IRdye, 800CW Streptavidin LI-COR) to the membrane and incubating at 22°C for 15 min and making sure the hybridization oven door was covered. Membrane washing was done by incubating the membrane with 20 mL TBST (0.05% Tween-20) at 22°C for 5 min. The membrane was scanned using the Odyssey machine at 800 nm. Probe stripping was done by rinsing the membrane in DEPC water, then adding Stripping solution (DEPC--water, 0.2 mL EDTA, and 20% SDS), and incubating at 80°C for 15 min. Then, the membrane was rinsed using 50 mL 2X SSC at room temperature for 5-10 min on a roller.

5.4.8. Southern blot

DNA was extracted from pulverized heart and small intestinal epithelial tissue using the Gentra Puregene Tissue Kit (Qiagen). 5 μg of DNA was used, and DNA digestion was performed using 20 μL 10X Buffer and 6 μL *SacI* enzyme (New England Biolabs) and incubated at 37°C overnight. 8 μL 5M NaCl and 400 μL EtOH were added, and the mixture was incubated at -80°C for 2 hr or overnight. It was then centrifuged at 14,000 g for 30 sec at room temperature. Washed with 70% EtOH and centrifuged again at 14,000 g for 30 sec. The pellet was air-dried, 20 μL Tris-HCl pH 7.4 or nuclease-free H_2O was added and incubated at 55°C for 15 to 30 min until it was dissolved. A 6X loading buffer was then added. Samples were loaded in 0.8% agarose gel in 0.5% TBE and run at 30-40V overnight. DNA migration was checked in the UV transilluminator. The gel was incubated in 0.2M HCl for 10 min, in dH_2O for 5 min, in denaturation solution for 20 min, in two washes with dH_2O for 5 min each, in neutralization solution for 20 min, and in two washes with dH_2O for 5 min each, in 20X SSC for 20 min. In parallel, the Hybond-N$^+$ membrane (Amersham) was incubated in dH_2O for 5 min, then in 20X SSC for 20 min. The transfer setup was assembled for the DNA in the gel to be transferred to the Hybond-N$^+$ membrane (Amersham) membrane through the capillary system. A glass dish was filled with 20X SSC halfway and a glass plate and blotting paper were placed as a salt bridge. Blotting papers soaked in 20X SSC were placed on top of the salt bridge. The gel was then placed face down on top of the blotting papers. Then the membrane was placed on top of the gel. Blotting papers soaked in 20X SSC were placed on top of the membrane. A stack of paper towels was placed on top then with a glass plate and a filled 1 L glass bottle. The transfer setup was left overnight. Then, the membrane was incubated in 2X SSC for 5 min under slow agitation, air-dried, and UV-crosslinked twice using a UVC500 crosslinker (GE Healthcare).

DNA was labeled with radioactive probes (Table 6). First, 15 mL PerfectHyb Plus Hybridization buffer (Sigma) was added to the membrane and was incubated at 65°C for ~1 hr. In parallel, probe labeling was prepared using the Prime-IT II Random Primer Labeling kit (Agilent Technologies) consisting of the following: Random 9-mer primers (Agilent), DNA probe (30 ng), and nuclease-free water. DNA probes used were pAM1, which recognized mtDNA, and 18S, which recognized nuclear DNA. The mixture was incubated at 95°C for 5 min to denature the primers. The following were then added to the master mix: 5X dCTP buffer (with all dNTPs except dCTPs) (Agilent), Exo (-) Klenow polymerase 5 U/μL (Agilent), and 50 μCi α-^{32}P dCTP (PerkinElmer). The mixture was incubated at 37°C for 15 min to 1 hr and the probe was purified using G-50 columns (IllustraTM Probe Quant TM G-50 Micro Columns, GE

Healthcare). A 50 μL purified probe was added to the hybridization buffer used in pre-incubating the membrane and incubated at 65°C overnight. The membrane was first washed with 25 mL 2X SSC plus 0.1% SDS at room temperature for 15 min. Then washed with 25 mL 2X SSC plus 0.1% SDS at 65°C for 15 min. Then washed with 25 mL 0.2X SSC plus 0.1% SDS at 65°C for 15 min. The membrane was sealed in a plastic bag and exposed to a phosphor screen by placing them both in a film cassette. The film was scanned using Typhoon FLA 7000 (GE Healthcare) to visualize the mtDNA.

Table 6. List of probes used for Northern and Southern blotting.

Probe	Sequence
mt-Cox3	CTTTTAACCCTTGGCCTACTCACCAATATCCTCACAATATATCAATGATGACGAGACGTAATTCGTGAAGGAACCTACCAAGGCCACCACACTCCTATTGTACAAAAAGGACTACGATATGGTATAATTCTATTCATCGTCTCGGAAGTATTTTTCTTTGCAGGATTCTTCTGAGCGTTCTATCATTCTAGCCTCGTACCAACACATGATCTAGGAGGCTGCTGACCTCCAACAGGAATTTCACCACTTAACCCTCTAGAAGTCCCACTACTTAATACTTCAGTACTTCTAGCATCAGGTGTTTCAATTACATGAGCTCATCATAGCCTTACAGAAGGTAAACGAAACCACATAAATCAAGCCCTACTAATTACCATTATACTAGGACTTTACTTCACCATCCTCCAAGCTTCAGAATACTTTGAAACATCATTCTCCATTTCAGATGGTATCTATGGTTCTACATTCTTCATGGCTACTGGATTCCATG GACTTCATGTAATTATTGGATCAACATTCCTTATTGTTTGCCTACTA
mt-Nd5	ACAAGACATCCGAAAAATAGGAAACATCACAAAAATCATACCATTCACATCATCATGCCTAGTAATCGGAAGCCTCGCCCTCACAGGAATACCATTCCTAACAGGGGTTCTACTCAAAAGACCTAATTATTGAAGCAATTAATACCTGCAACACCAACGCCTGAGCCCTACTAATTACACTAATCGCCACTTCTATAACAGCTATGTACAGCATACGAATCATTTACTTCGTAACAATAACAAAACCGCGTTTTCCCCCCCTAATCTCCATTAACGAAAATGACCCAGACCTCATAAACCCAATCAAACGCCTAGCATTCGGAAGCATCTTTGCAGGATTTGTCATCTCATATAATATTCCACCAACCAGCATTCCAGTCCTCACAATACCATGATTTTTAAAAACCACAGCCCTAATTATTTCAGTATTAGGATTCCTAATCGCACTAGAACTAAACAACCTAACCATAAAACTATCAATAAATAAAGCAAATCCATATTCATCCTTCTCAACTTTACTGGGGTTTTTCCCATCTATTATTCACCGCATTACACC
mt-Nd6	GTTCATTATTTTTGGTTGGTTGTCTTGGGTTAGCATTAAAGCCTTCACCTATTTATGGAGGTTTAGGTTTAATTGTTAGTGGGTTTGTTGGTTGTTTAATGGTTTTAGGGTTTGGTGGATCGTTTTTAGGTTTAATAGTTTTTTTTAATTTATTTAGGGGGGGATGTTGGTTGTGTTTGGATATACGACTGCTATAGCTACTGAGGAATATCCAGAGACTTGGGGATCTAACTGATTAATTTTGGGTTTTTTAGTATTGGGGGTGATTATAGAGGTTTTTTTTAATTTGTGTGCTTAATTATTATGATGAAGTTGGAGTAATTAATCTTGATGGTTTGGGAGATTGGTTGATGTATGAGGTTGATGATGTTGGAGTTATGTTGGAAGGAGGGATTGGGGTAGCGGCAATATATAGTTGTGCTACTTGAATGATGGTAGTAGCTGGGTGATCTTTGTTTGCGGGTATTTTTATT
18S rRNA	GGTCTACAAGACGCCACATCCCCTATTATAGAAGAGCTAATAAATTTCCATGATCACACACTAATAATTGTTTTCCTAATTAGCTCCTTAGTCCTCTATATCATCTCGCTAATATTAACAACA

	AAACTAACACATACAAGCACAATAGATGCACAAGAAGTTGAAACCATTTGAACTATTCTAC CAGCTGTAATCCTTATCATAATTGCTCTCCCCTCTCTACGCATTCTATATATAATAGACGAA ATCAACAACCCCGTATTAACCGTTAAAACCATAGGGCACCAATGATACTGAAGCTACGAA TATACTGACTATGAAGACCTATGCTTTGATTCATATATAATCCCAACAAACGACCTAAAAC CTGGTGAACTACGACTGCTAGAAGTTGATAACCGAGTCGTTCTGCCAA
pAM1	Whole mtDNA genome sequence in pACYC177 plasmid backbone (Bibb et al., 1981)

5.4.9. In vitro transcription assay

In vitro transcription assay was carried out by the Falkenberg research group. Mouse mitochondrial LSP regions, from 16,110 to 16,259, designated as LSP "A" – WT, and from 16,120 to 16,259 designated as either LSP "B" – WT or LSP "B" – mutant (with m.16232A>T mutation), in linear dsDNA form, followed by a random DNA sequence upstream of the promoter, were produced by Eurofins Genomics (GeneStrands). LSP "A" – WT and LSP "B" – WT; and LSP "A" – WT and LSP "B" – mutant, were cloned in pUC19 vector under HindIII/PstI and PstI/BamHI respectively. The plasmids were linearized using NdeI and SapI to produce run-off transcripts (about 321 nt for LSP "A" – WT and 302 nt LSP "B"), which were then used to build the dual promoter templates for the *in vitro* transcription assay. According to previously reported procedures (Gaspari et al., 2004; Posse et al., 2014), recombinant mouse Polrmt, Tfb2m, and Tfam were produced and purified. *In vitro* transcription reactions (in 25 μL reaction volume) consisting of a buffer containing 25 mM Tris-HCl pH 8.0, 10 mM MgCl$_2$, 64 mM NaCl, 100 μg/mL BSA, 1 mM DTT, 400 μM ATP, 150 μM GTP, 150 μM CTP, 10 μM UTP, 0.02 μM α-32P UTP (3000 Ci/mmol, Hartmann Analytic GmbH) and 4 U RNase inhibitor Murine (New England Biolabs), wherein 4 nM DNA template, 30 nM Polrmt, 40 nM Tfb2m and 0.3, 0.6, 1.1, or 2.2 μM Tfam were added. The reactions were prepared on ice, started with ribonucleotide addition, and incubated at 32°C for 10 min. The reactions were then stopped by adding the stop buffer (10 mM Tris-HCl pH 8.0, 200 mM NaCl, 1 mM EDTA, and 100 μg/mL proteinase K) and incubated at 42°C for 45 min. Pellets of ethanol-precipitated transcripts were resuspended in the loading buffer (98% formamide, 10 mM EDTA, 0.025% xylene cyanol, and 0.025% bromophenol blue). 125 μL reaction volume was used for time-course experiments. At stated times, 25 μL was removed, and the reaction was stopped using the stop buffer. Reaction products were loaded on a denaturing 4% polyacrylamide gel and viewed in the Phosphoimager. Results were analyzed using the Multi Gauge software.

5.4.10. Aminoacylation assay

The aminoacylation assay was performed by the Minczuk research group. Aminoacylation assay was conducted on transfection-immortalized mouse embryonic fibroblasts (MEFs) derived from A5019G mice. Total RNA was extracted using TRIzol. RNA preparations were resuspended in 100 mM NaOAc, pH 5.0, and placed on ice. $NaIO_4$ solution was added to 50 mM and incubated at room temperature for 30 min. Glucose was added to 100 mM and the mixture was incubated at room temperature for 5 min. Samples were filtered through MicroSpin G-25 spin columns (GE Healthcare). The RNA was precipitated with ethanol. The samples were centrifuged at 12,000 g at 4°C for 5 min. The RNA pellets were resuspended in 1 M Lysine pH 7.4 at 45°C for 1 hr and then filtered again through the G-25 spin columns. Alongside the $NaIO_4$-treated samples, control samples were treated with 100 mM NaCl instead of $NaIO_4$. For the deacylated negative control sample, 20 μg total mouse RNA was incubated with 200 mM Tris-HCl at 75°C for 5 min. The samples were then precipitated and resuspended in 100 mM NaOAc pH 5.0. 1.5 μg - 5 μg samples mixed with Gel Loading Buffer II (Invitrogen) were loaded in high-resolution denaturing Urea PAGE (8 M Urea, 10% polyacrylamide (19:1 acrylamide/bis), 1X Glycerol tolerant buffer (GTB)) and run at 75 W for about 5 hr. Northern blotting was performed using the Hybond-N+ membrane (Amersham) and cross-linked in a CL-1000 UV crosslinker. The blots were then hybridized using riboprobe primers.

5.5. Biochemistry methods

5.5.1. Protein isolation

Snap-frozen tissues of the heart and small intestinal epithelial tissue were pulverized using liquid nitrogen and a mortar and pestle. Powdered tissues were homogenized in protein lysis buffer (25 mM HEPES pH 8, 5 mM $MgCl_2$, 0.05 mM EDTA pH 8, 140 mM NaCl, and 1X protease inhibitor). NP-40 (10% solution: 400 μL buffer + 400 μL NP-40) was added to a final concentration of 1%. Mixture was homogenized up and down with pipet tip. Sonication was performed 10x 30/30 (high frequency). Centrifuged at 13,000 rpm for 10 min at 4°C. The supernatant was transferred to a new tube.

5.5.2. Protein assay

Protein quantification was conducted using *DC* (detergent compatible) Protein Assay (Bio-Rad). The protein sample was diluted and 5 μL was placed in the Greiner 96 flat bottom transparent plate (Sigma-Aldrich). Standards used were 0 mg/mL, 0.125 mg/mL, 0.25 mg/mL,

0.5 mg/mL, 1 mg/mL, and 2 mg/mL BSA. Samples and standards were in triplicates. 20 μL Reagent S was mixed with 1 mL Reagent A and 25 μL of this mix was added to the sample. 200 μL Reagent B was then added. The samples were incubated at room temperature for 15 min. Absorbance was measured at 750 nm using plate reader Infite 200 Pro (Tecan).

5.5.3. Western blot

30 μg of protein lysates from heart and intestinal epithelial tissues were resuspended in NuPAGE LDS 4X Sample Buffer with 20X DTT and were incubated at 37°C for 10 min. Proteins were separated by SDS-PAGE in 4-12% Bis-Tris precast gel (Thermo Fisher Scientific) using Novex Midi-Cell (Thermo Fisher Scientific). 20 μL samples and 8 μL Spectra Multicolor Broad Range Protein Ladder (Thermo Fisher Scientific) were loaded to the gel and run in 1X NuPAGE MOPS SDS Running Buffer at 200V for 48 min. Proteins from the gel were then transferred to polyvinylidene difluoride (PVDF) membrane (GE Healthcare) in a Criterion Blotter (Bio-Rad) system consisting of the following transfer stack: cathode (black), sponge, filter paper, gel, membrane, filter paper, sponge, anode (red), with 1X Transfer buffer (25 mM Tris base, 190 mM glycine, 20% methanol) pH 8.3. The membrane was blocked for 1 hr at room temperature or overnight at 4°C using blocking buffer (5% milk). The membrane was then incubated with appropriate dilutions of primary antibody (Table 7) in blocking buffer at 4°C overnight, washed in three washes of TBST (1X Tris-Buffered Saline, 0.1% Tween 20), 5 min each, and incubated with the conjugated secondary antibody (Table 7), ECL Anti-mouse IgG horseradish peroxidase linked whole antibody (from sheep) (Bio-Rad), in blocking buffer at room temperature for 1 hr. The membrane was then washed in three washes of TBST (5 min for each wash). Signal development was detected using ECL Western Blotting Detection Reagent (GE Healthcare) and scanned in LI-COR 43 imaging (LI-COR Biosciences).

Table 7. Primary and secondary antibodies used for Western blotting.

Protein target	Host	Dilution	Company	Catalog number
Anti-OXPHOS cocktail	Mouse	1:250	Abcam	ab110413
Anti-β-Actin	Mouse	1:2000	Abcam	ab8226
Anti-mouse IgG - HRP	Sheep	1:2,500	GE Healthcare	NXA931

5.5.4. In organello translation

Small intestinal epithelial tissue samples were collected in falcon tubes. The samples were washed with 2X PBS and centrifuged at 6,000 rpm for 5 min (these steps were performed

twice). 5 mL prewarmed labeling medium (DMEM high glucose without glutamine, methionine, and cysteine, 100X GlutaMAX-I, 100 mM sodium pyruvate solution, fetal bovine serum (Sigma) dialyzed) was added and the mixture was incubated at 37°C with 5% CO_2 for 30 min. A fresh stock of 1 mg/mL emetine (Sigma) was prepared and filtered sterilized. 250 μL of emetine stock solution was added per tube and was incubated for 5 min. 400 μCi of ^{35}S methionine/cysteine mix (Perkin-Elmer) was added and the samples were incubated at 37°C for 60 min (pulse). The medium was removed, and the samples were left on the bench at room temperature for 5 min (chase). The samples were washed 3X with PBS. 1 mL of cold PBS was added. The mixture was centrifuged at 1,500 g at 4°C for 5 min. The supernatant was discarded, and the pellet was resuspended in 50-100 μL RIPA lysis buffer. The samples were lysed for 30 min on ice, then centrifuged at 3,000 rpm at 4°C for 5 min. The supernatant was then collected in a new tube. The volume corresponding to 50 μg total proteins was collected and mixed with sample loading buffer. The samples were incubated at room temperature for 30 min and loaded on a 12% Tris-Bis NuPAGE gel. 400 mL of 1X NuPAGE MES SDS Running Buffer from 20X stock was used and run in a mini tank at 150 V for 1 hr. The gel was stained with Coomassie solution (20% EtOH, 10% acetic acid, 2 tablets PhastGelTM BlueR (GE Healthcare) for the Coomassie, 800 mL solution) for 30 min and destained in Destainer solution (20% EtOH, 10% acetic acid) for 1 hr or more. The gel was scanned to assess the loading and then incubated in the amplifier solution (GE Healthcare).

5.5.5. Peptide digestion and clean-up for mass spectrometry

Lysis buffer was added to the protein pellet and heated at 95°C for 10 min with shaking at 700 rpm. The lysate was placed in the Bioruptor with the following settings: 30 sec sonication, 30 sec break, 10 cycles, high performance and centrifuged at 20000 g for 20 min. 2 μL of supernatant was diluted at least 10 times with 20mM Tris to 20 μL. The concentration of the protein solution was measured with NanoDrop. 300 μg of sample was diluted 10 times with 20mM Tris and digested with trypsin (1:200 trypsin to protein ratio). The digest was left overnight at 37°C. 50% formic acid (FA) with a final concentration of 1% was added to stop the digestion. The sample was then centrifuged at 20,000 g for 10 min. Peptide clean-up was performed by adding 200 μL methanol to C18-SD tip and centrifuging for 50-60 sec. 200 μL 40% acetonitrile (ACN)/0.1% FA was then added and centrifuged for 60-80 sec. It was equilibrated by adding 200 μL 0.1% FA by centrifuging at 60-80 sec. 0.1% FA was added, then the digest of the sample was added and centrifuged for 1-2 min. The tip was washed with 200 μL 0.1% FA by centrifuging for 1-2 min. This step was repeated until the tip was dry

completely. The peptides were eluted with 100 μL 40% ACN/0.1% FA and centrifuged at 300 g for 6 min. The eluates were transferred to a new tube and dried using a Speed-Vac at 45°C for 45 min. The digest was resuspended with 20 μL 0.1% FA. The concentration was measured with the NanoDrop. 4 μg of peptide was transferred to a new tube, dried in Speed-Vac, and reconstituted in 9 μL of 0.1M triethylammonium bicarbonate (TEAB) buffer.

5.5.6. Mass spectrometry

Mass spectrometry (MS) was performed by the MPI-AGE Proteomics Core Facility. Tandem mass tag (TMTpro, Thermo Fisher Scientific cat. No A44522) labeling was carried out according to the manufacturer's instruction with the following changes: 0.5 mg of TMTPro reagent was re-suspended with 33 μL of anhydrous ACN. Seven microliters of TMTPro reagent in ACN was added to 9 μL of clean peptide in 0.1M TEAB. The final ACN concentration was 43.75% and the ratio of peptides to TMTPro reagent was 1:20. After 60 min of incubation the reaction was quenched with 2 μL of 5% hydroxylamine. Labelled peptides were pooled, dried, re-suspended in 200 μL of 0.1% formic acid (FA), split into two equal parts, and desalted using home-made STAGE tips (Li et al., 2021). One of the two parts was fractionated on a 1 mm x 150 mm ACQUITY column, packed with 130 Å, 1.7 μm C18 particles (Waters cat. no SKU: 186006935), using an Ultimate 3000 UHPLC (Thermo Fisher Scientific). Peptides were separated at a flow of 30 μL/min with a 88 min segmented gradient from 1% to 50% buffer B for 85 min and from 50% to 95% buffer B for 3 min; buffer A was 5% ACN, 10mM ammonium bicarbonate (ABC), buffer B was 80% ACN, 10mM ABC. Fractions were collected every three minutes, and fractions were pooled in two passes (1 + 17, 2 + 18 … etc.) and dried in a vacuum centrifuge (Eppendorf). Dried fractions were re-suspended in 0.1% formic acid (FA) and separated on a 50 cm, 75 μm Acclaim PepMap column (Thermo Fisher Scientific, Product No. 164942) and analyzed on an Orbitrap Lumos Tribrid mass spectrometer (Thermo Fisher Scientific) equipped with a FAIMS device (Thermo Fisher Scientific). The FAIMS device was operated in two compensation voltages, -50 V and -70 V. Synchronous precursor selection-based MS3 was used for the acquisition of the TMTPro reporter ion signals. Peptide separations were performed on an EASY-nLC1200 using a 90 min linear gradient from 6% to 31% buffer; buffer A was 0.1% FA, buffer B was 0.1% FA, 80% ACN. The analytical column was operated at 50°C. For proteomic data analysis, please refer to Section 5.7.1.

5.6. Phenotypic characterization

5.6.1. Body and heart weight

The body weight of mice was measured after CO_2 euthanasia and cervical dislocation. The whole heart is cut and washed in PBS buffer, dried down, and weighed.

5.6.2. Metabolic phenotyping

Phenotyping experiments were carried out by the MPI-AGE Phenotyping Core Facility. Mice were housed in PhenoMaster (TSE Systems) cages and acclimatized for several days. Indirect calorimetry, food and liquid intake, and locomotor activity were monitored and measured for two days. Results were analyzed through the PhenoMaster software.

5.7. Data and statistical analyses

5.7.1. Proteomic data analysis

Proteomic data were analyzed using Proteome Discover, version 2.4 (Thermo Fisher Scientific) by the MPI-AGE Proteomics Core Facility. The isotope purity correction factors, provided by the manufacturer, were included in the analysis. Differential expression analysis was performed using *limma*, version 3.34.9 (Ritchie et al., 2015) in R, version 3.4.3 (R Core Team, 2017).

5.7.2. Statistical analysis

Statistical analyses were performed using GraphPad Prism v9. All values were expressed as mean $\pm$ standard error of mean (SEM), unless otherwise stated. Statistical significance was set at $P<0.05$. Detailed information on the analyses used can be found in the figure legends.

REFERENCES

Abbott, J., Francklyn, C., & Robey-Bond, S. (2014). Transfer RNA and human disease. *Frontiers in Genetics*, *5*(158), 1–18.

Agaronyan, K., Morzov, Y. I., Anikin, M., & Temiakov, D. (2015). Replication-transcription switch in human mitochondria. *Science*, *347*(6221), 548–551.

Aguilar, K., Comes, G., Canal, C., Quintana, A., Sanz, E., & Hidalgo, J. (2022). Microglial response promotes neurodegeneration in the Ndufs4 KO mouse model of Leigh syndrome. *GLIA*, *70*(11), 2032–2044.

Aibara, S., Singh, V., Modelska, A., & Amunts, A. (2020). Structural basis of mitochondrial translation. *ELife*, *9*, 1–17.

Alexeyev, M. F., Venediktova, N., Pastukh, V., Shokolenko, I., Bonilla, G., & Wilson, G. L. (2008). Selective elimination of mutant mitochondrial genomes as therapeutic strategy for the treatment of NARP and MILS syndromes. *Gene Therapy*, *15*(7), 516–523.

Anderson, S., Bankier, A. T., Barrell, B. G., De Bruijn, M. H. L., Coulson, A. R., Drouin, J., Eperon, I. C., Nierlich, D. P., Roe, B. A., Sanger, F., Schreier, P. H., Smith, A. J. H., Staden, R., & Young, I. G. (1981). Sequence and organization of the human mitochondrial genome. *Nature*, *290*, 457–465.

Andreazza, S., Samstag, C. L., Sanchez-Martinez, A., Fernandez-Vizarra, E., Gomez-Duran, A., Lee, J. J., Tufi, R., Hipp, M. J., Schmidt, E. K., Nicholls, T. J., Gammage, P. A., Chinnery, P. F., Minczuk, M., Pallanck, L. J., Kennedy, S. R., & Whitworth, A. J. (2019). Mitochondrially-targeted APOBEC1 is a potent mtDNA mutator affecting mitochondrial function and organismal fitness in Drosophila. *Nature Communications*, *10*, 1–14.

Bacman, S. R., Kauppila, J. H. K., Pereira, C. V., Nissanka, N., Miranda, M., Pinto, M., Williams, S. L., Larsson, N. G., Stewart, J. B., & Moraes, C. T. (2018). MitoTALEN reduces mutant mtDNA load and restores tRNAAla levels in a mouse model of heteroplasmic mtDNA mutation. *Nature Medicine*, *24*(11), 1696–1700.

Bacman, S. R., Williams, S. L., Pinto, M., Peralta, S., & Moraes, C. T. (2013). Specific elimination of mutant mitochondrial genomes in patient-derived cells by mitoTALENs. *Nature Medicine*, *19*(9), 1111–1113.

Bailey, C. M., & Anderson, K. S. (2010). A mechanistic view of human mitochondrial DNA polymerase γ: Providing insight into drug toxicity and mitochondrial disease. In *Biochimica et Biophysica Acta - Proteins and Proteomics*, *1804*(5), 1213–1222.

Baines, H. L., Stewart, J. B., Stamp, C., Zupanic, A., Kirkwood, T. B. L., Larsson, N. G., Turnbull, D. M., & Greaves, L. C. (2014). Similar patterns of clonally expanded somatic mtDNA mutations in the colon of heterozygous mtDNA mutator mice and ageing humans. *Mechanisms of Ageing and Development*, *139*, 22–30.

Baughman, J. M., Perocchi, F., Girgis, H. S., Plovanich, M., Belcher-Timme, C. A., Sancak, Y., Bao, X. R., Strittmatter, L., Goldberger, O., Bogorad, R. L., Koteliansky, V., &

Mootha, V. K. (2011). Integrative genomics identifies MCU as an essential component of the mitochondrial calcium uniporter. *Nature*, *476*(7360), 341–345.

Bayona-Bafaluy, M. P., Blits, B., Battersby, B. J., Shoubridge, E. A., & Moraes, C. T. (2005). Rapid directional shift of mitochondrial DNA heteroplasmy in animal tissues by a mitochondrially targeted restriction endonuclease. *Proceedings of the National Academy of Sciences*, *102*, 14392–14397.

Behl, C. (2016). Breaking BAG: The Co-Chaperone BAG3 in Health and Disease. *Trends in Pharmacological Sciences*, *37*, 672–688.

Bernt, M., Braband, A., Schierwater, B., & Stadler, P. F. (2013). Genetic aspects of mitochondrial genome evolution. *Molecular Phylogenetics and Evolution*, *69*(2), 328–338.

Bhargava, K., Templeton, P., & Spremulli, L. L. (2004). Expression and characterization of isoform 1 of human mitochondrial elongation factor G. *Protein Expression and Purification*, *37*(2), 368–376.

Bianchetti, R., Lucchini, G., Crosti, P., & Tortora, P. (1977). Dependence of Mitochondrial Protein Synthesis Initiation on Formylation of the Initiator Methionyl-tRNAf. *Journal of Biological Chemistry*, *252*(8), 2519–2523.

Bibb, M. J., Van Etten, R. A., Wright, C. T., Walberg, M. W., & Clayton, D. A. (1981). Sequence and Gene Organization of Mouse Mitochondrial DNA. *Cell*, *26*, 167–180.

Bleazard, W., Mccaffery, J. M., King, E. J., Bale, S., Mozdy, A., Tieu, Q., Nunnari, J., & Shaw, J. M. (1999). The dynamin-related GTPase Dnm1 regulates mitochondrial fission in yeast. *Nature Cell Biology*, *1*, 298–304.

Blumberg, A., Rice, E. J., Kundaje, A., Danko, C. G., & Mishmar, D. (2017). Initiation of mtDNA transcription is followed by pausing, and diverges across human cell types and during evolution. *Genome Research*, *27*(3), 362–373.

Bock, F. J., & Tait, S. W. G. (2020). Mitochondria as multifaceted regulators of cell death. *Nature Reviews Molecular Cell Biology*, *21*(2), 85–100.

Boggan, R. M., Lim, A., Taylor, R. W., McFarland, R., & Pickett, S. J. (2019). Resolving complexity in mitochondrial disease: Towards precision medicine. *Molecular Genetics and Metabolism*, *128*(1-2), 19–29.

Boyer, P. D., Cross, R. L., & Momsen, W. (1973). A New Concept for Energy Coupling in Oxidative Phosphorylation Based on a Molecular Explanation of the Oxygen Exchange Reactions (protein conformational change/uncouplers/mitochondria). *Proc. Nat. Acad. Sci. USA*, *70*(10), 2837–2839.

Brown, T. A., Cecconi, C., Tkachuk, A. N., Bustamante, C., & Clayton, D. A. (2005). Replication of mitochondrial DNA occurs by strand displacement with alternative light-strand origins, not via a strand-coupled mechanism. *Genes and Development*, *19*(20), 2466–2476.

Brown, W. M., George, M., & Wilson, A. C. (1979). Rapid evolution of animal mitochondrial DNA (primates/restriction endonuclease cleavage maps/gel electrophoresis/DNA melting). *Proc. Nat. Acad. Sci. Genetics*, *76*(4), 1967–1971.

Brown, W. M., Shine, J., & Goodman, H. M. (1978). Human mitochondrial DNA: Analysis of 7S DNA from the origin of replication (gel electrophoresis/restriction endonucleases/electron microscopy/hybridization/multiple components). *Proc. Natl. Acad. Sci. USA*, *75*(2), 735–739.

Brüser, C., Keller-Findeisen, J., & Jakobs, S. (2021). The TFAM-to-mtDNA ratio defines inner-cellular nucleoid populations with distinct activity levels. *Cell Reports*, *37*(8), 1–9.

Burr, S. P., Klimm, F., Glynos, A., Prater, M., Sendon, P., Nash, P., Powell, C. A., Simard, M.-L., Bonekamp, N. A., Charl, J., Diaz, H., Bozhilova, L. V., Nie, Y., Zhang, H., Frison, M., Falkenberg, M., Jones, N., Minczuk, M., Stewart, J. B., & Chinnery, P. F. (2023). Cell lineage-specific mitochondrial resilience during mammalian organogenesis. *Cell*, *186*, 1–18.

Cai, Y. C., Bullard, J. M., Thompson, N. L., & Spremulli, L. L. (2000). Interaction of mitochondrial elongation factor Tu with aminoacyl-tRNA and elongation factor Ts. *Journal of Biological Chemistry*, *275*(27), 20308–20314.

Cao, L., Shitara, H., Horii, T., Nagao, Y., Imai, H., Abe, K., Hara, T., Hayashi, J. I., & Yonekawa, H. (2007). The mitochondrial bottleneck occurs without reduction of mtDNA content in female mouse germ cells. *Nature Genetics*, *39*(3), 386–390.

Cao, L., Shitara, H., Sugimoto, M., Hayashi, J. I., Abe, K., & Yonekawa, H. (2009). New evidence confirms that the mitochondrial bottleneck is generated without reduction of mitochondrial DNA content in early primordial germ cells of mice. *PLoS Genetics*, *5*(12), 1–8.

Carling, P. J., Cree, L. M., & Chinnery, P. F. (2011). The implications of mitochondrial DNA copy number regulation during embryogenesis. *Mitochondrion*, *11*(5), 686–692.

Chang, D. D., & Clayton, D. A. (1986). Precise Assignment of the Light-Strand Promoter of Mouse Mitochondrial DNA: a Functional Promoter Consists of Multiple Upstream Domains. *Molecular and Cellular Biology*, *6*(9), 3253–3261.

Chen, H., Detmer, S. A., Ewald, A. J., Griffin, E. E., Fraser, S. E., & Chan, D. C. (2003). Mitofusins Mfn1 and Mfn2 coordinately regulate mitochondrial fusion and are essential for embryonic development. *Journal of Cell Biology*, *160*(2), 189–200.

Chen, X., Liang, D., Guo, J., Zhang, J., Sun, H., Zhang, X., Jin, J., Dai, Y., Bao, Q., Qian, X., Tan, L., Hu, P., Ling, X., Shen, B., & Xu, Z. (2022). DdCBE-mediated mitochondrial base editing in human 3PN embryos. *Cell Discovery*, *8*, 1–4.

Cho, S. I., Lee, S., Mok, Y. G., Lim, K., Lee, J., Lee, J. M., Chung, E., & Kim, J. S. (2022). Targeted A-to-G base editing in human mitochondrial DNA with programmable deaminases. *Cell*, *185*(10), 1764–1776.

Chomyn, A., Mariottini, P., Cleeter, M. W. J., Tagan, C. I., Matsuno-Yagi, A., Youssef, H., Doolittle, R. F., & Attardi, G. (1985). Six unidentified reading frames of human

mitochondrial DNA encode components of the respiratory-chain NADH dehydrogenase. *Nature*, *314*, 592–597.

Chomyn, A., Mariottini, P., Gonzalez-Cadavid, N., Attardi, G., Strongt, D. D., Trovatot, D., Rileyt, M., & Doolittleo, R. F. (1983). Identification of the polypeptides encoded in the ATPase 6 gene and in the unassigned reading frames 1 and 3 of human mtDNA (HeLa cells/synthetic peptides/antibodies/mitochondrial translation products). *Proc. Natl. Acad. Sci. USA*, *80*, 5535–5539.

Cipolat, S., Martins De Brito, O., Zilio, B. D., & Scorrano, L. (2004). *OPA1 requires mitofusin 1 to promote mitochondrial fusion. Proceedings of the National Academy of Sciences*, *101*(45), 15927–15932.

Connor, T. M., Hoer, S., Mallett, A., Gale, D. P., Gomez-Duran, A., Posse, V., Antrobus, R., Moreno, P., Sciacovelli, M., Frezza, C., Duff, J., Sheerin, N. S., Sayer, J. A., Ashcroft, M., Wiesener, M. S., Hudson, G., Gustafsson, C. M., Chinnery, P. F., & Maxwell, P. H. (2017). Mutations in mitochondrial DNA causing tubulointerstitial kidney disease. *PLoS Genetics*, *13*(3), 1–17.

Corneo, G., Zardi, L., & Polli, E. (1968). Human Mitochondrial DNA. *Journal of Molecular Biology*, *36*, 419–423.

Cornford, E., Varesi, J., Hyman, S., Damian, R., & Raleigh, M. (1997). Mitochondrial content of choroid plexus epithelium. *Exp Brain Res, 116*, 399–405.

Cottrell, D. A., Blakely, E. L., Johnson, M. A., Ince, P. G., Borthwick, G. M., & Turnbull, D. M. (2001). Cytochrome c oxidase deficient cells accumulate in the hippocampus and choroid plexus with age. *Neurobiology of Aging*, *22*(2), 265–272.

Cree, L. M., Samuels, D. C., De Sousa Lopes, S. C., Rajasimha, H. K., Wonnapinij, P., Mann, J. R., Dahl, H. H. M., & Chinnery, P. F. (2008). A reduction of mitochondrial DNA molecules during embryogenesis explains the rapid segregation of genotypes. *Nature Genetics*, *40*(2), 249–254.

Crick, F. H. C. (1966). Codon—anticodon pairing: The wobble hypothesis. *Journal of Molecular Biology*, *19*, 548–555.

de Stefani, D., Raffaello, A., Teardo, E., Szabó, I., & Rizzuto, R. (2011). A forty-kilodalton protein of the inner membrane is the mitochondrial calcium uniporter. *Nature*, *476*(7360), 336–340.

Diaz, F., Thomas, C. K., Garcia, S., Hernandez, D., & Moraes, C. T. (2005). Mice lacking COX10 in skeletal muscle recapitulate the phenotype of progressive mitochondrial myopathies associated with cytochrome c oxidase deficiency. *Human Molecular Genetics*, *14*(18), 2737–2748.

DiMauro, S. (2004). Mitochondrial diseases. *Biochimica et Biophysica Acta*, *1658*, 80–88.

Dogan, S. A., & Trifunovic, A. (2011). Modelling Mitochondrial Dysfunction in Mice Cologne Excellence Cluster on Cellular Stress Responses in Aging-Associated Diseases. *Physiol. Res*, *60*, 61–70.

Doimo, M., Pfeiffer, A., Wanrooij, P. H., & Wanrooij, S. (2020). mtDNA replication, maintenance, and nucleoid organization. In *The Human Mitochondrial Genome: From Basic Biology to Disease* (pp. 3–33). Elsevier.

D'Souza, A. R., & Minczuk, M. (2018). Mitochondrial transcription and translation: overview. *Essays in Biochemistry, 62*(3), 309–320.

Dunn, D. A., Cannon, M. V., Irwin, M. H., & Pinkert, C. A. (2012). Animal models of human mitochondrial DNA mutations. *Biochimica et Biophysica Acta, 1820*(5), 601–607.

Ekstrand, M. I., Falkenberg, M., Rantanen, A., Park, C. B., Gaspari, M., Hultenby, K., Rustin, P., Gustafsson, C. M., & Larsson, N. G. (2004). Mitochondrial transcription factor A regulates mtDNA copy number in mammals. *Human Molecular Genetics, 13*(9), 935–944.

Elliott, H. R., Samuels, D. C., Eden, J. A., Relton, C. L., & Chinnery, P. F. (2008). Pathogenic Mitochondrial DNA Mutations Are Common in the General Population. *American Journal of Human Genetics, 83*, 254–260.

Eme, L., Tamarit, D., Caceres, E. F., Stairs, C. W., De Anda, V., Schön, M. E., Seitz, K. W., Dombrowski, N., Lewis, W. H., Homa, F., Saw, J. H., Lombard, J., Nunoura, T., Li, W.-J., Hua, Z.-S., Chen, L.-X., Banfield, J. F., John, E. S., Reysenbach, A.-L., … Ettema, T. J. G. (2023). Inference and reconstruction of the heimdallarchaeial ancestry of eukaryotes. *Nature*, 1–13.

Falkenberg, M. (2018). Mitochondrial DNA replication in mammalian cells: Overview of the pathway. *Essays in Biochemistry, 62*(3), 287–296.

Falkenberg, M., & Gustafsson, C. M. (2020). Mammalian mitochondrial DNA replication and mechanisms of deletion formation. *Critical Reviews in Biochemistry and Molecular Biology, 55*(6), 509–524.

Falkenberg, M., Larsson, N. G., & Gustafsson, C. M. (2007). DNA replication and transcription in mammalian mitochondria. *Annual Review of Biochemistry*, 76, 679–699.

Fan, L., Wu, D., Goremykin, V., Xiao, J., Xu, Y., Garg, S., Zhang, C., Martin, W. F., & Zhu, R. (2020). Phylogenetic analyses with systematic taxon sampling show that mitochondria branch within Alphaproteobacteria. *Nature Ecology and Evolution, 4*, 1213–1219.

Fan, W., Waymire, K. G., Narula, N., Li, P., Rocher, C., Coskun, P. E., Vannan, M. A., Narula, J., MacGregor, G. R., & Wallace, D. C. (2008). A mouse model of mitochondrial disease reveals germline selection against severe mtDNA mutations. *Science, 319*(5865), 958–962.

Fan, Y.-Y., Davidson, L. A., Callaway, E. S., Wright, G. A., Safe, S., & Chapkin, R. S. (2015). A bioassay to measure energy metabolism in mouse colonic crypts, organoids, and sorted stem cells. *Am J Physiol Gastrointest Liver Physiol, 309*, G1–G9.

Farge, G., Pham, X. H., Holmlund, T., Khorostov, I., & Falkenberg, M. (2007). The accessory subunit B of DNA polymerase γ is required for mitochondrial replisome function. *Nucleic Acids Research, 35*(3), 902–911.

Filograna, R., Koolmeister, C., Upadhyay, M., Pajak, A., Clemente, P., Wibom, R., Simard, M. L., Wredenberg, A., Freyer, C., Stewart, J. B., & Larsson, N. G. (2019). Modulation of mtDNA copy number ameliorates the pathological consequences of a heteroplasmic mtDNA mutation in the mouse. *Sci. Adv.*, 5, 1–13.

Fine, A. S., Nemeth, C. L., Kaufman, M. L., & Fatemi, A. (2019). Mitochondrial aminoacyl-TRNA synthetase disorders: An emerging group of developmental disorders of myelination. *Journal of Neurodevelopmental Disorders*, 11, 1–15.

Finnilä, S., Tuisku, S., Herva, R., & Majamaa, K. (2001). A novel mitochondrial DNA mutation and a mutation in the Notch3 gene in a patient with myopathy and CADASIL. *Journal of Molecular Medicine*, 79, 641–647.

Floros, V. I., Pyle, A., DIetmann, S., Wei, W., Tang, W. W. C., Irie, N., Payne, B., Capalbo, A., Noli, L., Coxhead, J., Hudson, G., Crosier, M., Strahl, H., Khalaf, Y., Saitou, M., Ilic, D., Surani, M. A., & Chinnery, P. F. (2018). Segregation of mitochondrial DNA heteroplasmy through a developmental genetic bottleneck in human embryos. *Nature Cell Biology*, *20*(2), 144–151.

Fonseca, T. B., Sánchez-Guerrero, Á., Milosevic, I., & Raimundo, N. (2019). Mitochondrial fission requires DRP1 but not dynamins. *Nature*, 570, E34–E42.

Fontanesi, F., Tigano, M., Fu, Y., Sfeir, A., & Barrientos, A. (2020). Human mitochondrial transcription and translation. In *The Human Mitochondrial Genome: From Basic Biology to Disease* (pp. 35–70). Elsevier.

Freyer, C., Cree, L. M., Mourier, A., Stewart, J. B., Koolmeister, C., Milenkovic, D., Wai, T., Floros, V. I., Hagström, E., Chatzidaki, E. E., Wiesner, R. J., Samuels, D. C., Larsson, N. G., & Chinnery, P. F. (2012). Variation in germline mtDNA heteroplasmy is determined prenatally but modified during subsequent transmission. *Nature Genetics*, *44*(11), 1282–1285.

Fritz, S., Rapaport, D., Klanner, E., Neupert, W., & Westermann, B. (2001). Connection of the Mitochondrial Outer and Inner Membranes by Fzo1 Is Critical for Organellar Fusion. *The Journal of Cell Biology*, *152*(4), 683–692.

Gabaldón, T. (2021). Origin and Early Evolution of the Eukaryotic Cell. *Annual Review of Microbiology*, *75*, 631–647.

Gammage, P. A., Rorbach, J., Vincent, A. I., Rebar, E. J., & Minczuk, M. (2014). Mitochondrially targeted ZFNs for selective degradation of pathogenic mitochondrial genomes bearing large-scale deletions or point mutations. *EMBO Molecular Medicine*, *6*(4), 458–466.

Gammage, P. A., Viscomi, C., Simard, M. L., Costa, A. S. H., Gaude, E., Powell, C. A., Van Haute, L., McCann, B. J., Rebelo-Guiomar, P., Cerutti, R., Zhang, L., Rebar, E. J., Zeviani, M., Frezza, C., Stewart, J. B., & Minczuk, M. (2018). Genome editing in mitochondria corrects a pathogenic mtDNA mutation in vivo. *Nature Medicine, 24*(11), 1691–1695.

Gaspari, M., Falkenberg, M., Larsson, N. G., & Gustafsson, C. M. (2004). The mitochondrial RNA polymerase contributes critically to promoter specificity in mammalian cells. *EMBO Journal*, *23*(23), 4606–4614.

Giegé, R., & Eriani, G. (2023). The tRNA identity landscape for aminoacylation and beyond. *Nucleic Acids Research*, *51*(4), 1528–1570.

Greaves, L. C., Barron, M. J., Campbell-Shiel, G., Kirkwood, T. B. L., & Turnbull, D. M. (2011). Differences in the accumulation of mitochondrial defects with age in mice and humans. *Mechanisms of Ageing and Development*, *132*(11–12), 588–591.

Gorman, G. S., Chinnery, P. F., DiMauro, S., Hirano, M., Koga, Y., McFarland, R., Suomalainen, A., Thorburn, D. R., Zeviani, M., & Turnbull, D. M. (2016). Mitochondrial diseases. *Nature Reviews Disease Primers*, *2*, 1–22.

Gorman, G. S., Schaefer, A. M., Ng, Y., Gomez, N., Blakely, E. L., Alston, C. L., Feeney, C., Horvath, R., Yu-Wai-Man, P., Chinnery, P. F., Taylor, R. W., Turnbull, D. M., & McFarland, R. (2015). Prevalence of nuclear and mitochondrial DNA mutations related to adult mitochondrial disease. *Annals of Neurology*, *77*(5), 753–759.

Grady, J. P., Pickett, S. J., Ng, Y. S., Alston, C. L., Blakely, E. L., Hardy, S. A., Feeney, C. L., Bright, A. A., Schaefer, A. M., Gorman, G. S., McNally, R. J., Taylor, R. W., Turnbull, D. M., & McFarland, R. (2018). mtDNA heteroplasmy level and copy number indicate disease burden in m.3243A>G mitochondrial disease. *EMBO Molecular Medicine*, *10*, 1–13.

Gray, H., & Wong, T. W. (1992). Purification and identification of subunit structure of the human mitochondrial DNA polymerase. *Journal of Biological Chemistry*, *267*(9), 5835–5841.

Gray, M. W. (2012). Mitochondrial evolution. *Cold Spring Harbor Perspectives in Biology*, *4*(9), 1–16.

Gray, M. W. (2015). Mosaic nature of the mitochondrial proteome: Implications for the origin and evolution of mitochondria. *Proceedings of the National Academy of Sciences of the United States of America*, *112*(33), 10133–10138.

Gray, M. W., Burger, C., & Lang, F. B. (1999). Mitochondrial Evolution. *Science*, *283*, 1476–1481.

Guerbette, T., Boudry, G., & Lan, A. (2022). Mitochondrial function in intestinal epithelium homeostasis and modulation in diet-induced obesity. *Molecular Metabolism*, *63*, 1–18.

Guo, J., Chen, X., Liu, Z., Sun, H., Zhou, Y., Dai, Y., Ma, Y., He, L., Qian, X., Wang, J., Zhang, J., Zhu, Y., Zhang, J., Shen, B., & Zhou, F. (2022). DdCBE mediates efficient and inheritable modifications in mouse mitochondrial genome. *Molecular Therapy - Nucleic Acids*, *27*, 73–80.

Guo, J., Zhang, X., Chen, X., Sun, H., Dai, Y., Wang, J., Qian, X., Tan, L., Lou, X., & Shen, B. (2021). Precision modeling of mitochondrial diseases in zebrafish via DdCBE-mediated mtDNA base editing. *Cell Discovery*, 7, 1–5.

Gustafsson, C. M., Falkenberg, M., & Larsson, N. G. (2016). Maintenance and Expression of Mammalian Mitochondrial DNA. *Annual Review of Biochemistry*, *85*, 133–160.

Hällberg, B. M., & Larsson, N. G. (2014). Making proteins in the powerhouse. *Cell Metabolism*, *20*, 226–240.

Handy, D. E., & Loscalzo, J. (2012). Redox regulation of mitochondrial function. *Antioxidants and Redox Signaling*, *16*(11), 1323–1367.

Hauswirth, W. W., & Laipist, P. J. (1982). Mitochondrial DNA polymorphism in a maternal lineage of Holstein cows (nucleotide sequence/cytoplasmic inheritance/silent mutation). *Proc. Natl. Acad. Sci. Genetics*, *79*, 4686–4690.

Hillen, H. S., Morozov, Y. I., Sarfallah, A., Temiakov, D., & Cramer, P. (2017). Structural Basis of Mitochondrial Transcription Initiation. *Cell*, *171*, 1072–1081.

Hixson, J. E., & Clayton, D. A. (1985). Initiation of transcription from each of the two human mitochondrial promoters requires unique nucleotides at the transcriptional start sites (displacement loop/mutagenesis/regulatory sequences/template signals). *Proc. Natl. Acad. Sci. Biochemistry*, *82*, 2660–2664.

Holmes, J. B., Akman, G., Wood, S. R., Sakhuja, K., Cerritelli, S. M., Moss, C., Bowmaker, M. R., Jacobs, H. T., Crouch, R. J., & Holt, I. J. (2015). Primer retention owing to the absence of RNase H1 is catastrophic for mitochondrial DNA replication. *Proceedings of the National Academy of Sciences*, *112*(30), 9334–9339.

Holt, I. J., Harding, A. E., & Morgan-Hughes, J. A. (1988). Deletions of muscle mitochondrial DNA in patients with mitochondrial myopathies. *Nature*, *331*, 717–719.

Holt, I. J., Lorimer, H. E., & Jacobs, H. T. (2000). Coupled Leading-and Lagging-Strand Synthesis of Mammalian Mitochondrial DNA eubacteria. Replication of the H strand on this model is proposed to initiate at a single site (O H), and to proceed unidirectionally until two-thirds of the way around the These replication intermediates were compared with. *Cell*, *100*, 515–524.

Huang, L.-K., & Wang, M.-J. J. (1995). Image Thresholding by Minimizing the Measures of Fuzziness. *Pattern Recognition*, *28*(1), 41–51.

Hudson, G., Gomez-Duran, A., Wilson, I. J., & Chinnery, P. F. (2014). Recent Mitochondrial DNA Mutations Increase the Risk of Developing Common Late-Onset Human Diseases. *PLoS Genetics*, *10*(5), 1–9.

Huot, J. L., Shikha, S., & Schneider, A. (2019). Inducible orthogonal aminoacylation demonstrates that charging is required for mitochondrial tRNA import in Trypanosoma brucei. *Scientific Reports*, *9*(1), 1–8.

Imachi, H., Nobu, M. K., Nakahara, N., Morono, Y., Ogawara, M., Takaki, Y., Takano, Y., Uematsu, K., Ikuta, T., Ito, M., Matsui, Y., Miyazaki, M., Murata, K., Saito, Y., Sakai, S., Song, C., Tasumi, E., Yamanaka, Y., Yamaguchi, T., … Takai, K. (2020). Isolation of an archaeon at the prokaryote–eukaryote interface. *Nature*, *577*(7791), 519–525.

Inoue, K., Nakada, K., Ogura, A., Isobe, K., Goto, Y.-I., Nonaka, I., & Hayashi, J.-I. (2000). Generation of mice with mitochondrial dysfunction by introducing mouse mtDNA carrying a deletion into zygotes. *Nature Genetics*, *26*, 176–181.

Itsara, L. S., Kennedy, S. R., Fox, E. J., Yu, S., Hewitt, J. J., Sanchez-Contreras, M., Cardozo-Pelaez, F., & Pallanck, L. J. (2014). Oxidative Stress Is Not a Major Contributor to Somatic Mitochondrial DNA Mutations. *PLoS Genetics*, *10*(2), 1–13.

Jackson, C. B., Turnbull, D. M., Minczuk, M., & Gammage, P. A. (2020). Therapeutic Manipulation of mtDNA Heteroplasmy: A Shifting Perspective. *Trends in Molecular Medicine*, *26*(7), 698–709.

Jastroch, M., Divakaruni, A. S., Mookerjee, S., Treberg, J. R., & Brand, M. D. (2010). Mitochondrial proton and electron leaks. *Essays in Biochemistry*, *47*, 53–67.

Johnson, S. C., Kayser, E. B., Bornstein, R., Stokes, J., Bitto, A., Park, K. Y., Pan, A., Sun, G., Raftery, D., Kaeberlein, M., Sedensky, M. M., & Morgan, P. G. (2020). Regional metabolic signatures in the Ndufs4(KO) mouse brain implicate defective glutamate/α-ketoglutarate metabolism in mitochondrial disease. *Molecular Genetics and Metabolism*, *130*(2), 118–132.

Jornayvaz, F. R., & Shulman, G. I. (2010). Regulation of mitochondrial biogenesis. *Essays in Biochemistry*, *47*, 69–84.

Kauppila, J. H. K., Baines, H. L., Bratic, A., Simard, M. L., Freyer, C., Mourier, A., Stamp, C., Filograna, R., Larsson, N. G., Greaves, L. C., & Stewart, J. B. (2016). A Phenotype-Driven Approach to Generate Mouse Models with Pathogenic mtDNA Mutations Causing Mitochondrial Disease. *Cell Reports*, *16*(11), 2980–2990.

Kauppila, J. H. K., Bonekamp, N. A., Mourier, A., Isokallio, M. A., Just, A., Kauppila, T. E. S., Stewart, J. B., & Larsson, N. G. (2018). Base-excision repair deficiency alone or combined with increased oxidative stress does not increase mtDNA point mutations in mice. *Nucleic Acids Research*, *46*(13), 6642–6669.

Kauppila, J. H. K., & Stewart, J. B. (2015). Mitochondrial DNA: Radically free of free-radical driven mutations. *Biochimica et Biophysica Acta - Bioenergetics*, *1847*, 1354–1361.

Kennedy, S. R., Salk, J. J., Schmitt, M. W., & Loeb, L. A. (2013). Ultra-Sensitive Sequencing Reveals an Age-Related Increase in Somatic Mitochondrial Mutations That Are Inconsistent with Oxidative Damage. *PLoS Genetics*, *9*(9), 1–10.

Koonin, E. v. (2010). Eukaryotes. *Genome Biology*, *11*(209), 1–12.

Korhonen, J. A., Gaspari, M., & Falkenberg, M. (2003). TWINKLE has $5' \rightarrow 3'$ DNA helicase activity and is specifically stimulated by mitochondrial single-stranded DNA-binding protein. *Journal of Biological Chemistry*, *278*(49), 48627–48632.

Koripella, R. K., Sharma, M. R., Haque, M. E., Risteff, P., Spremulli, L. L., & Agrawal, R. K. (2019). Structure of Human Mitochondrial Translation Initiation Factor 3 Bound to the Small Ribosomal Subunit. *iScience*, *12*, 76–86.

Krüger, A., Remes, C., Shiriaev, D. I., Liu, Y., Spåhr, H., Wibom, R., Atanassov, I., Nguyen, M. D., Cooperman, B. S., & Rorbach, J. (2023). Human mitochondria require mtRF1 for translation termination at non-canonical stop codons. *Nature Communications*, *14*, 1–16.

Kruse, B., Narasimhan, N., & Attardi, G. (1989). Termination of Transcription in Human Mitochondria: Identification and Purification of a DNA Binding Protein Factor That Promotes Termination. *Cell*, *58*, 391–397.

Kruse, S. E., Watt, W. C., Marcinek, D. J., Kapur, R. P., Schenkman, K. A., & Palmiter, R. D. (2008). Mice with Mitochondrial Complex I Deficiency Develop a Fatal Encephalomyopathy. *Cell Metabolism*, *7*(4), 312–320.

Kukat, C., Davies, K. M., Wurm, C. A., Spåhr, H., Bonekamp, N. A., Kühl, I., Joos, F., Polosa, P. L., Park, C. B., Posse, V., Falkenberg, M., Jakobs, S., Kühlbrandt, W., & Larsson, N. G. (2015). Cross-strand binding of TFAM to a single mtDNA molecule forms the mitochondrial nucleoid. *Proceedings of the National Academy of Sciences*, *112*(36), 11288–11293.

Kukat, C., Wurm, C. A., Spåhr, H., Falkenberg, M., Larsson, N. G., & Jakobs, S. (2011). Super-resolution microscopy reveals that mammalian mitochondrial nucleoids have a uniform size and frequently contain a single copy of mtDNA. *Proceedings of the National Academy of Sciences*, *108*(33), 13534–13539.

Kummer, E., & Ban, N. (2021). Mechanisms and regulation of protein synthesis in mitochondria. *Nature Reviews Molecular Cell Biology*, *22*(5), pp. 307–325.

Kummer, E., Leibundgut, M., Rackham, O., Lee, R. G., Boehringer, D., Filipovska, A., & Ban, N. (2018). Unique features of mammalian mitochondrial translation initiation revealed by cryo-EM. *Nature*, *560*(7717), 263–267.

Laipis, P. J., van de Wallet, M. J., & Hauswirth, W. W. (1988). Unequal partitioning of bovine mitochondrial genotypes among siblings (maternal inheritance/heteroplasmy/mitochondrial DNA/sequence polymorphism). *Proc. Natl. Acad. Sci. Genetics*, *85*, 8107–8110.

Lakshmipathy, U., & Campbell, C. (2001). Antisense-mediated decrease in DNA ligase III expression results in reduced mitochondrial DNA integrity. *Nucleic Acids Research*, *29*(3), 668–676.

Larsson, N.-G., Wang, J., Wilhelmsson, H., Oldfors, A., Rustin, P., Lewandoski, M., Barsh, G. S., & Clayton, D. A. (1998). Mitochondrial transcription factor A is necessary for mtDNA maintenance and embryogenesis in mice. *Nature Genetics*, *18*, 231–236.

Latorre-Pellicer, A., Lechuga-Vieco, A. V., Johnston, I. G., Hämäläinen, R. H., Pellico, J., Justo-Méndez, R., Fernández-Toro, J. M., Clavería, C., Guaras, A., Sierra, R., Llop, J., Torres, M., Criado, L. M., Suomalainen, A., Jones, N. S., Ruíz-Cabello, J., & Enríquez, J. A. (2019). Regulation of Mother-to-Offspring Transmission of mtDNA Heteroplasmy. *Cell Metabolism*, *30*(6), 1120–1130.

Lavdovskaia, E., Denks, K., Nadler, F., Steube, E., Linden, A., Urlaub, H., Rodnina, M. v., & Richter-Dennerlein, R. (2020). Dual function of GTPBP6 in biogenesis and recycling of human mitochondrial ribosomes. *Nucleic Acids Research*, *48*(22), 12929–12942.

Lee, H., Lee, S., Baek, G., Kim, A., Kang, B. C., Seo, H., & Kim, J. S. (2021). Mitochondrial DNA editing in mice with DddA-TALE fusion deaminases. *Nature Communications*, *12*(1), 1–6.

Lehmann, D., Schubert, K., Joshi, P. R., Hardy, S. A., Tuppen, H. A. L., Baty, K., Blakely, E. L., Bamberg, C., Zierz, S., Deschauer, M., & Taylor, R. W. (2015). Pathogenic mitochondrial mt-tRNA Ala variants are uniquely associated with isolated myopathy. *European Journal of Human Genetics*, *23*, 1735–1738.

Letts, J. A., & Sazanov, L. A. (2017). Clarifying the supercomplex: The higher-order organization of the mitochondrial electron transport chain. *Nature Structural and Molecular Biology*, 24(10), 800–808.

Li, X., Franz, T., Atanassov, I., & Colby, T. (2021). Step-by-Step Sample Preparation of Proteins for Mass Spectrometric Analysis. In *Methods in Molecular Biology* (Vol. 2261, pp. 13–23). Humana Press Inc.

Lill, R., Hoffmann, B., Molik, S., Pierik, A. J., Rietzschel, N., Stehling, O., Uzarska, M. A., Webert, H., Wilbrecht, C., & Mühlenhoff, U. (2012). The role of mitochondria in cellular iron-sulfur protein biogenesis and iron metabolism. *Biochimica et Biophysica Acta - Molecular Cell Research*, 1823(9), 1491–1508.

Lim, K., Cho, S. I., & Kim, J. S. (2022). Nuclear and mitochondrial DNA editing in human cells with zinc finger deaminases. *Nature Communications*, *13*, 1–10.

Lind, C., Sund, J., & Åqvist, J. (2013). Codon-reading specificities of mitochondrial release factors and translation termination at non-standard stop codons. *Nature Communications*, *4*, 1–8.

López-García, P., & Moreira, D. (2006). Selective forces for the origin of the eukaryotic nucleus. *BioEssays*, *28*(5), 525–533.

López-García, P., & Moreira, D. (2020). The Syntrophy hypothesis for the origin of eukaryotes revisited. *Nature Microbiology*, *5*(5), 655–667.

Lun, M. P., Monuki, E. S., & Lehtinen, M. K. (2015). Development and functions of the choroid plexus-cerebrospinal fluid system. *Nature Reviews Neuroscience*, *16*, 445–457.

Macken, W. L., Lucassen, A. M., Hanna, M. G., & Pitceathly, R. D. S. (2021). Mitochondrial DNA variants in genomic data: diagnostic uplifts and predictive implications. *Nature Reviews Genetics*, *22*, 547–548

Macken, W. L., Vandrovcova, J., Hanna, M. G., & Pitceathly, R. D. S. (2021). Applying genomic and transcriptomic advances to mitochondrial medicine. *Nature Reviews Neurology*, 17(4), 215–230.

Marchi, S., Guilbaud, E., Tait, S. W. G., Yamazaki, T., & Galluzzi, L. (2022). Mitochondrial control of inflammation. *Nature Reviews Immunology*, *23*, 159–173.

Marchington, D. R., Barlow, D., & Poulton, J. (1999). Transmitochondrial mice carrying resistance to chloramphenicol on mitochondrial DNA: Developing the first mouse model of mitochondrial DNA disease. *Nature Medicine*, *5*(8), 957–960.

Mariottini, P., Chomyn, A., Rileyt, M., Cottrello, B., Doolittlet, R. F., & Attardi, G. (1986). Identification of the polypeptides encoded in the unassigned reading frames 2, 4, 4L, and 5 of human mitochondrial DNA (HeLa cells/synthetic peptides/antibodies/mitochondrial translation products). *Proc. Natl. Acad. Sci. Biochemistry*, *83*, 1563–1567.

Martijn, J., Vosseberg, J., Guy, L., Offre, P., & Ettema, T. J. G. (2018). Deep mitochondrial origin outside the sampled alphaproteobacteria. *Nature*, *557*(7703), 101–105.

Martin, W. F., Garg, S., & Zimorski, V. (2015). Endosymbiotic theories for eukaryote origin. *Philosophical Transactions of the Royal Society B: Biological Sciences*, *370*, 1–18.

Martin, W. F., Roettger, M., Ku, C., Garg, S. G., Nelson-Sathi, S., & Landan, G. (2017). Late mitochondrial origin is an artifact. *Genome Biology and Evolution*, *9*(2), 373–379.

Martin, W., & Müller, M. (1998). The hydrogen hypothesis for the first eukaryote. *Nature*, *392*, 37–41.

Martínez-Reyes, I., & Chandel, N. S. (2020). Mitochondrial TCA cycle metabolites control physiology and disease. *Nature Communications*, *11*, 1–11.

Mavraki, E., Labrum, R., Sergeant, K., Alston, C. L., Woodward, C., Smith, C., Knowles, C. V. Y., Patel, Y., Hodsdon, P., Baines, J. P., Blakely, E. L., Polke, J., Taylor, R. W., & Fratter, C. (2022). Genetic testing for mitochondrial disease: the United Kingdom best practice guidelines. *European Journal of Human Genetics*, *31*, 148–163.

McFarland, R., Swalwell, H., Blakely, E. L., He, L., Groen, E. J., Turnbull, D. M., Bushby, K. M., & Taylor, R. W. (2008). The m.5650G > A mitochondrial tRNAAla mutation is pathogenic and causes a phenotype of pure myopathy. *Neuromuscular Disorders*, *18*, 63–67.

Meeusen, S., DeVay, R., Block, J., Cassidy-Stone, A., Wayson, S., McCaffery, J. M., & Nunnari, J. (2006). Mitochondrial Inner-Membrane Fusion and Crista Maintenance Requires the Dynamin-Related GTPase Mgm1. *Cell*, *127*(2), 383–395.

Mi, L., Shi, M., Li, Y. X., Xie, G., Rao, X., Wu, D., Cheng, A., Niu, M., Xu, F., Yu, Y., Gao, N., Wei, W., Wang, X., & Wang, Y. (2023). DddA homolog search and engineering expand sequence compatibility of mitochondrial base editing. *Nature Communications*, *14*, 1–9.

Miralles Fusté, J., Shi, Y., Wanrooij, S., Zhu, X., Jemt, E., Persson, Ö., Sabouri, N., Gustafsson, C. M., & Falkenberg, M. (2014). *In Vivo* Occupancy of Mitochondrial Single-Stranded DNA Binding Protein Supports the Strand Displacement Mode of DNA Replication. *PLoS Genetics*, *10*(12), 1–11.

Mitchell, P. (1961). Coupling of Phosphorylation to Electron and Hydrogen Transfer by a Chemi-osmotic Type of Mechanism. *Nature*, *191*, 144–148.

Mok, B. Y., de Moraes, M. H., Zeng, J., Bosch, D. E., Kotrys, A. V., Raguram, A., Hsu, F. S., Radey, M. C., Peterson, S. B., Mootha, V. K., Mougous, J. D., & Liu, D. R. (2020). A bacterial cytidine deaminase toxin enables CRISPR-free mitochondrial base editing. *Nature*, *583*, 631–637.

Mok, B. Y., Kotrys, A. V., Raguram, A., Huang, T. P., Mootha, V. K., & Liu, D. R. (2022). CRISPR-free base editors with enhanced activity and expanded targeting scope in mitochondrial and nuclear DNA. *Nature Biotechnology*, *40*, 1378–1387.

Montoya, J., Christiansont, T., Levenst, D., Rabinowitzt, M., & Attardi, G. (1982). Identification of initiation sites for heavy-strand and light-strand transcription in human mitochondrial DNA [*in vitro* capped RNA/poly(A)-containing RNA/mitochondrial DNA transcription complexes/SI endonuclease]. *Proc. Natl. Acad. Sci. Biochemistry*, *79*, 7195–7199.

Montoya, J., Gaines, G. L., & Attardi, G. (1983). The Pattern of Transcription of the Human Mitochondrial rRNA Genes Reveals Two Overlapping Transcription Units. *Cell*, *34*, 151–159.

Montoya, J., Ojala, D., & Attardi, G. (1981). Distinctive features of the 5'-terminal sequences of the human mitochondrial mRNAs. *Nature*, *290*(9), 465–470.

Muñoz-Gómez, S. A., Susko, E., Williamson, K., Eme, L., Slamovits, C. H., Moreira, D., López-García, P., & Roger, A. J. (2022). Site-and-branch-heterogeneous analyses of an expanded dataset favour mitochondria as sister to known Alphaproteobacteria. *Nature Ecology and Evolution*, *6*(3), 253–262.

Murgia, M., Tan, J., Geyer, P. E., Doll, S., Mann, M., & Klopstock, T. (2019). Proteomics of Cytochrome c Oxidase-Negative versus -Positive Muscle Fiber Sections in Mitochondrial Myopathy. *Cell Reports*, *29*, 3825–3834.

Naganuma, M., Sekine, S. I., Chong, Y. E., Guo, M., Yang, X. L., Gamper, H., Hou, Y. M., Schimmel, P., & Yokoyama, S. (2014). The selective tRNA aminoacylation mechanism based on a single G.U pair. *Nature*, *510*(7506), 507–511.

Naganuma, M., Sekine, S.-I., Fukunaga, R., Yokoyama, S., & Riken, B. (2009). Unique protein architecture of alanyl-tRNA synthetase for aminoacylation, editing, and dimerization. *Proceedings of the National Academy of Sciences*, *106*(21), 8489–8494.

Nagao, A., Suzuki, T., Katoh, T., Sakaguchi, Y., & Suzuki, T. (2009). Biogenesis of glutaminyl-mt tRNA Gln in human mitochondria. *Proceedings of the National Academy of Sciences*, *106*(38), 16209–16214.

Nam, S.-C., & Changwon, K. (2005). DNA Light-strand Preferential Recognition of Human Mitochondria Transcription Termination Factor mTERF . *Journal of Biochemistry and Molecular Biology*, *38*(6), 690–694.

Nicholls, T. J., Nadalutti, C. A., Motori, E., Sommerville, E. W., Gorman, G. S., Basu, S., Hoberg, E., Turnbull, D. M., Chinnery, P. F., Larsson, N. G., Larsson, E., Falkenberg,

M., Taylor, R. W., Griffith, J. D., & Gustafsson, C. M. (2018). Topoisomerase 3α Is Required for Decatenation and Segregation of Human mtDNA. *Molecular Cell*, *69,* 9–23.

Ojala, D., Montoya, J., & Attardi, G. (1981). tRNA punctuation model of RNA processing in human mitochondria. *Nature*, *290*, 470–474.

Old, S. L., & Johnson, M. A. (1989). Methods of microphotometric assay of succinate dehydrogenase and cytochrome c oxidase activities for use on human skeletal muscle. *Histochemical Journal*, *21*, 545–555.

Olesen, M. A., Torres, A. K., Jara, C., Murphy, M. P., & Tapia-Rojas, C. (2020). Premature synaptic mitochondrial dysfunction in the hippocampus during aging contributes to memory loss. *Redox Biology*, *34*, 1–17.

Olivo, P. D., van de Walle, M. J., Laipis, P. J., & Hauswirth, W. W. (1983). Nucleotide sequence evidence for rapid genotypic shifts in the bovine mitochondrial DNA D-loop. *Nature*, *306*, 400–402.

Orellana, E. A., Siegal, E., & Gregory, R. I. (2022). tRNA dysregulation and disease. *Nature Reviews Genetics*, *23*, 651–664.

Osawa, S., Ohama, T., Jukes, T. H., & Watanabe, K. (1989). Evolution of the Mitochondrial Genetic Code I. Origin of AGR Serine and Stop Codons in Metazoan Mitochondria. *J Mol Evol*, *29*, 202–207.

Ott, M., Amunts, A., & Brown, A. (2016). Organization and Regulation of Mitochondrial Protein Synthesis. *Annual Review of Biochemistry, 85*, 77–101.

Peterson, L. W., & Artis, D. (2014). Intestinal epithelial cells: Regulators of barrier function and immune homeostasis. *Nature Reviews Immunology*, *14*, 141–153.

Pfanner, N., Warscheid, B., & Wiedemann, N. (2019). Mitochondrial proteins: from biogenesis to functional networks. *Nature Reviews Molecular Cell Biology*, *20*(5), 267–284.

Pfeffer, G., Horvath, R., Klopstock, T., Mootha, V. K., Suomalainen, A., Koene, S., Hirano, M., Zeviani, M., Bindoff, L. A., Yu-Wai-Man, P., Hanna, M., Carelli, V., Mcfarland, R., Majamaa, K., Turnbull, D. M., Smeitink, J., & Chinnery, P. F. (2013). New treatments for mitochondrial disease - No time to drop our standards. *Nature Reviews Neurology*, *9*(8), 474–481.

Posse, V., & Gustafsson, C. M. (2017). Human mitochondrial transcription factor B2 is required for promoter melting during initiation of transcription. *Journal of Biological Chemistry*, *292*(7), 2637–2645.

Posse, V., Hoberg, E., Dierckx, A., Shahzad, S., Koolmeister, C., Larsson, N. G., Wilhelmsson, L. M., Hällberg, B. M., & Gustafsson, C. M. (2014). The amino terminal extension of mammalian mitochondrial RNA polymerase ensures promoter specific transcription initiation. *Nucleic Acids Research*, *42*(6), 3638–3647.

Rackham, O., & Filipovska, A. (2022). Organization and expression of the mammalian mitochondrial genome. *Nature Reviews Genetics*, 23(10), 606–623.

Reyes, A., Kazak, L., Wood, S. R., Yasukawa, T., Jacobs, H. T., & Holt, I. J. (2013). Mitochondrial DNA replication proceeds via a "bootlace" mechanism involving the incorporation of processed transcripts. *Nucleic Acids Research*, *41*(11), 5837–5850.

Ritchie, M. E., Phipson, B., Wu, D., Hu, Y., Law, C. W., Shi, W., & Smyth, G. K. (2015). Limma powers differential expression analyses for RNA-sequencing and microarray studies. *Nucleic Acids Research*, *43*(7), 1–13.

Rodríguez-Colman, M. J., Schewe, M., Meerlo, M., Stigter, E., Gerrits, J., Pras-Raves, M., Sacchetti, A., Hornsveld, M., Oost, K. C., Snippert, H. J., Verhoeven-Duif, N., Fodde, R., & Burgering, B. M. T. (2017). Interplay between metabolic identities in the intestinal crypt supports stem cell function. *Nature*, *543*, 424–427.

Roger, A. J., Muñoz-Gómez, S. A., & Kamikawa, R. (2017). The Origin and Diversification of Mitochondria. *Current Biology*, 27(21), R1177–R1192.

Rorbach, J., & Minczuk, M. (2012). The post-transcriptional life of mammalian mitochondrial RNA. *Biochemical Journal*, *444*(3), 357–373.

Rorbach, J., Richter, R., Wessels, H. J., Wydro, M., Pekalski, M., Farhoud, M., Kühl, I., Gaisne, M., Bonnefoy, N., Smeitink, J. A., Lightowlers, R. N., & Chrzanowska-Lightowlers, Z. M. A. (2008). The human mitochondrial ribosome recycling factor is essential for cell viability. *Nucleic Acids Research*, *36*(18), 5787–5799.

Ross, J. M. (2011). Visualization of mitochondrial respiratory function using cytochrome C oxidase/succinate dehydrogenase (COX/SDH) double-labeling histochemistry. *Journal of Visualized Experiments*, *57*, 1–6.

Ross, J. M., Stewart, J. B., Hagström, E., Brené, S., Mourier, A., Coppotelli, G., Freyer, C., Lagouge, M., Hoffer, B. J., Olson, L., & Larsson, N. G. (2013). Germline mitochondrial DNA mutations aggravate ageing and can impair brain development. *Nature*, *501*(7467), 412–415.

Rossi, A., Pizzo, P., & Filadi, R. (2019). Calcium, mitochondria and cell metabolism: A functional triangle in bioenergetics. *Biochimica et Biophysica Acta - Molecular Cell Research*, *1866*(7), 1068–1078.

Rubio-Cosials, A., Sidow, J. F., Jiménez-Menéndez, N., Fernández-Millán, P., Montoya, J., Jacobs, H. T., Coll, M., Bernadó, P., & Solà, M. (2011). Human mitochondrial transcription factor A induces a U-turn structure in the light strand promoter. *Nature Structural and Molecular Biology*, *18*(11), 1281–1289.

Ruzzenente, B., Rötig, A., & Metodiev, M. D. (2016). Mouse models for mitochondrial diseases. *Human Molecular Genetics*, 25(R2), R115–R122.

Sabharwal, A., Kar, B., Restrepo-Castillo, S., Holmberg, S. R., Mathew, N. D., Kendall, B. L., Cotter, R. P., Warejoncas, Z., Seiler, C., Nakamaru-Ogiso, E., Clark, K. J., & Ekker, S. C. (2021). The FusX TALE Base Editor (FusXTBE) for Rapid Mitochondrial DNA

Programming of Human Cells in Vitro and Zebrafish Disease Models in Vivo. *CRISPR Journal*, *4*(6), 799–821.

Sanchez-Contreras, M., Sweetwyne, M. T., Tsantilas, K. A., Whitson, J. A., Campbell, M. D., Kohrn, B. F., Kim, H. J., Hipp, M. J., Fredrickson, J., Nguyen, M. M., Hurley, J. B., Marcinek, D. J., Rabinovitch, P. S., & Kennedy, S. R. (2023). The multi-tissue landscape of somatic mtDNA mutations indicates tissue-specific accumulation and removal in aging. *ELife*, 1–26.

Schägger, H., & Pfeiffer, K. (2000). Schägger and Pfeiffer, 2000. *The EMBO Journal*, *19*(8), 1777–1783.

Schindelin, J., Arganda-Carreras, I., Frise, E., Kaynig, V., Longair, M., Pietzsch, T., Preibisch, S., Rueden, C., Saalfeld, S., Schmid, B., Tinevez, J. Y., White, D. J., Hartenstein, V., Eliceiri, K., Tomancak, P., & Cardona, A. (2012). Fiji: An open-source platform for biological-image analysis. *Nature Methods*, *9*(7), 676–682.

Schwartzbach, C. J., & Spremulli, L. L. (1989). Bovine Mitochondrial Protein Synthesis Elongation Factors: Identification and initial characterization of an elongation factor Tu-elongation factor Ts complex*. *The Journal of Biological Chemistry*, *264*(32), 19125–19131.

Searcy, D. G. (2003). Metabolic integration during the evolutionary origin of mitochondria. *Cell Research*, *13*(4), 229–238.

Shutt, T. E., & Gray, M. W. (2006). Bacteriophage origins of mitochondrial replication and transcription proteins. *Trends in Genetics*, *22*(2), 90–95.

Signes, A., & Fernandez-Vizarra, E. (2018). Assembly of mammalian oxidative phosphorylation complexes I–V and supercomplexes. *Essays in Biochemistry*, *62*, 255–270.

Silva-Pinheiro, P., & Minczuk, M. (2022). The potential of mitochondrial genome engineering. *Nature Reviews Genetics*, *23*(4), 199–214.

Silva-Pinheiro, P., Mutti, C. D., Van Haute, L., Powell, C. A., Nash, P. A., Turner, K., & Minczuk, M. (2023). A library of base editors for the precise ablation of all protein-coding genes in the mouse mitochondrial genome. *Nature Biomedical Engineering*, *7*, 692–703.

Simard, M. L., Mourier, A., Greaves, L. C., Taylor, R. W., & Stewart, J. B. (2018). A novel histochemistry assay to assess and quantify focal cytochrome c oxidase deficiency. *Journal of Pathology*, *245*(3), 311–323.

Sissler, M., González-Serrano, L. E., & Westhof, E. (2017). Recent Advances in Mitochondrial Aminoacyl-tRNA Synthetases and Disease. *Trends in Molecular Medicine*, *23*(8), 693–708.

Soleimanpour-Lichaei, H. R., Kühl, I., Gaisne, M., Passos, J. F., Wydro, M., Rorbach, J., Temperley, R., Bonnefoy, N., Tate, W., Lightowlers, R., & Chrzanowska-Lightowlers, Z. (2007). mtRF1a Is a Human Mitochondrial Translation Release Factor Decoding the Major Termination Codons UAA and UAG. *Molecular Cell*, *27*(5), 745–757.

Sonney, S., Leipzig, J., Lott, M. T., Zhang, S., Procaccio, V., Wallace, D. C., & Sondheimer, N. (2017). Predicting the pathogenicity of novel variants in mitochondrial tRNA with MitoTIP. *PLoS Computational Biology*, *13*(12), 1–8.

Spang, A., Saw, J. H., Jørgensen, S. L., Zaremba-Niedzwiedzka, K., Martijn, J., Lind, A. E., van Eijk, R., Schleper, C., Guy, L., & Ettema, T. J. G. (2015). Complex archaea that bridge the gap between prokaryotes and eukaryotes. *Nature*, *521*(7551), 173–179.

Spang, A., Stairs, C. W., Dombrowski, N., Eme, L., Lombard, J., Caceres, E. F., Greening, C., Baker, B. J., & Ettema, T. J. G. (2019). Proposal of the reverse flow model for the origin of the eukaryotic cell based on comparative analyses of Asgard archaeal metabolism. *Nature Microbiology*, *4*(7), 1138–1148.

Spencer, A. C., & Spremulli, L. L. (2004). Interaction of mitochondrial initiation factor 2 with mitochondrial fMet-tRNA. *Nucleic Acids Research*, *32*(18), 5464–5470.

Srivastava, S., & Moraes, C. T. (2001). Manipulating mitochondrial DNA heteroplasmy by a mitochondrially targeted restriction endonuclease. *Human Molecular Genetics*, *10*(26), 3093–3099.

Steinberg, S., & Cedergren, R. (1994). Structural compensation in atypical mitochondrial tRNAs. *Nature Structural & Molecular Biology*, *1*, 507–510.

Stewart, J. B. (2021). Current progress with mammalian models of mitochondrial DNA disease. *Journal of Inherited Metabolic Disease*, *44*(2), 325–342.

Stewart, J. B., & Chinnery, P. F. (2015). The dynamics of mitochondrial DNA heteroplasmy: Implications for human health and disease. *Nature Reviews Genetics*, *16*(9), 530–542.

Stewart, J. B., Freyer, C., Elson, J. L., Wredenberg, A., Cansu, Z., Trifunovic, A., & Larsson, N. G. (2008). Strong purifying selection in transmission of mammalian mitochondrial DNA. *PLoS Biology*, *6*(1), 0063–0071.

Suzuki, T. (2021). The expanding world of tRNA modifications and their disease relevance. *Nature Reviews Molecular Cell Biology*, *22*, 375–392.

Suzuki, T., Nagao, A., & Suzuki, T. (2011). Human mitochondrial trnas: Biogenesis, function, structural aspects, and diseases. *Annual Review of Genetics*, *45*, 299–329.

Suzuki, T., Yashiro, Y., Kikuchi, I., Ishigami, Y., Saito, H., Matsuzawa, I., Okada, S., Mito, M., Iwasaki, S., Ma, D., Zhao, X., Asano, K., Lin, H., Kirino, Y., Sakaguchi, Y., & Suzuki, T. (2020). Complete chemical structures of human mitochondrial tRNAs. *Nature Communications*, *11*, 1–15.

Swalwell, H., Deschauer, ; M, Hartl, ; H, Strauss, ; M, Turnbull, ; D M, Zierz, ; S, & Taylor, R. W. (2006). Pure myopathy associated with a novel mitochondrial tRNA gene mutation. *Neurology*, *66*, 447–449.

Tahmasebi, S., Khoutorsky, A., Mathews, M. B., & Sonenberg, N. (2018). Translation deregulation in human disease. *Nature Reviews Molecular Cell Biology*, *19*, 791–807.

Tan, B. G., Mutti, C. D., Shi, Y., Xie, X., Zhu, X., Silva-Pinheiro, P., Menger, K. E., Díaz-Maldonado, H., Wei, W., Nicholls, T. J., Chinnery, P. F., Minczuk, M., Falkenberg, M., & Gustafsson, C. M. (2022). The human mitochondrial genome contains a second light strand promoter. *Molecular Cell*, *82*(19), 1–15.

Tanaka, M., Borgeld, H.-J., Zhang, J., Muramatsu, S.-I., Gong, J.-S., Yoneda, M., Maruyama, W., Naoi, M., Ibi, T., Sahashi, K., Shamoto, M., Fuku, N., Kurata, M., Yamada, Y., Nishizawa, K., Akao, Y., Ohishi, N., Miyabayashi, S., Umemoto, H., … Yagi, K. (2002). Gene Therapy for Mitochondrial Disease by Delivering Restriction Endonuclease SmaI into Mitochondria. *Journal of Biomedical Science, 9*, 534–541.

Taylor, R. W., Barron, M. J., Borthwick, G. M., Gospel, A., Chinnery, P. F., Samuels, D. C., Taylor, G. A., Plusa, S. M., Needham, S. J., Greaves, L. C., Kirkwood, T. B. L., & Turnbull, D. M. (2003). Mitochondrial DNA mutations in human colonic crypt stem cells. *Journal of Clinical Investigation*, *112*(9), 1351–1360.

Taylor, R. W., & Turnbull, D. M. (2005). Mitochondrial DNA mutations in human disease. *Nature Reviews Genetics*, *6*(5), 389–402.

Temperley, R. J., Wydro, M., Lightowlers, R. N., & Chrzanowska-Lightowlers, Z. M. (2010). Human mitochondrial mRNAs-like members of all families, similar but different. *Biochimica et Biophysica Acta – Bioenergetics*, *1797*(6–7), 1081–1085.

Temperley, R., Richter, R., Dennerlein, S., Lightowlers, R. N., & Chrzanowska-Lightowlers, Z. M. (2010). Hungry codons promote frameshifting in human mitochondrial ribosomes. *Science, 327*, 301.

Terzioglu, M., Ruzzenente, B., Harmel, J., Mourier, A., Jemt, E., López, M. D., Kukat, C., Stewart, J. B., Wibom, R., Meharg, C., Habermann, B., Falkenberg, M., Gustafsson, C. M., Park, C. B., & Larsson, N. G. (2013). MTERF1 Binds mtDNA to prevent transcriptional interference at the light-strand promoter but is dispensable for rRNA gene transcription regulation. *Cell Metabolism, 17*(4), 618–626.

Trifunovic, A., Wredenberg, A., Falkenberg, M., Spelbrink, J. N., Rovio, A. T., Bruder, C. E., Bohlooly-Y, M., Gidlöf, S., Oldfors, A., Wibom, R., Törnell, J., Jacobs, H. T., & Larsson, N.-G. (2004). Premature ageing in mice expressing defective mitochondrial DNA polymerase. *Nature, 429*, 417–423.

Tsuboi, M., Morita, H., Nozaki, Y., Akama, K., Ueda, T., Ito, K., Nierhaus, K. H., & Takeuchi, N. (2009). EF-G2mt Is an Exclusive Recycling Factor in Mammalian Mitochondrial Protein Synthesis. *Molecular Cell, 35*(4), 502–510.

Tuppen, H. A. L., Blakely, E. L., Turnbull, D. M., & Taylor, R. W. (2010). Mitochondrial DNA mutations and human disease. *Biochimica et Biophysica Acta – Bioenergetics*, 1797(2), 113–128.

Tyynismaa, H., Mjosund, K. P., Wanrooij, S., Lappalainen, I., Ylikallio, E., Jalanko, A., Spelbrink, J. N., Paetau, A., & Suomalainen, A. (2005). Mutant mitochondrial helicase Twinkle causes multiple mtDNA deletions and a late-onset mitochondrial disease in mice. *Proceedings of the National Academy of Sciences, 102*(49), 17687–17692.

Tyynismaa, H., & Suomalainen, A. (2009). Mouse models of mitochondrial DNA defects and their relevance for human disease. *EMBO Reports*, *10*(2), 137–143.

Umbria, M., Ramos, A., Aluja, M. P., & Santos, C. (2020). The role of control region mitochondrial DNA mutations in cardiovascular disease: stroke and myocardial infarction. *Scientific Reports*, *10*, 1–10.

Urbauer, E., Rath, E., & Haller, D. (2021). Mitochondrial Metabolism in the Intestinal Stem Cell Niche—Sensing and Signaling in Health and Disease. *Frontiers in Cell and Developmental Biology*, *8*, 1–14.

Van Berge, L., Dooves, S., Van Berkel, C. G. M., Polder, E., Van Der Knaap, M. S., & Scheper, G. C. (2012). Leukoencephalopathy with brain stem and spinal cord involvement and lactate elevation is associated with cell-type-dependent splicing of mtAspRS mRNA. *Biochemical Journal*, *441*, 955–962.

Van Der Flier, L. G., & Clevers, H. (2009). Stem cells, self-renewal, and differentiation in the intestinal epithelium. *Annual Review of Physiology*, *71*, 241–260.

van der Knaap, M. S., van der Voorn, P., Barkhof, F., Van Coster, R., Krägeloh-Mann, I., Feigenbaum, A., Blaser, S., Vles, J. S. H., Rieckmann, P., & Pouwels, P. J. W. (2003). A New Leukoencephalopathy with Brainstem and Spinal Cord Involvement and High Lactate. *Annals of Neurology*, *53*(2), 252–258.

Veitia, R. A. (2018). How the most common mitochondrial DNA mutation (m.3243A > G) vanishes from leukocytes: A mathematical model. *Human Molecular Genetics*, *27*(9), 1565–1571.

Wai, T., Teoli, D., & Shoubridge, E. A. (2008). The mitochondrial DNA genetic bottleneck results from replication of a subpopulation of genomes. *Nature Genetics*, *40*(12), 1484–1488.

Wallace, D. C., Singh, G., Lotr, M. T., Hodge, J. A., Schurr, T. G., Lezza, A. M. S., Elsas II, L. J., & Nikoskelainen, E. K. (1988). Mitochondrial DNA Mutation Associated with Leber's Hereditary Optic Neuropathy. *Science*, *242*, I427–I430.

Wang, Z., & Wu, M. (2015). An integrated phylogenomic approach toward pinpointing the origin of mitochondria. *Scientific Reports*, *5*, 1–12.

Wanrooij, P. H., Uhler, J. P., Simonsson, T., Falkenberg, M., & Gustafsson, C. M. (2010). G-quadruplex structures in RNA stimulate mitochondrial transcription termination and primer formation. *Proceedings of the National Academy of Sciences*, *107*(37), 16072–16077.

Wasilewski, M., Chojnacka, K., & Chacinska, A. (2017). Protein trafficking at the crossroads to mitochondria. *Biochimica et Biophysica Acta - Molecular Cell Research*, *1864*, 125–137.

Watanabe, K. (2010). Unique features of animal mitochondrial translation systems: The non-universal genetic code, unusual features of the translational apparatus and their relevance to human mitochondrial diseases. *Proceedings of the Japan Academy Series B: Physical and Biological Sciences*, *86*(1), 11–39.

Wei, Y., Li, Z., Xu, K., Feng, H., Xie, L., Li, D., Zuo, Z., Zhang, M., Xu, C., Yang, H., & Zuo, E. (2022). Mitochondrial base editor DdCBE causes substantial DNA off-target editing in nuclear genome of embryos. *Cell Discovery*, *8*, 1–4.

Westermann, B. (2010). Mitochondrial fusion and fission in cell life and death. *Nature Reviews Molecular Cell Biology*, *11*(12), 872–884.

Willis, J. C. W., Silva-Pinheiro, P., Widdup, L., Minczuk, M., & Liu, D. R. (2022). Compact zinc finger base editors that edit mitochondrial or nuclear DNA in vitro and in vivo. *Nature Communications*, *13*, 1–16.

Wolburg, H., & Paulus, W. (2010). Choroid plexus: Biology and pathology. *Acta Neuropathologica*, *119*, 75–88.

Xu, H., Liu, Y. Y., Li, L. S., & Liu, Y. S. (2023). Sirtuins at the Crossroads between Mitochondrial Quality Control and Neurodegenerative Diseases: Structure, Regulation, Modifications, and Modulators. *Aging and Disease*, *14*(3), 794–824.

Yakubovskaya, E., Mejia, E., Byrnes, J., Hambardjieva, E., & Garcia-Diaz, M. (2010). Helix unwinding and base flipping enable human MTERF1 to terminate mitochondrial transcription. *Cell*, *141*(6), 982–993.

Yasukawa, T., Reyes, A., Cluett, T. J., Yang, M. Y., Bowmaker, M., Jacobs, H. T., & Holt, I. J. (2006). Replication of vertebrate mitochondrial DNA entails transient ribonucleotide incorporation throughout the lagging strand. *EMBO Journal*, *25*(22), 5358–5371.

Yi, Z., Zhang, X., Tang, W., Yu, Y., Wei, X., Zhang, X., & Wei, W. (2023). Strand-selective base editing of human mitochondrial DNA using mitoBEs. *Nature Biotechnology*. https://doi.org/10.1038/s41587-023-01791-y

Ylikallio, E., & Tyynismaa, H. (2015). Generating Mouse Models of Mitochondrial Disease. In *Movement Disorders: Genetics and Models: Second Edition* (pp. 689–701). Elsevier Inc.

Zacharioudakis, E., Agianian, B., Kumar MV, V., Biris, N., Garner, T. P., Rabinovich-Nikitin, I., Ouchida, A. T., Margulets, V., Nordstrøm, L. U., Riley, J. S., Dolgalev, I., Chen, Y., Wittig, A. J. H., Pekson, R., Mathew, C., Wei, P., Tsirigos, A., Tait, S. W. G., Kirshenbaum, L. A., … Gavathiotis, E. (2022). Modulating mitofusins to control mitochondrial function and signaling. *Nature Communications*, *13*, 1–20.

Zaremba-Niedzwiedzka, K., Caceres, E. F., Saw, J. H., Bäckström, Di., Juzokaite, L., Vancaester, E., Seitz, K. W., Anantharaman, K., Starnawski, P., Kjeldsen, K. U., Stott, M. B., Nunoura, T., Banfield, J. F., Schramm, A., Baker, B. J., Spang, A., & Ettema, T. J. G. (2017). Asgard archaea illuminate the origin of eukaryotic cellular complexity. *Nature*, *541*(7637), 353–358.

Zekonyte, U., Bacman, S. R., Smith, J., Shoop, W., Pereira, C. V., Tomberlin, G., Stewart, J., Jantz, D., & Moraes, C. T. (2021). Mitochondrial targeted meganuclease as a platform to eliminate mutant mtDNA in vivo. *Nature Communications*, *12*, 1–11.

Zhu, J., & Thompson, C. B. (2019). Metabolic regulation of cell growth and proliferation. *Nature Reviews Molecular Cell Biology*, *20*, 436–450.

SUPPLEMENTARY MATERIAL

Supplementary Table 1 Point mutations in mt-tRNA^{ALA} and the reported mitochondrial DNA base substitution diseases from the MITOMAP.

Allele	Position	Homo-plasmy	Hetero-plasmy	Disease	Status	MitoTIP
m.5587T>C	55887	+	+	LHON / possible DEAF modifier / dilated cardiomyopathy / hypertension / tic disorder	Reported	12.10% ↓↓
m.5591G>A	5591	-	+	Myopathy	Reported	68.40% ↑
m.5592A>G	5592	+	-	Coronary Heart Disease	Reported	0.40% ↓↓
m.5595G>A	5595	nr	nr	Reported in tic disorder patient	Reported	64.60% ↑
m.5601C>T	5601	+	-	Possible 4435G helper in maternally inherited hypertension	Reported	4.20% ↓↓*
m.5610G>A	5610	-	+	Myopathy	Reported	38.70% ↓
m.5613T>C	5613	-	+	CPEO	Reported	59.30% ↑
m.5618T>C	5618	nr	nr	Hearing loss patient	Reported	28.30% ↓
m.5628T>C	5628	-	+	CPEO / DEAF enhancer / gout / tic disorder		78.90% ↑↑
m.5631G>A	5631	-	+	Myopathy	Reported	43.40% ↓
m.5636T>C	5636	-	+	PEO	Reported	73.50% ↑
m.5641T>C	5641	nr	nr	Hearing loss patient	Reported	28.40% ↓
m.5650G>A	5650	-	+	Myopathy	Cfrm	Pathogenic ↑↑↑
m.5652C>G	5652	+	-	Dilated Cardiomyopathy	Reported	69.90% ↑
m.5655T>C	5655	+	-	DEAF enhancer / Hypertension risk	Reported	26.70% ↓*

MitoTIP:

↑↑↑ confirmed pathogenic

↑↑ likely pathogenic

↑ possibly pathogenic

↓ possibly benign

↓↓ likely benign

* frequency alert

Supplementary Table 2 Body and heart weight values of WT and A5019G mice at 20-36 weeks and 49-68 weeks.

		20-36 weeks old		49-68 weeks old	
		Body weight (g)	Heart weight (g)	Body weight (g)	Heart weight (g)
WT male	1	38.22	0.1388	46.88	0.1483
	2	33.76	0.1301	50.1	0.1659
	3	31.46	0.1407	43.1	0.1681
	4	28.53	0.1394	48.18	0.1917
	5	34.44	0.1375	48.7	0.1775
	6	34.49	0.1465	39.15	0.1625
	7	32.21	0.1228	50.36	0.2271
	8	35.1	0.1401	39.51	0.1592
	9	31.46	0.1636	52.65	0.1905
A5019G male	1	28.38	0.1339	32.37	0.1888
	2	34.12	0.1389	27.88	0.1654
	3	28.86	0.1623	34.85	0.1801
	4	29.77	0.162	32.89	0.1739
	5	29.33	0.1773	26.69	0.1919
	6	36.21	0.1564	34.05	0.1747
	7	35.48	0.1806	22.67	0.1464
	8	32.12	0.1518	28.6	0.1904
	9	29.89	0.126	30.6	0.1695
WT female	1	24.05	0.115	24.14	0.1192
	2	27.85	0.1114	30.41	0.1268
	3	21.7	0.0964	33.6	0.1333
	4	32.88	0.1516	36.07	0.1362
	5	29.51	0.127	31	0.123
	6	33.34	0.1218	33.02	0.1347
	7	36.37	0.1383	34.21	0.1438
	8	27.19	0.126	31.2	0.1652
	9	24.86	0.11309	38.8	0.1525
A5019G female	1	20.31	0.112	31.88	0.1597
	2	21.66	0.1183	30.12	0.1874
	3	22.67	0.1271	22.5	0.1296
	4	24.1	0.1578	25.52	0.2114
	5	25.64	0.1581	26.73	0.142
	6	26.27	0.1448	28.84	0.1745
	7	26.27	0.1448	25.51	0.1347
	8	28.46	0.1237	26	0.1301
	9	23.76	0.127	21.73	0.1283

Supplementary Table 3 Heteroplasmy levels in various tissues of A5019G mice.

#	Mouse ID	Gender	Age (weeks)	% m.5019A>G							
				ear clip	heart	lung	liver	skm2	kidney	small intestine	colon
1	T801	f	37	52	59	64	63	51	65	69	73
2	T804	f	37	77	49	61	60	53	53	72	65
3	U224	f	30	77	77	78.3	77	66	80.3	77	80
4	U337	m	29	74	79.7	76.3	78	76	80.77	75	78
5	U339	f	31	76	60	73	75	63	76	81	78

Supplementary Table 4 Difference in heteroplasmy levels among tissue types.

	m.5019A>G (tissue-ear)				
Animal ID	T801	T804	U224	U337	U339
Heart	1	-3	0	2.7	-14
Lung	6	9	1.3	-0.7	-1
Liver	5	8	0	1	1
Skm2	-7	1	-11	-1	-11
Kidney	7	1	3.3	3.7	2
Small intestine	11	20	0	-2	7
Colon	15	13	3	1	4

Supplementary Table 5 Heteroplasmy levels in colonic crypts of A5019G mouse.

m.5019A>G (COX+ crypts)	m.5019A>G (COX- crypts)
37%	85%
58%	84%
63%	84%
54%	84%
67%	85%
47%	76%
66%	83%
52%	85%
56%	85%
71%	86%
45%	83%

Supplementary Table 6 NBTx quantification in heart tissue: Percentage of COX deficient cells in different blue optical density ranges.

	101-150 blue optical density range	151-200 blue optical density range	201-255 blue optical density range
WT	0.00015511%	0.00012527%	0%
59% m.5019A>G	0.00296252%	0.00033406%	0.00014411%
63% m.5019A>G	0.00062042%	0.00112745%	0%
72% m.5019A>G	3.28405468%	2.54382926%	1.62140117%
75% m.5019A>G	13.3886275%	10.5217378%	6.2587728%
76% m.5019A>G	16.6556464%	20.2650729%	25.4522226%

Supplementary Table 7 NBTx quantification in kidney tissue: Percentage of COX deficient cells in different blue optical density ranges.

	101-150 blue optical density range	151-200 blue optical density range	201-255 blue optical density range
WT	0.0040509%	0.00702219%	0.00037151%
53% m.5019A>G	0.00028806%	0.00023278%	0.00012384%
65% m.5019A>G	0.00387086%	0.00054315%	0%
76% m.5019A>G	1.55538224%	1.30294626%	1.10995117%
80% m.5019A>G	16.4186258%	17.251235%	16.4035749%
81% m.5019A>G	15.3511155%	14.771354%	15.8193119%

Supplementary Table 8 NBTx quantification in liver tissue: Percentage of COX deficient cells in different blue optical density ranges.

	101-150 blue optical density range	151-200 blue optical density range	201-255 blue optical density range
WT	0.00064803%	0.0000560666%	0.00020558%
60% m.5019A>G	0.14908555%	0.075185314%	0.01572666%
63% m.5019A>G	0.00991108%	0.005158127%	0.00154183%
75% m.5019A>G	14.0228855%	14.64538154%	16.9957959%
77% m.5019A>G	19.1480205%	18.60373975%	16.3183159%

Supplementary Table 9 NBTx quantification in small intestinal tissue: Percentage of COX deficient cells in different blue optical density ranges.

	101-150 blue optical density range	151-200 blue optical density range	201-255 blue optical density range
WT	0	0	0
69% m.5019A>G	8.73657255%	9.1190176%	8.32317464%
72% m.5019A>G	0.9273014%	0.27862085%	0.13990362%
75% m.5019A>G	5.78146278%	5.00066074%	4.33619413%
77% m.5019A>G	2.28182437%	1.06059523%	0.56438703%
81% m.5019A>G	15.6061722%	17.8744389%	19.9696739%

Supplementary Table 8 NBTx quantification in colonic tissue: Percentage of COX deficient cells in different intensity value ranges.

	101-150 blue optical density range	151-200 blue optical density range	201-255 blue optical density range
WT	0.00096907%	0.00062229%	0%
65% m.5019A>G	7.6403223%	10.6501303%	1.08518382%
73% m.5019A>G	8.19633701%	9.87143426%	1.01337259%
78% m.5019A>G	8.78853029%	6.16816847%	0.36134626%
78% m.5019A>G	5.23901618%	5.01671894%	0.51265693%
80% m.5019A>G	3.46815848%	1.62625911%	0.05774343%

Supplementary Table 9 LogFC values of proteins involved in various mitochondrial processes in C5024T and A5019G mice. Significant at p<0.05 (*).

Group	Gene name	C5024T mice	A5019G mice	
		22-26 weeks	22-26 weeks	58-66 weeks
Complex I	mt-Nd4			-0.901*
	Ndufa1	0.124	-0.357	
	Ndufa2	-0.212	-1.341*	-1.111*
	Ndufa3	-0.372	-0.608	-0.685*
	Ndufa5	-0.355	-1.259*	-0.965*
	Ndufa6	-0.329	-1.579*	-1.129*
	Ndufa7	-0.414	-1.677*	-1.279*
	Ndufa8	-0.432	-1.331*	-0.741*
	Ndufa9	-0.25	-1.34*	-0.737*
	Ndufa10	-0.484	-1.546*	-0.69*
	Ndufa11	-0.385	-1.544*	-1.254*
	Ndufa12	-0.449	-1.632*	-1.296*
	Ndufa13	-0.499	-1.064*	-1.061*
	Ndufab1	-0.447	-0.585*	
	Ndufb2	-0.462	-1.497*	-1.616*
	Ndufb3	-0.21	-1.61	-1.238*

	Ndufb4	-0.594*	-1.517*	-1.753*
	Ndufb5	-0.452	-0.801*	-0.323
	Ndufb6	-0.283	-0.68	-1.047*
	Ndufb7	-0.661*	-1.64*	-1.268*
	Ndufb8	-0.696	-1.493*	-1.369
	Ndufb9	-0.42	-1.477	-1.19*
	Ndufb10	-0.279	-1.038	-0.653
	Ndufb11	-0.723*	-0.984*	-0.397
	Ndufc2	-0.371	-1.105*	-0.914*
	Ndufs1	-0.529*	-1.469*	-0.884*
	Ndufs2	-0.55	-1.234*	-0.959
	Ndufs3	-0.543	-1.162*	-0.801*
	Ndufs4	-0.659	-1.74*	-1.76*
	Ndufs5	-0.704*	-1.725*	-1.346*
	Ndufs6	-0.541	-1.59*	-1.025*
	Ndufs7	-0.549	-1.309*	-1.128*
	Ndufs8	-0.567	-1.429*	-1.15*
	Ndufv1	-0.499	-1.539*	-1.014*
	Ndufv2	-0.549*	-1.395*	-0.588*
	Ndufv3	-0.506	-1.488*	0.489
Complex II	Sdha	-0.071	-0.214	0.452
	Sdhb	0.055	-0.265	0.243
	Sdhd	-0.111	-0.148	-0.053
Complex III	Cyc1	-0.355	-0.541	0.37
	Uqcr10	-0.204	-0.245	
	Uqcr11	0.062	-0.533	
	Uqcrb	-0.154	-1.269*	-0.437
	Uqcrc1	-0.262	-0.744*	-0.106
	Uqcrc2	-0.152	-0.899*	-0.535*
	Uqcrfs1	-0.023	-0.954*	-0.806*
	Uqcrh	0.02	-0.495	0.221
	Uqcrq	-0.208	-1.136*	-0.864*
Complex IV	mt-Co2	-0.355	-1.087*	-0.76*
	Cox4i1	-0.266	-1.044	-0.408*
	Cox5a	-0.218	-1.039	-0.688*
	Cox5b	-0.414	-1.343*	-1.306*
	Cox6a1	-0.505	-1.652*	-1.115*
	Cox6b1	-0.31	-1.696	-1.522*
	Cox6c	-0.78*	-1.7*	-1.21*
	Cox7a1	-0.411	-1.609	-1.116*
	Cox7a2	-0.41	-1.377*	-1.306*
	Cox7a2l	-0.035	-0.722	
	Cox7c	-0.265	-1.451	-1.588*
	Ndufa4	-0.36	-1.224*	-0.601
Complex V	mt-Atp8	-0.068	-0.203	0.18
	Atp5c1	-0.088	-0.192	0.414
	Atp5h	-0.242	-0.336	0.402
	Atp5j	-0.115	-0.333	-0.057
	Atp5j2	-0.051	-0.088	0.326
	Atp5l	-0.146	-0.145	0.071
	Atp5o	0.125	-0.45	0.089
	Atpif1	0.14	-0.864	-0.907*
OXPHOS Assembly Factors	Acad9	-0.191	0.096	0.71*
	Aifm1	0	-0.333	0.207
	Dmac1	-0.462	0.161	

	Dmac2	0.149	-0.691	-0.088
	Ecsit	-0.013	-0.002	0.291
	Foxred1	-0.11	-0.008	-0.036
	Lyrm2	-0.023	-0.311	0.624
	Ndufaf1	-0.117	0.097	0.82*
	Ndufaf2	-0.105	-0.182	0.558
	Ndufaf3	-0.013	-0.091	0.41*
	Ndufaf4	-0.063	-0.088	0.317
	Ndufaf5	-0.171	-0.301	0.154
	Ndufaf6	-0.197	-0.122	0.532*
	Ndufaf7	-0.073	-0.22	0.385
	Ndufaf8	-0.048	-0.199	-0.115
	Nubpl	-0.253	-0.094	0.49
	Timmdc1	-0.031	0.325	0.935*
	Tmem186	-0.032	0.18	0.318
	Sdhaf1	-0.005	-0.135	
	Sdhaf2	0.025	0.441	0.226
	Sdhaf4	-0.118	0.306	1.032*
	Bcs1l	-0.175	0.072	0.428*
	Lyrm7	0.025	-0.167	0.645
	Ttc19	-0.182	0.002	0.631*
	Uqcc1	0.005	0.118	0.524*
	Uqcc2	0.176	0.004	0.485*
	Uqcc3	-0.49	-2.146*	-1.203*
	Cep89	-0.274	0.814	-0.043
	Cmc1	-0.376	-0.792*	-0.143
	Cmc2	0.124	-0.387	-0.723
	Coa3	0.032	-0.587*	-0.243
	Coa4	-0.325	-0.33	0.364
	Coa5	-0.607	-1.489	
	Coa6	-0.054	-0.243	0.058
	Coa7	-0.255	-0.409	
	Cox10	-0.11	0.384	1.038*
	Cox14	0.065	-0.61	
	Cox16			0.689*
	Cox17	-0.307	0.193	1.282*
	Cox19	-0.131	-0.461	0.108
	Cox20	-0.05	0.075	
	Higd1a	-0.102	0.138	
	Pet100	0.198	-0.817*	-0.798*
	Pet117	0.009	-0.356	-0.263
	Pnkd	-0.198	-0.362	0.43
	Sco1	0.052	-0.094	0.374
	Sco2	-0.053	-0.132	0.721*
	Smim20	0.155	-0.409	0.068
	Surf1	0.119	0.067	0.272
	Taco1	-0.153	-0.287	0.212
	Timm21	0.079	-0.03	
	Tmem177	0.059	-0.169	
	Atpaf1	0.471	-0.117	0.382
	Atpaf2	-0.186	0.263	
	Fmc1	0.132	-0.256	0.09
mtDNA Maintenance	Apex1	0.128	0.074	-0.284
	Endog	-0.244	-0.968*	-0.092
	Exog	-0.127	-0.212	-0.217

	Lig3	0.095		0.074
	Mgme1	-0.081	-0.177	0.85
	Mterf1b			0.764*
	Mterf2	-0.34	-0.189	
	Polb	0.136	-0.095	-0.066
	Poldip2	-0.258	-0.104	0.402
	Polg			0.67*
	Polrmt	0.098	-0.14	0.742*
	Ppa2	-0.201	-0.417	0.618
	Rnaseh1	-0.077	0.077	
	Ssbp1	-0.117	-0.268	0.23
	Tfam	-0.201	-0.678	0.156
	Tfb2m	0.129	-0.139	
	Ung	0.099	-0.416	0.078
mtRNA Metabolism	Alkbh1	-0.771*	0.013	
	Angel2	0.015	-0.005	0.265
	Cdk5rap1	-0.858	0.187	0.496*
	Ddx28	-0.077	0.062	0.879*
	Dhx30	0.068	0.194	0.393*
	Dus2			-0.224
	Elac2	-0.098	0.279	0.263
	Endog	-0.244	-0.968	-0.092
	Eral1	-0.043	0.256	1.001*
	Fastkd2	-0.257		
	Fastkd3			
	Fastkd5	-0.099	-0.38	0.08
	Grsf1	-0.03	0.262	0.801*
	Gtpbp3	-0.119	-0.206	0.544
	Hsd17b10	-0.222	-0.233	0.482
	Lactb2	-0.008	-0.177	0.079
	Lrpprc	-0.219	-0.048	0.785*
	Mettl15	-0.08	-0.088	
	Mettl17	-0.16	0.031	0.655*
	Mettl5			
	Mettl8	-0.066	0.169	0.976*
	Mrm1	-0.125	-0.066	0.562
	Mrm2	-0.16	-0.315	0.197
	Mrm3	0.272	-0.261	0.583*
	Mrpl12	0.3	-0.353	0.481
	Mrpl47	-0.017	-0.171	0.691*
	Mrps7	-0.032	-0.002	0.448
	Mrps9	0.104	0.025	0.554
	Mterf1a			
	Mterf1b			0.764*
	Mto1	-0.103	-0.07	0.15
	Mtpap	0.23	-0.126	0.551*
	Mtres1			
	Myg1	0.235	-0.25	-0.497*
	Ngrn	0.231	0.313	1.01*
	Noa1	0.128	-0.008	0.781*
	Nsun2	0.114	0.111	-0.453*
	Nsun3			
	Nsun4	-0.126	-0.043	0.422
	Osgepl1			
	Pde12	0.152	0.135	0.523*

	Pnpt1	-0.161	-0.102	0.51*
	Polrmt	0.098	-0.14	0.742*
	Ppa2	-0.201	-0.417	0.618
	Prorp			
	Ptcd1	-0.246	0.254	0.861*
	Ptcd2	-0.19	0.249	
	Pus1	-0.153	0.053	0.054
	Qtrt1	0.014	-0.087	-0.173
	Rcc1l	0.055	-0.022	0.611*
	Rexo2	0.073	0.076	-0.304
	Rnaseh1	-0.077	0.077	
	Rpusd3	-0.164	-0.16	0.439
	Rpusd4	-0.022	0.112	0.317
	Slirp	-0.063	-0.252	0.222
	Supv3l1	-0.199	-0.208	0.423
	Tbrg4	-0.094	-0.014	0.276
	Tefm	-0.007	-0.082	1.114*
	Tfam	-0.201	-0.678	0.156
	Tfb1m	-0.163	0.044	0.372
	Tfb2m	0.129	-0.139	
	Top1mt			
	Trit1			0.3
	Trmt1	0.716	0.244	-0.307
	Trmt10c	-0.156	-0.106	0.421
	Trmt2b	-0.249	0.013	
	Trmt5			-0.261
	Trmu	0.133	-0.15	0.409
	Trnt1	-0.052	0.148	0.49*
	Trub2	0.055	0.573*	1.221*
	Ybey			
Mitochondrial ribosome	Aurkaip1	0.058	-0.205	0.197
	Chchd1	0.359	-0.42	0.26
	Dap3	-0.002	0.052	0.697*
	Gadd45gip1	0.069	-0.077	0.405
	Mrpl1	-0.143	-0.078	0.352
	Mrpl10	-0.199	-0.071	0.55*
	Mrpl11	-0.057	-0.168	0.216
	Mrpl12	0.3	-0.353	0.481
	Mrpl13	-0.036	-0.043	0.484
	Mrpl14	-0.042	-0.483	0.63*
	Mrpl15	-0.007	-0.115	0.489
	Mrpl16	-0.287	-0.13	0.817*
	Mrpl17	0.135	-0.14	-0.222
	Mrpl18	-0.305	0.081	0.291
	Mrpl19	-0.148	-0.107	0.572*
	Mrpl2	0.037	-0.026	0.413
	Mrpl20	-0.189	-0.134	0.765*
	Mrpl21	-0.065	-0.266	0.603*
	Mrpl22	-0.084	-0.233	0.028
	Mrpl23	-0.116	-0.123	0.335
	Mrpl24	-0.045	-0.137	0.557*
	Mrpl27	0.035	-0.106	0.399
	Mrpl28	-0.199	-0.281	0.195
	Mrpl3	-0.197	-0.148	0.496
	Mrpl30	-0.251	0.088	0.267

Mrpl33	-0.12	-0.147	0.518*
Mrpl34			-0.391
Mrpl35	-0.455	-0.152	0.475
Mrpl37	-0.103	-0.114	0.609*
Mrpl38	-0.283	-0.077	0.533*
Mrpl39	-0.12	0.091	0.419
Mrpl4	-0.285	-0.148	0.45
Mrpl40	0.101	-0.264	0.261
Mrpl41	-0.168	0.037	0.466
Mrpl42	0.217	-0.193	0.055
Mrpl43	-0.006	-0.131	0.683*
Mrpl44	-0.623	-0.492	-0.128
Mrpl45	-0.334	-0.145	0.258
Mrpl46	-0.088	-0.124	0.416
Mrpl47	-0.017	-0.171	0.691*
Mrpl48	0.166	-0.374	0.329
Mrpl49	-0.105	0.002	0.363
Mrpl50	-0.025	0.139	0.521*
Mrpl51	-0.169	-0.268	0.453
Mrpl52	-0.117	-0.064	
Mrpl53	-0.211	-0.229	0.576*
Mrpl54	-0.447	-0.137	
Mrpl55	0.042	-0.185	-0.102
Mrpl57	-0.114	-0.184	0.409
Mrpl58	0.167	-0.231	0.518
Mrpl9	-0.163	-0.138	0.374
Mrps10	0.003	-0.073	0.819*
Mrps11	0.096	-0.168	0.375
Mrps12	-0.196	0.155	0.846*
Mrps14	-0.101	-0.21	-0.02
Mrps15	-0.095	-0.155	0.581
Mrps16	-0.143	-0.191	0.329
Mrps17	0.034	-0.163	0.465
Mrps18a			0.755*
Mrps18b	-0.151	-0.11	0.616*
Mrps18c	-0.016	-0.054	
Mrps2	0.482	-0.222	0.68*
Mrps21	0.079	-0.222	0.287
Mrps22	-0.23	-0.05	0.894*
Mrps23	0.042	-0.141	0.345
Mrps24	0.014	-0.069	0.075
Mrps25	-0.098	-0.068	0.847*
Mrps26	-0.077	0.015	0.373
Mrps27	-0.099	-0.02	0.71*
Mrps28	-0.198	-0.039	0.652*
Mrps30	-0.149	-0.13	0.697*
Mrps31	-0.258	-0.265	0.758*
Mrps33	-0.022	-0.136	0.419
Mrps34	-0.1	-0.039	0.407
Mrps35	-0.104	-0.061	0.617*
Mrps36	-0.11	-0.451	0.024
Mrps5	-0.032	-0.056	0.485
Mrps6	-0.101	-0.054	-0.197
Mrps7	-0.032	-0.002	0.448
Mrps9	0.104	0.025	0.554

	Ptcd3	-0.657	-0.558	0.639*
Mitochondrial ribosome assembly	Ddx28	-0.077	0.062	0.879*
	Dhx30	0.068	0.194	0.393*
	Eral1	-0.043	0.256	1.001*
	Fastkd2	-0.257	0.078	
	Grsf1	-0.03	0.262	0.801*
	Gtpbp10	-0.108	-0.049	0.747*
	Mettl17	-0.16	0.031	0.655*
	Mief1	0.145	-0.245	-0.054
	Mpv17l2	-0.34	0.225	
	Mrm2	-0.16	-0.315	0.197
	Mrm3	0.272	-0.261	0.583*
	Mterf3	-0.404	0.538	
	Mterf4	0.196	-0.036	0.09
	Mtg1	0.02	-0.178	0.306
	Mtg2	-0.057	0.086	0.303
	Ngrn	0.231	0.313	1.01*
	Noa1	0.128	-0.008	0.781*
	Nsun4	-0.126	-0.043	0.422
	Ptcd3	-0.657	-0.558	0.639*
	Rbfa	-0.106	-0.232	0.639*
	Tfb1m	-0.163	0.044	0.372
Translation factors	Coa3	0.032	-0.587	-0.243
	Cox14	0.065	-0.61	
	Gfm1	-0.11	0.089	0.836*
	Gfm2	-0.144	0.035	0.788*
	Mrpl58	0.167	-0.231	0.518
	Mrrf	-0.252	-0.189	0.532
	Mtif2	-0.074	-0.344	0.119
	Mtif3	-0.249	-0.221	0.584*
	Mtrf1	-0.401	-0.348	0.214
	Mtrf1l	-0.18	-0.345	0.194
	Taco1	-0.153	-0.287	0.212
	Timm21	0.079	-0.03	
	Tsfm	-0.358	-0.32	0.481
	Tufm	-0.242	-0.166	0.366
mt-tRNA synthetases	Aars2	-0.01	-0.047	0.918*
	Cars2	-0.149	0.224	0.73*
	Dars2	-0.298	-0.128	0.623*
	Ears2	-0.132	-0.193	0.42
	Fars2	-0.238	0.181	0.736*
	Gars	0.127	0.495	-0.111
	Gatb	-0.254	-0.053	0.701*
	Gatc	-0.154	0.002	0.725*
	Hars2	-0.122	-0.149	0.327
	Iars2	-0.161	-0.079	0.638*
	Kars	0.219	0.422	-0.505*
	Lars2	-0.121	0.038	0.58*
	Mars2	-0.128	0.115	1.34*
	Pars2	-0.273	-0.353	0.506
	Qrsl1	-0.059	-0.102	0.864*
	Rars2	-0.164	-0.07	0.746*
	Sars2	-0.014	-0.115	0.44
	Tars2	-0.165	-0.086	0.786*
	Vars2	-0.175	-0.118	0.52

	Wars2	-0.132	-0.026	0.457
	Yars2	-0.222	-0.167	0.393
fMet processing	Mtfmt	-0.116	-0.113	0.361
	Pdf	-0.223	-0.168	0.373

Supplementary Data. Fiji script for quantification of NBTx assay.

```
1    optionalManualRoiSelection=0;//if 1 manual ROI selection is offered for each image, if 0 autothresholding is applied without callback

2

3

4    directory=getDirectory("Choose a Directory");

5    filelist=getFileList(directory);

6    filelist=cleanFilelist(filelist);

7    resultpath=directory+File.separator+"ImageJ";

8    origFile="";

9    if(!File.exists(resultpath)){

10       File.makeDirectory(resultpath);

11   }

12   run("Clear Results");

13   run("Set Measurements...", "area mean standard min median area_fraction redirect=None decimal=3");

14   totalArea=newArray(filelist.length);

15   for(i=0;i<filelist.length;i++){

16       open(filelist[i]);

17       origImg=getImageID;

18       origFile=File.nameWithoutExtension;

19     deconvFile=resultpath+File.separator+origFile+"_"+i+".tif";

20       selectImage(origImg);

21       //TODO: Implement white balancing

22        //TODO: Implement interactive component vector creation

23     run("Colour Deconvolution", "vectors=[User values] [r1]=107 [g1]=86 [b1]=37 [r2]=12 [g2]=17 [b2]=14 [r3]=10 [g3]=10 [b3]=10");

24    //selectWindow("02_1345_NBTx15min_22DC_080616_001.tif-(Colour_3)");

25       close("*Colour_2*");

26    //selectWindow("02_1345_NBTx15min_22DC_080616_001.tif-(Colour_2)");

27       close("*Colour_3*");

28    //selectWindow("02_1345_NBTx15min_22DC_080616_001.tif-(Colour_1)");

29       deconvImg=getImageID;

30       run("Invert");

31       run("Invert LUT");

32       run("Duplicate...", " ");

33       maskImg=getImageID;

34       setAutoThreshold("Huang");

35       setOption("BlackBackground", true);
```

```
36    run("Convert to Mask");


37        run("Create Selection");
38        if(optionalManualRoiSelection){
39            discardAutothreshold=getBoolean("Would you like to change the selected ROI?");
40            if(discardAutothreshold){

                   close;
41

                   selectImage(deconvImg);
42

                   run("Duplicate...", " ");
43

                   maskImg=getImageID;
44
45

                   //Prompt until user selected ROI
46

                   setSelection=-1;
47

                   while(setSelection<0){
48

                       waitForUser("Create user defined selection");
49

                           setSelection=selectionType();
50

                   }
51
52            }
53        }
54    roiManager("Add");
55    selectImage(deconvImg);

56    roiManager("Select", i);
57    run("Measure");
58    selectImage(deconvImg);
59    run("Select All");
60    getStatistics(area);//assumes constant image size!
61    totalArea[i]=area;
62    save(deconvFile);
63    roiManager("Save", resultpath+File.separator+"RoiSet.zip");
64    close("*");
65  }
66  saveAs("Results",  resultpath+File.separator+"Values.csv");
```

```
67    roiManager("reset");
68    plottitle=origFile;
69
70    xlabel="Image number";
71    ylabel="Stain Intensity [a.u.]";
72    thrshAreaValues=newArray(nResults);
73    thrshMeanValues=newArray(nResults);
74    thrshStdDevValues=newArray(nResults);
75
76    for(i=0;i<nResults;i++){
77        thrshAreaValues[i]=getResult("Area",  i);
78        thrshMeanValues[i]=getResult("Mean",  i);
79        thrshStdDevValues[i]=getResult("StdDev", i);
80    }
81    yValues=thrshMeanValues;
82
83    Plot.create(plottitle, xlabel, ylabel);
84    //Plot.setLimits(0, 5, 0, 3);
85    Plot.setLineWidth(5);
86    Plot.setColor("darkGray");
87    Plot.add("line", thrshMeanValues);
88    Plot.add("error bars",
      thrshStdDevValues); 89
90
91    Plot.setColor("lightGray");
92    for(i=0;i<nResults;i++){
93        x=i*(1/(nResults-1));
94        areaPercentage=round((thrshAreaValues[i]/totalArea[i])*100);
95        Plot.addText(areaPercentage+"%", x, 0.12);
96        row=nResults-(nResults-i);
97        setResult("%Area",row,areaPercentage);
98    }

99
100
101   Plot.show();
102   saveAs("png",resultpath+File.separator+"Plot.png");
103
104   function cleanFilelist(filelist){
105       origLength=filelist.length;
106       cleanLength=origLength;
107       for(i=0;i<origLength;i++){
108                   if(!endsWith(filelist[i],".tif")){

                                        cleanLength=cleanLength-1;
109

110
```

```
111                      }
112      }
113        if(cleanLength==origLength) {
114                              return filelist;
115      }
116
117      cleanList=newArray(cleanLength);
118      idx=0;
119      for(i=0;i<origLength;i++){
120                              if(filelist[i]!="-"){
filelist[i]="-";

                                                cleanList[idx]=filelist[i];
121
                                                    idx=idx+1;
122
123                                    }
124      }
125      return cleanList;
126
```

ABBREVIATIONS

3'	3' end
5'	5' end
7S DNA	Mitochondrially encoded 7S DNA
12S rRNa	Mitochondrially encoded 12S ribosomal RNA
16S rRNA	Mitochondrially encoded 16S ribosomal RNA
AA	Amino acid
aaRS	Aminoacyl-tRNA synthetase
ATP	Adenosine triphosphate
BAK	Bcl-2 homologous antagonist/killer
BAX	Bcl-2-associated X protein
CI	Complex I, NADH:ubiquinone oxidoreductase
CII	Complex II, Succinate dehydrogenase
CIII	Complex III, Cytochrome c reductase
CIV	Complex IV, Cytochrome c oxidase
Ca^{2+}	Calcium ion
COX	Cytochrome c oxidase
CoA	Coenzyme A
CR	Control region
Cryo-EM	Cryo-electron microscopy
CSB	Conserved sequence block
CV	Complex V, ATP synthetase
CytC	Cytochorome C
D-loop	Displacement loop
DddA	Double-stranded DNA deaminase toxin A
DdCBE	DddA-derived cytosine base editor
DNA	Deoxyribonucleic acid
dNTP	Deoxynucleotide triphosphate
dsDNA	Double-stranded DNA
EDTA	Ethylenediamine tetraacetic acid
ETC	Electron transport chain
EtBr	Ethidium bromide
$FADH_2$	Flavin adenine dinucleotide
Fe-S	Iron-sulfur
GWAS	Genome-wide association study
H-strand	Heavy strand
HSP	Heavy strand promoter
IMM	Inner mitochondrial membrane
IMS	Intermembrane space
L-strand	Light strand
LECA	Last eukaryotic common ancestor
LMCA	Last mitochondrial common ancestor
LRPPRC	Leucine-rich PPR motif-containing protein

LSP	Light strand promoter
LHON	Leber's hereditary optic neuropathy
MELAS	Mitochondrial encephalopathy, lactic acidosis, and stroke-like episodes
MERFF	Myoclonic epilepsy with ragged red fibers
MFN	Mitofusin
MM	Mitochondrial matrix
MOMP	Mitochondria outer membrane permeability
MT-ATP6	Mitochondrially encoded ATP synthase 6
MT-ATP8	Mitochondrially encoded ATP synthase 8
MT-CO1	Mitochondrially encoded Cytochrome c oxidase I
MT-CO2	Mitochondrially encoded Cytochrome c oxidase II
MT-CO3	Mitochondrially encoded Cytochrome c oxidase III
MT-CYB	Mitochondrially encoded Cytochrome B
MT-ND1	Mitochondrially encoded NADH dehydrogenase 1
MT-ND2	Mitochondrially encoded NADH dehydrogenase 2
MT-ND3	Mitochondrially encoded NADH dehydrogenase 3
MT-ND4	Mitochondrially encoded NADH dehydrogenase 4
MT-ND4L	Mitochondrially encoded NADH 4L dehydrogenase
MT-ND5	Mitochondrially encoded NADH dehydrogenase 5
MT-ND6	Mitochondrially encoded NADH dehydrogenase 6
mtDNA	Mitochondrial DNA
MTERF1	Mitochondrial transcription termination factor 1
mtSSB	Mitochondrial single-stranded binding protein
NAD	Nicotinamide adenine dinucleotide
NADH	Nicotinamide adenine dinucleotide + hydrogen
NARP	Neurogenic muscle weakness, ataxia, and retinitis pigmentosa
NBT	Nitroblue tetrazolium
NCR	Non-coding region
nDNA	Nuclear DNA
O_H	Origin for heavy strand replication
O_L	Origin for light strand replication
OMM	Outer mitochondrial membrane
OPA1	Optic atrophy protein 1
OXPHOS	Oxidative phosphorylation
PAGE	Polyacrylamide gel electrophoresis
pAM1	Plasmid with mouse mitochondrial DNA
PBS	Phosphate-buffered saline
PCR	Polymerase chain reaction
PEO	Progressive external ophthalmoplegia
PGC	Primordial germ cell
PMS	Phenazine methosulfate
PPR	Pentatricopeptide repeat
Polγ	DNA polymerase gamma
POLRMT	DNA-directed RNA polymerase, mitochondrial
Q	Ubiquinone
RE	Restriction endonuclease

RNA	Ribonucleic acid	
ROS	Reactive oxygen species	
rRNA	Ribosomal RNA	
SDH	Succinate dehydrogenase	
SDS	Sodium dodecyl sulfate	
SDS-PAGE	Sodium dodecyl sulfate polyacrylamide gel electrophoresis	
SLIRP	Stem-loop interacting RNA binding protein	
SSBP	Single-stranded binding protein	
ssDNA	Single-stranded DNA	
TALE	Transcription activator-like effector	
TALED	TALE-linked deaminase	
TALEN	Transcription activator-like effector nuclease	
TAS	Termination associated sequence	
TBS	Tris-buffered saline	
TCA	Tricarboxylic acid	
TEFM	Mitochondrial transcription elongation factor	
TFAM	Mitochondrial transcription factor A	
TFB2M	Mitochondrial transcription factor B2	
TOP3α	Topoisomerase 3α	
tRNA	Transfer RNA	
TWINKLE	Mitochondrial DNA helicase	
ZFN	Zinc-finger nuclease	

Abbreviations for Amino acids

Amino acid	Three letter code	One letter code
Alanine	Ala	A
Arginine	Arg	R
Asparagine	Asn	N
Aspartic acid	Asp	D
Cysteine	Cys	C
Glutamic acid	Glu	E
Glutamine	Gln	Q
Glycine	Gly	G
Histidine	His	H
Isoleucine	Ile	I
Leucine	Leu	L
Lysine	Lys	K
Methionine	Met	M
Phenylalanine	Phe	F
Proline	Pro	P
Serine	Ser	S
Threonine	Thr	T
Tryptophan	Trp	W
Tyrosine	Tyr	Y
Valine	Val	V

ACKNOWLEDGEMENTS

regards to graduate student life. I would also like to express my gratitude to Peter Tessarz for taking me under his wing during the last part of my stay at the institute, as well as to Stephanie Panier and her lab members for accommodating me and allowing me to conduct experiments in their lab.

To my friends – Kris, Tona, Lele, Fred, Gerly, Monique, and Ana – for lifting my spirits during difficult times and emotional lows. Special shoutout to Kris for our Saturday writing updates and life talks.

Finally, I would like to express my heartfelt thanks and appreciation to my family for believing in me throughout this journey. From Day 1 until now, their unconditional love, support, and understanding have played an integral part in my life. And to Robert, for always encouraging me to keep going, thank you very much!

Diese Erklärung muss in der Dissertation enthalten sein.
(*This version must be included in the doctoral thesis*)

„Hiermit versichere ich an Eides statt, dass ich die vorliegende Dissertation selbstständig und ohne die Benutzung anderer als der angegebenen Hilfsmittel und Literatur angefertigt habe. Alle Stellen, die wörtlich oder sinngemäß aus veröffentlichten und nicht veröffentlichten Werken dem Wortlaut oder dem Sinn nach entnommen wurden, sind als solche kenntlich gemacht. Ich versichere an Eides statt, dass diese Dissertation noch keiner anderen Fakultät oder Universität zur Prüfung vorgelegen hat; dass sie - abgesehen von unten angegebenen Teilpublikationen und eingebundenen Artikeln und Manuskripten - noch nicht veröffentlicht worden ist sowie, dass ich eine Veröffentlichung der Dissertation vor Abschluss der Promotion nicht ohne Genehmigung des Promotionsausschusses vornehmen werde. Die Bestimmungen dieser Ordnung sind mir bekannt. Darüber hinaus erkläre ich hiermit, dass ich die Ordnung zur Sicherung guter wissenschaftlicher Praxis und zum Umgang mit wissenschaftlichem Fehlverhalten der Universität zu Köln gelesen und sie bei der Durchführung der Dissertation zugrundeliegenden Arbeiten und der schriftlich verfassten Dissertation beachtet habe und verpflichte mich hiermit, die dort genannten Vorgaben bei allen wissenschaftlichen Tätigkeiten zu beachten und umzusetzen. Ich versichere, dass die eingereichte elektronische Fassung der eingereichten Druckfassung vollständig entspricht."

Teilpublikationen:

Burr, S. P., Klimm, F., Glynos, A., Prater, M., Sendon, P., Nash, P., Powell, C. A., Simard, M.-L., Bonekamp, N. A., Charl, J., Diaz, H., Bozhilova, L. V., Nie, Y., Zhang, H., Frison, M., Falkenberg, M., Jones, N., Minczuk, M., Stewart, J. B., & Chinnery, P. F. (2023). Cell lineage-specific mitochondrial resilience during mammalian organogenesis. *Cell*, *186*, 1–18.

28.02.2024   Pamella Marie Sendon

Datum, Name und Unterschrift

CURRICULUM VITAE

Pamella Marie Sendon

Education

Ph.D. in Genetics
- University of Cologne, Cologne, Germany
- Dissertation: Development and Characterization of a Novel Mouse Model Carrying Specific Mitochondrial DNA Mutations

Masters, Major in Agronomy
- Kyungpook National University, Daegu, South Korea
- Dissertation: Activation of C2H2-type Zinc Finger Genes Induces Dwarfism in Arabidopsis thaliana

Bachelor of Science in Biology
- University of the Philippines-Los Baños, Laguna, Philippines
- Internship: Asian Vegetable Research and Development Center, Taiwan
- Dissertation: Tissue culture and genetic transformation of hot pepper (Capsicum annum L. var Nok-gouang) mediated by Agrobacterium tumefaciens

Employment History

Guest researcher
Doctoral researcher
- Max Planck Institute for Biology of Ageing (MPI-AGE), Cologne, Germany
- Responsible for developing and characterizing a novel mouse model carrying specific mitochondrial DNA mutations

Researcher
- Institute of Plant Breeding, Laguna, Philippines
- In charge of the development of molecular markers for smut (fungal disease)-resistance in sugarcane

Research associate
- International Rice Research Institute (IRRI), Laguna, Philippines
- Performed phenotypic and genotypic screening using molecular markers for submergence/flooding tolerance in rice

Awards and Scholarships

Marie Skłodowska Curie Fellowship Initial Training Network
National Research Foundation Korea and Kyungpook National University
        Honours Scholarship
International Rice Research Institute Internship
Asian Vegetable Research and Development Center Undergraduate Internship

Publications

Burr, S.P., Klimm, F., Glynos, A., Prater, M., **Sendon, P.**, Nash, P., Powell, C.A., Simard, M.-L., Bonekamp, N.A., Charl, J., Diaz, H., Bozhilova, L.V., Nie, Y., Zhang, H., Frison, M., Falkenberg, M., Jones, N., Minczuk, M., Stewart, J.B., and Chinnery, P.F. 2023. Cell lineage-specific mitochondrial resilience during mammalian organogenesis. Cell 186:1-18.

Bello, E.B., Rasco, J.L.S., **Sendon, P.M.D.**, Dela Cueva, F.M., Lalusin, A.G., and Laurena, A.C. 2019. Genetic Diversity Analysis of Selected Sugarcane (Saccharum spp. Hybrids) Varieties Using DArT-Seq Technology. Philippine Journal of Science 148(S1): 103-114.

Sendon, P.M., Oo, M.M., Park, J.B., Lee, B.H., Kim, J.H., Seo, H.K., Park, S.K., and Song, J.T. 2014. Activation of C2H2-type Zinc Finger Genes Induces Dwarfism in Arabidopsis thaliana. Journal of the Korean Society for Applied Biological Chemistry 57:35-41.

Sendon, P.M., Park, J.-B., Park, S.-K., and Song, J.T. 2013. GUS Expression Driven by Promoter of AtSAGT1 Gene Encoding a Salicylic Acid Glucosyltransferase 1 in Arabidopsis Plants. Current Research on Agriculture and Life Sciences 31(2):83-87.

Septiningsih, E.M., Ignacio, J.C.I., **Sendon, P.M.D.**, Sanchez, D.L. Ismail, A.M., and Mackill, D.J. 2013. QTL mapping and confirmation for tolerance of anaerobic conditions during germination derived from the rice landrace Ma-Zhan Red. Theoretical and Applied Genetics DOI 10.1007/S00122-013-2057-1.

Sendon, P.M., Park, J.-B., Seo, H.S., Park, S.-K., and Song, J.T. 2012. Temporal and Spatial Expression Patterns of the Gene AtBSMT1 Encoding a Salicylic Acid Methyltransferase in Arabidopsis Transgenic Plants. Journal of the Korean Society for Applied Biological Chemistry 55:823-826.

Septiningsih, E.M., Sanchez, D.L., Sing, N., **Sendon, P.M.D.**, Pamplona, A.M., Heuer, S., and Mackill, D.J. 2012. Identifying novel QTLs for submergence tolerance in rice cultivars IR72 and Madabaru. Theoretical and Applied Genetics 124:867-874.

Park, J.-B., **Sendon, P.M.**, Kwon, S.H., Seo, H.S., Park, S.-K., Kim, J.H., and Song, J.T. 2012. Overexpression of Stress-Related Genes, BrERF4 and AtMYB44, in Arabidopsis thaliana Alters Cell Expansion but Not Cell Proliferation During Leaf Growth. Journal of Plant Biology 55:406-412.

Sendon, P.M., Seo, H.S., and Song, J.T. 2011. Salicylic Acid Signaling: Biosynthesis, Metabolism, and Crosstalk with Jasmonic Acid. Journal of the Korean Society for Applied Biological Chemistry 54:501-506.